OSU

The Ohio State University

A CASSEGRAIN REFLECTOR SYSTEM FOR COMPACT RANGE APPLICATIONS

Mark D. Rader
W.D. Burnside

The Ohio State University

ElectroScience Laboratory

Department of Electrical Engineering
Columbus, Ohio 43212

Technical Report 716148-14
Contract NSG 1613
July 1986

National Aeronautics and Space Administration
Langley Research Center
Hampton, VA 23665

NOTICES

When Government drawings, specifications, or other data are used for any purpose other than in connection with a definitely related Government procurement operation, the United States Government thereby incurs no responsibility nor any obligation whatsoever, and the fact that the Government may have formulated, furnished, or in any way supplied the said drawings, specifications, or other data, is not to be regarded by implication or otherwise as in any manner licensing the holder or any other person or corporation, or conveying any rights or permission to manufacture, use, or sell any patented invention that may in any way be related thereto.

50272-101

REPORT DOCUMENTATION PAGE	1. REPORT NO.	2.	3. Recipient's Accession No.

4. Title and Subtitle
A Cassegrain Reflector System for Compact Range Applications

5. Report Date
July 1986

6.

7. Author(s)
Mark D. Rader, W.D. Burnside

8. Performing Organization Rept. No.
716148-14

9. Performing Organization Name and Address
The Ohio State University ElectroScience Laboratory
1320 Kinnear Road
Columbus, Ohio 43212

10. Project/Task/Work Unit No.

11. Contract(C) or Grant(G) No.
(C) NSG 1613
(G)

12. Sponsoring Organization Name and Address
National Aeronautics and Space Administration
Langley Research Center
Hampton, VA 23665

13. Type of Report & Period Covered
Technical

14.

15. Supplementary Notes

16. Abstract (Limit: 200 words)

An integral part of a compact range is the means of providing a uniform plane wave. A Cassegrain reflector system is one alternative for achieving this goal. Theoretically, this system offers better performance than a simple reflector system. The longer path-lengths in the Cassegrain system lead to a more uniform field in the plane of interest.

The addition of the subreflector creates several problems, though. System complexity is increased both in terms of construction and performance analysis. The subreflector also leads to aperture blockage and the orientation of the feed now results in spillover illuminating the target area as well as the rest of the range. Finally, the addition of the subreflector leads to interactions between the two reflectors resulting in undesired field variations in the plane of interest.

These difficulties are addressed and through the concept of blending the surfaces, a Cassegrain reflector system is developed that will provide a uniform plane wave that offers superior performance over large target areas for a given size reflector system. Design and analysis is implemented by considering the main reflector and subreflector separately. Then the system may be put together and the final design and system analysis completed.

17. Document Analysis a. Descriptors

b. Identifiers/Open-Ended Terms

c. COSATI Field/Group

18. Availability Statement
A. Approved for public release; distribution is unlimited.

19. Security Class (This Report)
Unclassified

21. No. of Pages
180

20. Security Class (This Page)
Unclassified

22. Price

(See ANSI-Z39.18)

See Instructions on Reverse

OPTIONAL FORM 272 (4-77)
(Formerly NTIS-35)
Department of Commerce

TABLE OF CONTENTS

LIST OF FIGURES

CHAPTER I

INTRODUCTION

Recently, the indoor compact range has received much attention and is increasng in popularity as it rivals the outdoor range for antenna and scattering measurements. As the compact range performance improves, its use will continue to grow. An integral part of this system is the means of providing a uniform plane wave. This study presents a Cassegrain antenna feed system as a means to achieve a more uniform plane wave.

Normally, a single parabolic reflector is used to generate this plane wave. Edge diffractions are the major drawback to this reflector system because they generate ripple on the desired uniform plane wave. One method used to reduce this ripple is through the use of serrated edges. The edges may also be rolled to reduce the ripple and provide structural strength as well. Large circular rolled edges provide greater ripple reduction but require additional structural support and are more costly. Elliptic edges are also used to control ripple and these are more effective than simple circular edges since there is more control over the shape such that a smaller ellipse can work as well as a larger circular edge. At the bottom of a parabolic dish section, serrated absorber patterns are often used to break up the field. Proper

tapering of the feed horn field pattern will also minimize the diffracted fields.

Another possible alternative to the reflector system is the use of a lens antenna. But lens antennas are not being widely used due to several disadvantages. Although lens antennas are frequency dependent, the major disadvantage is in the construction of the antenna itself. Reflector antennas are much easier to design since only one surface needs to be considered. If made of natural dielectrics, lens antennas can be heavy and bulky, especially at lower frequencies. The homogeneity of the dielectric is also often in question. Besides the structural problems, lenses are also inherently lossy and reflections occur at both interfaces [1]. Therefore, reflector type antennas are usually favored over lens antennas.

The alternative considered in this study is the Cassegrain reflector system. Theoretically, the Cassegrain system offers better performance than a simple reflector system. The longer pathlengths in the Cassegrain system lead to a more uniform field in the plane of interest. The convenient location of the feed and supporting hardware is another advantage of this system.

Initially, several disadvantages to the Cassegrain system are apparent. The addition of the subreflector increases system complexity both in terms of construction and performance analysis. The subreflector also gives rise to aperture blockage. The orientation of the feed now leads to spillover illuminating the target area as well as the rest of the room. Finally, the addition of the subreflector leads

to interactions between the two reflectors resulting in undesired field variations in the target area. These problems are considered as the Cassegrain system is designed and analyzed.

The major design consideration in implementing the Cassegrain system is through the blending of the edges to improve performance as opposed to simply attaching circular or elliptical edges. The blending technique is a better method of providing the transition from one curve to another. Blending also reduces the junction diffracted field and therefore enhances performance. The tapering of the field is also controlled through the blending process. In fact, the blending concept is what allows the Cassegrain system to work as an effective source of a uniform plane wave.

CHAPTER II

THEORY

A. CASSEGRAIN REFLECTOR SYSTEM GEOMETRY

The Cassegrain antenna system consists of a main reflector, subreflector, and feed. The main reflector is a parabolic curve while the subreflector has a hyperbolic contour. Two foci are present in this system: the real focal point located at the feed and the virtual focal point located at the focus of the parabola. To generate this system, two variables for each reflector must be specified. Seven variables are used to describe this system and three equations used to solve for the three remaining unknowns (Figure 2.1) are as follows:

$$\tan \frac{1}{2}\phi v = \pm \frac{1}{4} \frac{Dm}{Fm} \tag{2.1}$$

$$\frac{1}{\tan \phi v} + \frac{1}{\tan \phi r} = 2 \frac{Fc}{Ds} \quad , \quad \text{and} \tag{2.2}$$

$$1 - \frac{\sin(\phi v - \phi r)/2}{\sin(\phi v + \phi r)/2} = 2 \frac{Lv}{Fc} \quad . \tag{2.3}$$

Equation (2.1) applies to the main reflector while Equations (2.2) and (2.3) apply to the subreflector. The negative sign applies to the

Gregorian forms of the system.

The parabolic main reflector is generated by

$$Xm = \frac{Ym^2}{4Fm} \quad . \tag{2.4}$$

The hyperbolic subreflector is generated by

$$Xs = a\left[\sqrt{1+\left(\frac{Ys}{b}\right)^2} - 1\right] \tag{2.5}$$

where

$$e = \frac{\sin(\phi v+\phi r)/2}{\sin(\phi v-\phi r)/2} \tag{2.6}$$

$$a = \frac{Fc}{2e} \quad , \text{ and} \tag{2.7}$$

$$b = a\sqrt{e^2-1} \quad . \tag{2.8}$$

These equations govern the classical Cassegrain system. Using these equations, many variations of the basic system may be formed. For this study, the basic system of Figure 2.1 is sufficient, though one variation is considered. The Gregorian form occurs when the focus of the main reflector moves between the two reflectors (see Figure 2.2). In this case the contour of the subreflector is elliptical. The negative sign must be used in equation (2.1) since ϕv is now negative. Otherwise, the equations remain the same.

In later analysis, the use of the virtual feed is made. In this concept, the real feed and subreflector are replaced by a virtual feed

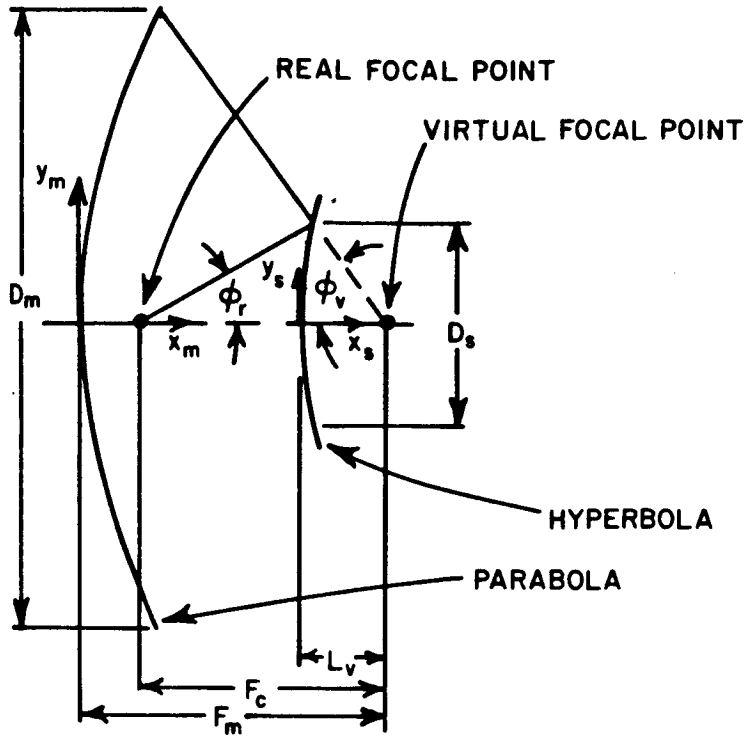

Figure 2.1 Geometry of Cassegrain system.

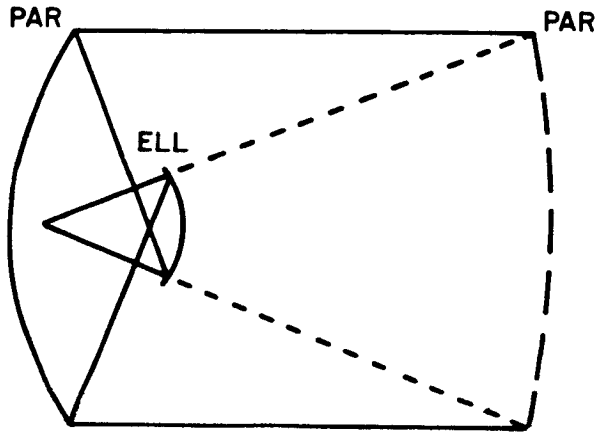

Figure 2.2 Gregorian form.

at the focal point of the main reflector. The system is now a single reflector design, and this concept is useful when designing and analyzing the main reflector.

Another useful concept is that of the equivalent parabola. As is seen in Figure 2.3, the Cassegrain system is replaced by an equivalent surface which has a parabolic contour as demonstrated by Hannan [2]. Using this concept, the feed remains unchanged, and ray optics are used to determine the surface as the locus of incoming rays intersecting the rays converging to the real feed. Then the Cassegrain system has been replaced by an equivalent single reflector system. The following equations show the relationship between the two systems:

$$\frac{1}{4}\frac{Dm}{Fe} = \tan\frac{1}{2}\phi r \qquad (2.9)$$

$$Xe = \frac{Ye^2}{4Fe} \quad , \quad \text{and} \qquad (2.10)$$

$$\pm\frac{Fe}{Fm} = \frac{\tan\phi v/2}{\tan\phi r/2} = \frac{L_r}{L_v} = \frac{e+1}{e-1} \quad . \qquad (2.11)$$

Again, the negative sign applies to the Gregorian forms. Equation (2.9) generates the equivalent focal length. Equation (2.10) generates the equivalent parabolic surface, and Equation (2.11) provides several expressions for comparing the focal lengths. For the classical Cassegrain system, Fe/Fm is greater than one. It is apparent that a Cassegrain system has a much smaller focal length but can be equivalent to a single reflector system of much larger focal length. It is this

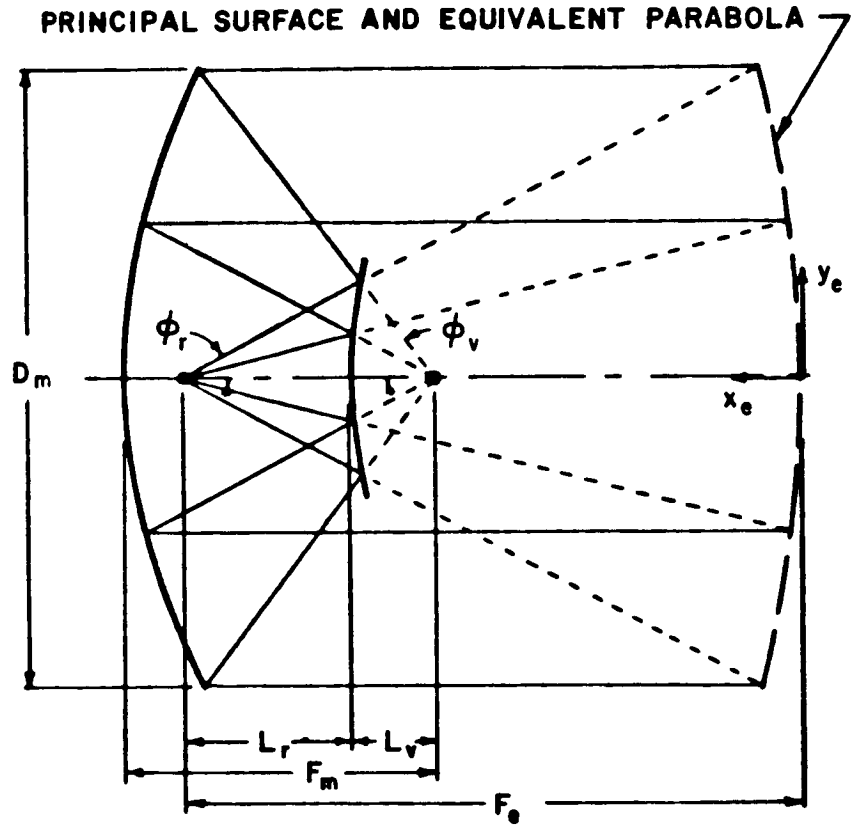

Figure 2.3 Equivalent-parabola concept.

idea that favors the Cassegrain system over the single reflector system. When working in a restricted area, such as a compact range, the shorter Cassegrain system is favored over the longer equivalent single reflector system [2].

B. MOMENT METHOD ANALYSIS

Several analysis techniques are used when studying the Cassegrain system. The first that will be described is the moment method theory. Only the two-dimensional part of this theory is outlined [3]. By using the reaction concept of Rumsey [4], a moment method solution may be obtained. In Figure (2.4) a scattering problem is presented. The source electrical and magnetic currents $(\vec{J}_i, \vec{M}_i)$ generate electric and magnetic fields $(\vec{E}, \vec{H})$ in the presence of the scatterer which is a conducting body in free space.

The surface-equivalence theorem of Schellkunoff [5] gives an equivalent problem by replacing the scatterer by the following surface current densities:

$$\bar{J}_S = \hat{n} \times \bar{H} \quad , \quad \text{and} \tag{2.12}$$

$$\bar{M}_S = \bar{E} \times \hat{n} \tag{2.13}$$

with $\hat{n}$ being the outward normal to the surface. It is self-evident that the source currents $(\bar{J}_i, \bar{M}_i)$ generate the incident fields $(\bar{E}_i, \bar{H}_i)$ in the free space. The scattered fields are given by

$$\bar{E}_S = \bar{E} - \bar{E}_i, \quad \text{and} \tag{2.14}$$

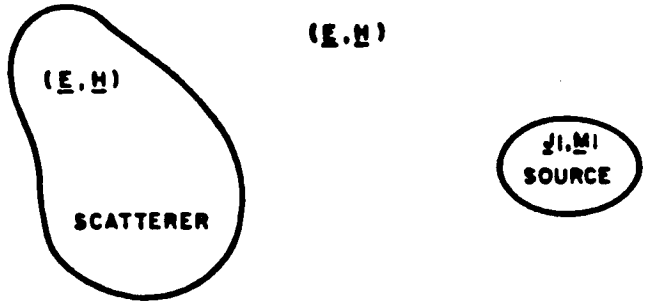

(a) The source $(\vec{J}_i, \vec{M}_i)$ generates the field $(\vec{E}, \vec{H})$ with the scatterer present.

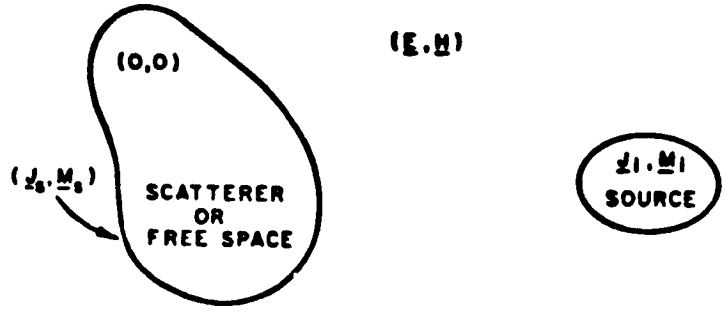

(b) The interior field vanishes when the currents $(\vec{J}_S, \vec{M}_S)$ are introduced on the surface of the scatterer.

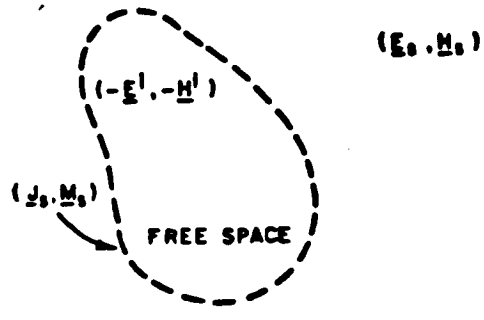

(c) The exterior scattered field may be generated by $(\vec{J}_S, \vec{M}_S)$ in free space.

Figure 2.4 Scattering problems.

$$\bar{H}_s = \bar{H} - \bar{H}_i \quad . \tag{2.15}$$

The surface currents generate the scattered fields $(\bar{E}_s, \bar{H}_s)$ outside the body and $(-\bar{E}_i, -\bar{H}_i)$ inside the body.

An electric test source $\bar{J}_m$ is now placed within the region of the scatterer (see Figure 2.5). Because there is no field in this region, the reaction of this test source with the field produced by the other sources is zero. By reciprocity, this reaction must be equivalent to the reaction of the other sources with the field produced by the test source. Then, one finds that

$$\iint(\bar{J}_s \cdot \bar{E}_m - \bar{M}_s \cdot \bar{H}_m)ds + \iiint(\bar{J}_i \cdot \bar{E}_m - \bar{M}_i \cdot \bar{H}_m)dv = 0 \quad . \tag{2.16}$$

This equation is the basis of this solution and approach is the "zero-reaction theorem" of Rumsey [4].

Next, the surface current distributions $(\bar{J}_s, \bar{M}_s)$ need to be determined. These currents are constructed of finite series with N unknown coefficients. For this problem, the scattering body is a perfect electrical conductor so $\bar{M}_s$ vanishes. Since only the two-dimensional case is being considered, $\bar{J}_s$ is a function of the position ℓ around the contour of the body. Also consider a magnetic line source and TE_z polarization so that $\bar{J}_i$ is zero. Then the integral equation reduces such that

$$\int_c \bar{J}_s \cdot \bar{E}_m \, d\ell = \iint \bar{M}_i \cdot \bar{H}_m \, ds \quad . \tag{2.17}$$

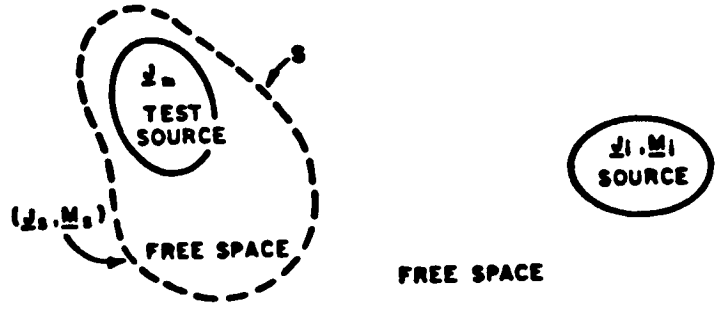

Figure 2.5 Placement of test source.

The electric currents may now be represented by

$$\bar{J}_S(\ell) = \sum_{n=1}^{N} I_n \bar{J}_n(\ell) \tag{2.18}$$

where I_n are complex constants, and samples of $\bar{J}_S(\ell)$ and $\bar{J}_n(\ell)$ are the basis functions. The basis functions as well as the test source have unit current density at their terminals. Substituting this series into the integral equation yields

$$\sum_{n=1}^{N} I_n Z_{mn} = V_m \quad \text{with } m = 1,2,3,\ldots N \tag{2.19}$$

where

$$Z_{mn} = -\int_n \bar{J}_n(\ell)\cdot\bar{E}_m d\ell = -\int_m \bar{J}_m(\ell)\cdot\bar{E}_n d\ell, \text{ and} \tag{2.20}$$

$$V_m = -\iint_i \bar{M}_i \cdot \bar{H}_m ds = \int_m \bar{J}_m(\ell)\cdot\bar{E}_i d\ell \tag{2.21}$$

with the integrations are done over the non-zero range of the integrands.

When solving these expressions on a computer, it is advantageous for the impedance matrix, Z_{mn}, to be symmetrical. Also, the test sources, $\bar{J}_m$, should be the same size, shape, and functional form as the basis functions $\bar{J}_n$. This will allow some of the integrals to be solved in closed form and yield readily solvable simultaneous linear equations. In addition, the test sources are placed a distance δ from the surface where δ tends toward zero in the limiting case of the integrals. In this case, sinusoidal strip dipoles are chosen as the basis functions (see Figure 2.6). This planar strip dipole extends infinitely in the z-direction and has a surface current density given by [9]

$$\bar{J} = \hat{x}\,\frac{\sin[k(x-x_1)]}{\sin[k(x_2-x_1)]} \tag{2.22}$$

for $x_1 < x < x_2$, and

$$\bar{J} = \hat{x}\,\frac{\sin[k(x_3-x)]}{\sin[k(x_3-x_2)]} \tag{2.23}$$

for $x_2 < x < x_3$. Similarly, for the strip v-dipole in Figure 2.7 the surface current density is given by

$$\bar{J} = -\hat{s}\,\frac{\sin[k(t_1-t)]}{\sin(ks_1)} \tag{2.24}$$

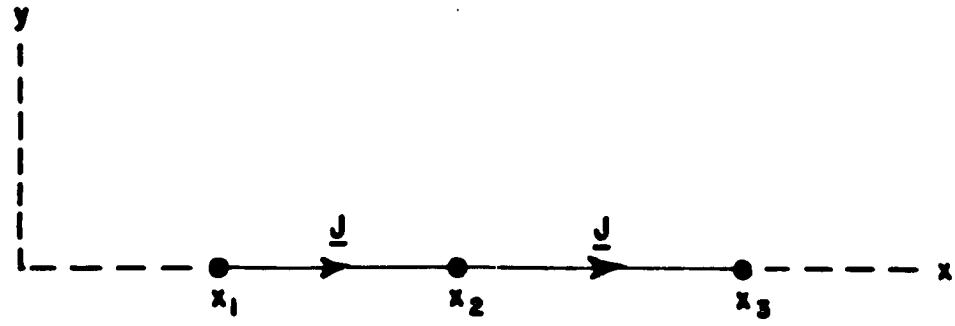

(a) A planar strip dipole with edges at x_1 and x_3 and terminals at x_2.

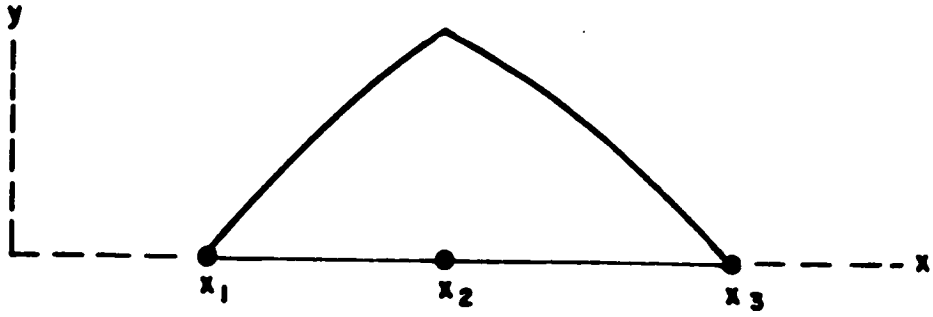

(b) The current-density distribution $\vec{J}$ on the sinusoidal strip dipole.

Figure 2.6 Sinusoidal strip dipoles for basis functions.

on arm s, and

$$\bar{J} = \hat{t}\,\frac{\sin[k(t_1-t)]}{\sin(kt_1)} \tag{2.25}$$

on arm t. It is evident that $\hat{s}$ and $\hat{t}$ are perpendicular to the z-axis. In both cases, the current density goes to zero at the endpoints and is unity at the center terminals. Also, a slope discontinuity is present at the center terminals. Of course the v-dipole reduces to the planar case when ψ is equal to 180°.

The field of the strip dipole may be obtained from the superposition of two strip monopoles considered to have a common endpoint (see Figure 2.8). The field for the strip monopole is known from reference [6]. Now the calculation may begin for elements of the impedance matrix as well as the V_m elements of the excitation column.

First consider an open or closed perfectly conducting polygon cylinder (see Figure 2.9). For this open cylinder, surface currents flow on both sides of the conductor, and the surface current density is given by $\bar{J}_s$. A magnetic line source $\bar{M}_i$ is present and I_1 and I_2 are the current densities at the corners of the polygon. Two strip dipole mode currents may now be defined on the conductor. The first extends from point 0 to point 2 with terminals at point 1. The second extends from point 1 to point 3 with terminals at point 2. Each mode has a sinusoidal current distribution as described earlier. Now the current density $\bar{J}_s$ is the superposition of these two modes with weightings of I_1 and I_2. Then $\bar{J}_s$ is a piecewise sinusoidal expansion with unknown constants, I_1 and I_2. Since the polygon is a perfect conductor, the

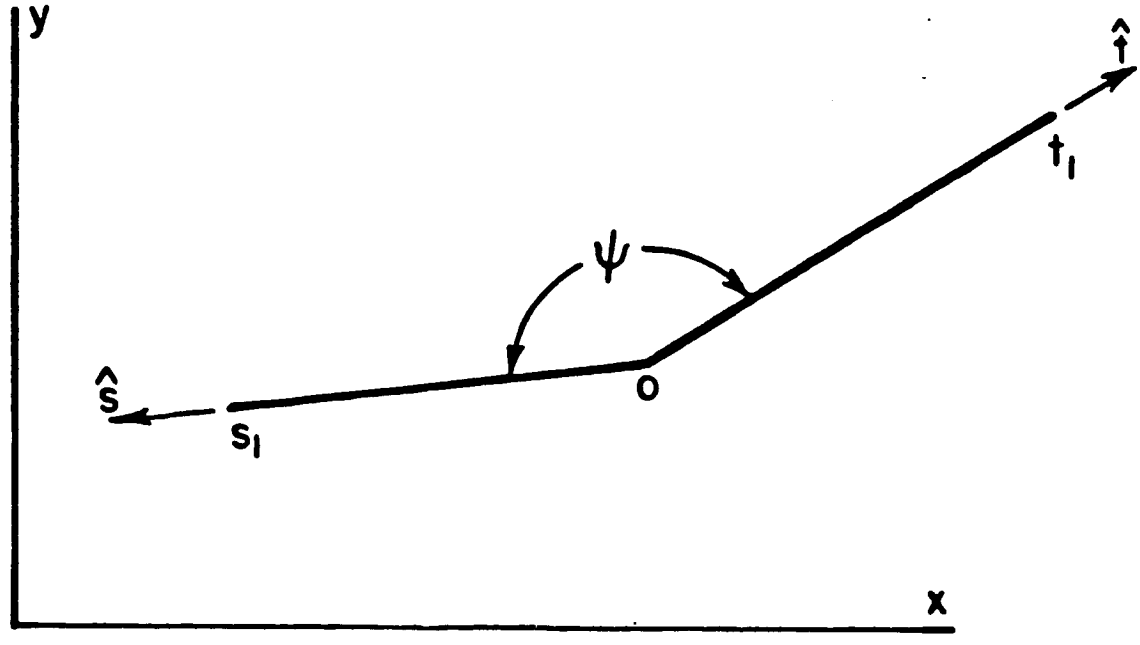

Figure 2.7 Nonplanar strip dipole with edges at s_1 and t_1 and terminals at 0.

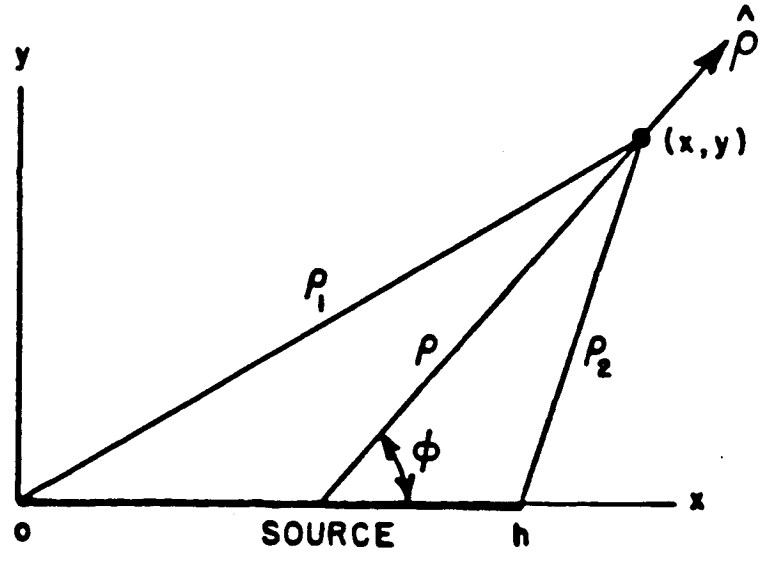

Figure 2.8 An electric strip monopole and the coordinate system.

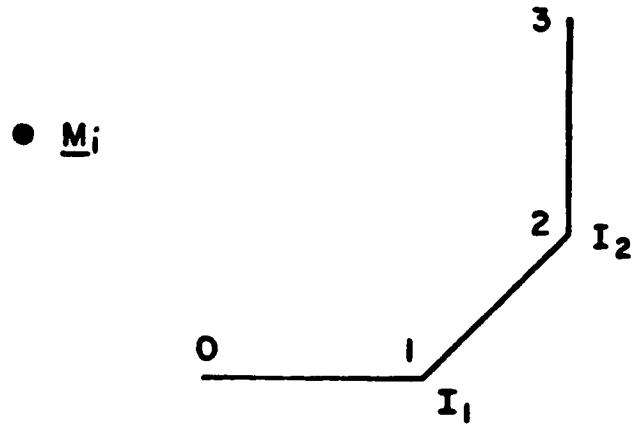

(a) Perfectly conducting polygon cylinder with parallel magnetic line source $\vec{M}_i$.

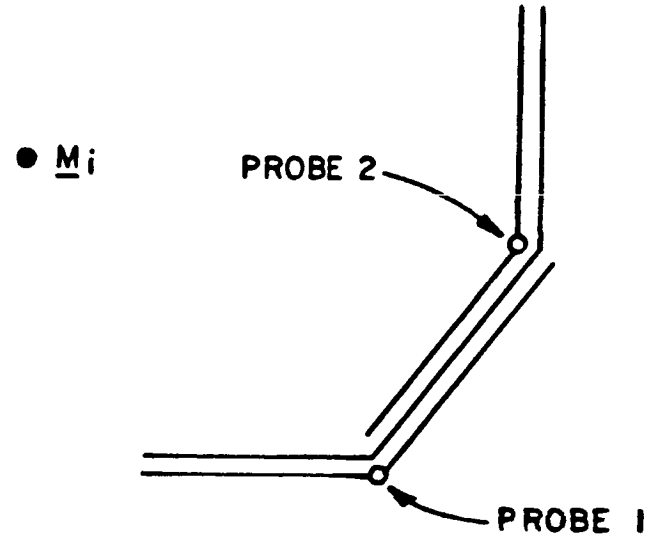

(b) Electric test probes 1 and 2 are moved to the conducting surface.

Figure 2.9 Probing of a perfectly conducting polygon cylinder.

tangential electric field is zero on the surface. So, if an electric test probe is moved along the conducting surface, the open circuit voltage at its terminals can be examined. For N different current samples, N probing tests are done. The probes may be real (thin wire v-dipoles) or hypothetical (electric line sources or strip dipoles). Then the currents I_n are adjusted until all the probes read zero. Finally, as N increases this stationary solution for the currents approaches the rigorous solution. The mutual impedance between the m^{th} test probe and the n^{th} current mode is Z_{mn}. The probe sums all the voltage contributions from $\bar{J}_s$ and $\bar{M}_i$ and this result must be zero, resulting once again in Equations (2.19) to (2.21).

Finally, the simultaneous linear equations are solved using linear algebra techniques, and the current distribution $\bar{J}_s$ is known. The scattered fields ($\bar{E}_s$,$\bar{H}_s$) may then be found. J.H. Richmond [6] provided this theory, method, and appropriate computer programs. Using duality, the TM polarization case could also be solved.

C. UNIFORM GEOMETRICAL THEORY OF DIFFRACTION ANALYSIS

Another analysis technique used is that of the Uniform Geometrical Theory of Diffraction. Again, only the two-dimensional part of this theory is outlined.

For the Cassegrain system three basic field components are examined (see Figure 2.10). These are the incident, reflected and diffracted fields. The total field is then given by

$$U^{TOTAL} = U^{INC} + U^{REF} + U^{DIF} \qquad (2.26)$$

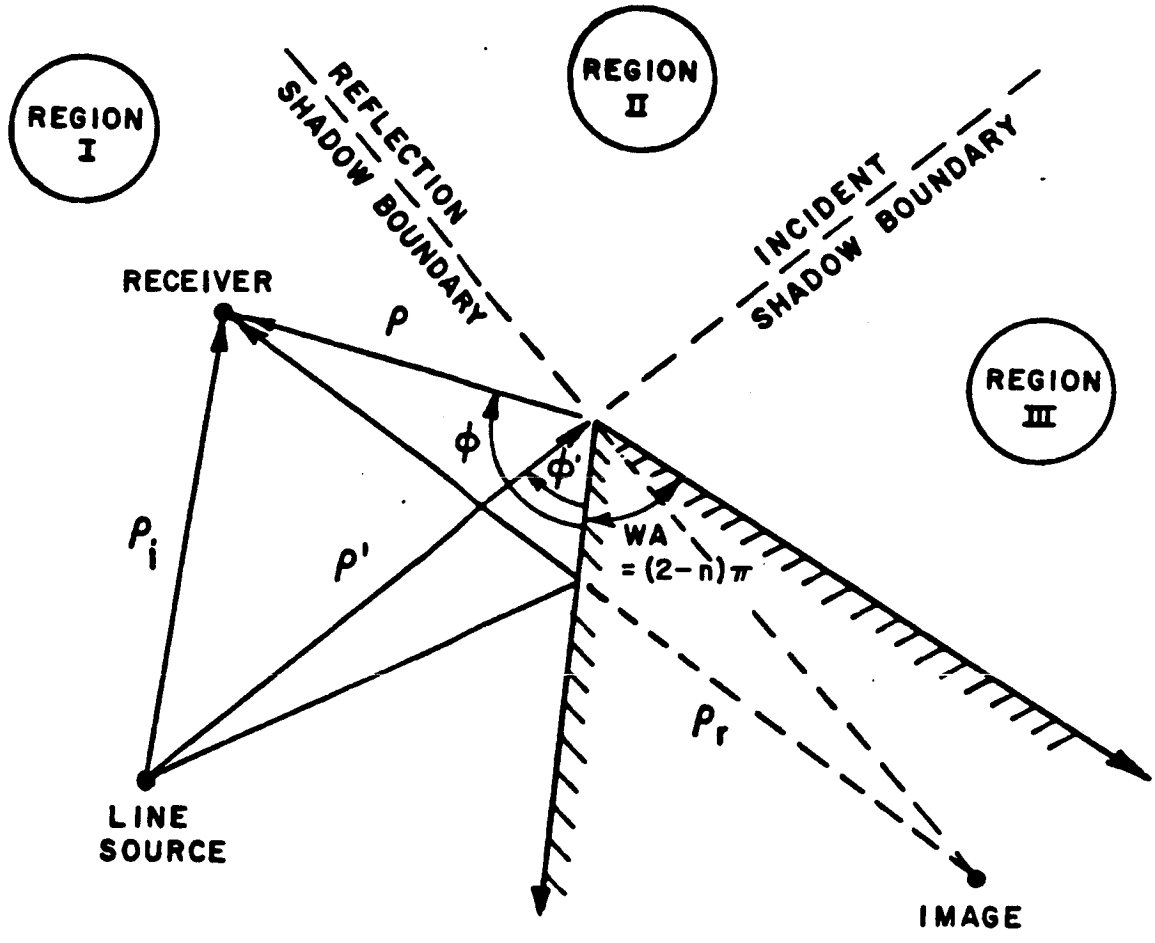

Figure 2.10 Basic UTD field components.

where U represents an electric scalar field for the electric line source case and a magnetic scalar field for the magnetic line source case. The incident field is given by

$$U^{INC} = \begin{cases} C \dfrac{e^{-jk\rho_i}}{\sqrt{\rho_i}} & \text{Regions I and II, and} \\ 0 & \text{Region III} \end{cases} \tag{2.27}$$

whereas ρ_i is the distance between the source and receiver. Note that C is a complex constant. The reflected field is given by

$$U^{REF} = \begin{cases} \pm C \dfrac{e^{-jk\rho_r}}{\sqrt{\rho_r}} & \text{Region I, and} \\ 0 & \text{Regions II and III} \end{cases} \tag{2.28}$$

where ρ_r is the distance from the image of the source to the receiver and the positive sign is used for the magnetic line source case and the minus sign for the electric line source case. To simplify calculations the magnetic line source is used when analyzing the Cassegrain system. The diffracted field is given by

$$U^{DIFF} = \left[D\left[\frac{\rho'\rho}{\rho'+\rho}, \phi-\phi', n\right] \pm D\left[\frac{\rho'\rho}{\rho'+\rho}, \phi+\phi', n\right] \right] C \frac{e^{-jk\rho'}}{\sqrt{\rho'}} \frac{e^{-jk\rho}}{\sqrt{\rho}} \tag{2.29}$$

with the plus and minus signs for the magnetic and electric line source cases, respectively. The term with $\phi-\phi'$ is associated with the incident shadow boundary while the term with $\phi+\phi'$ is associated with the reflected shadow boundary.

Now consider a curved conducting strip as will be found in the Cassegrain system (see Figure 2.11). The incident field does not change but the reflected field is now given by

$$U^{REF} = \begin{cases} \pm \sqrt{\dfrac{\rho_c(Q_R)}{\rho_c(Q_R)+\rho_r}}\; C\, \dfrac{e^{-jk\rho_i}}{\sqrt{\rho_i}}\, e^{-jk\rho_r} & \text{Region I, and} \\ 0 & \text{Regions II and III} \end{cases} \tag{2.30}$$

with the calculation of $\rho_c(Q_R)$ needed. This caustic distance varies with the reflection point Q_R and is given by

$$\frac{1}{\rho_c(Q_R)} = \frac{1}{\rho_i} + \frac{2}{R_c \cos\theta_i} \tag{2.31}$$

where R_c is the radius of curvature of the surface at the reflection point, Q_R. The diffracted field is given by

$$U^{DIFF} = \left[D\left[\frac{\rho'\rho}{\rho'+\rho}, \phi-\phi', n\right] \pm D\left[\frac{\rho_c'\rho}{\rho c'+\rho}, \phi+\phi', n\right] \right] C\, \frac{e^{-jk\rho'}}{\sqrt{\rho'}}\, \frac{e^{-jk\rho}}{\sqrt{\rho}} \tag{2.32}$$

where ρ_c' is the caustic distance $\rho_c(Q_E)$ associated with the reflected ray from the edge and n=2 such that

$$D(L,B,n=2) = -\frac{-e^{-j\pi/4}}{2\sqrt{2\pi k}}\, \frac{F(KLa(\beta))}{\cos(\beta/2)} \tag{2.33}$$

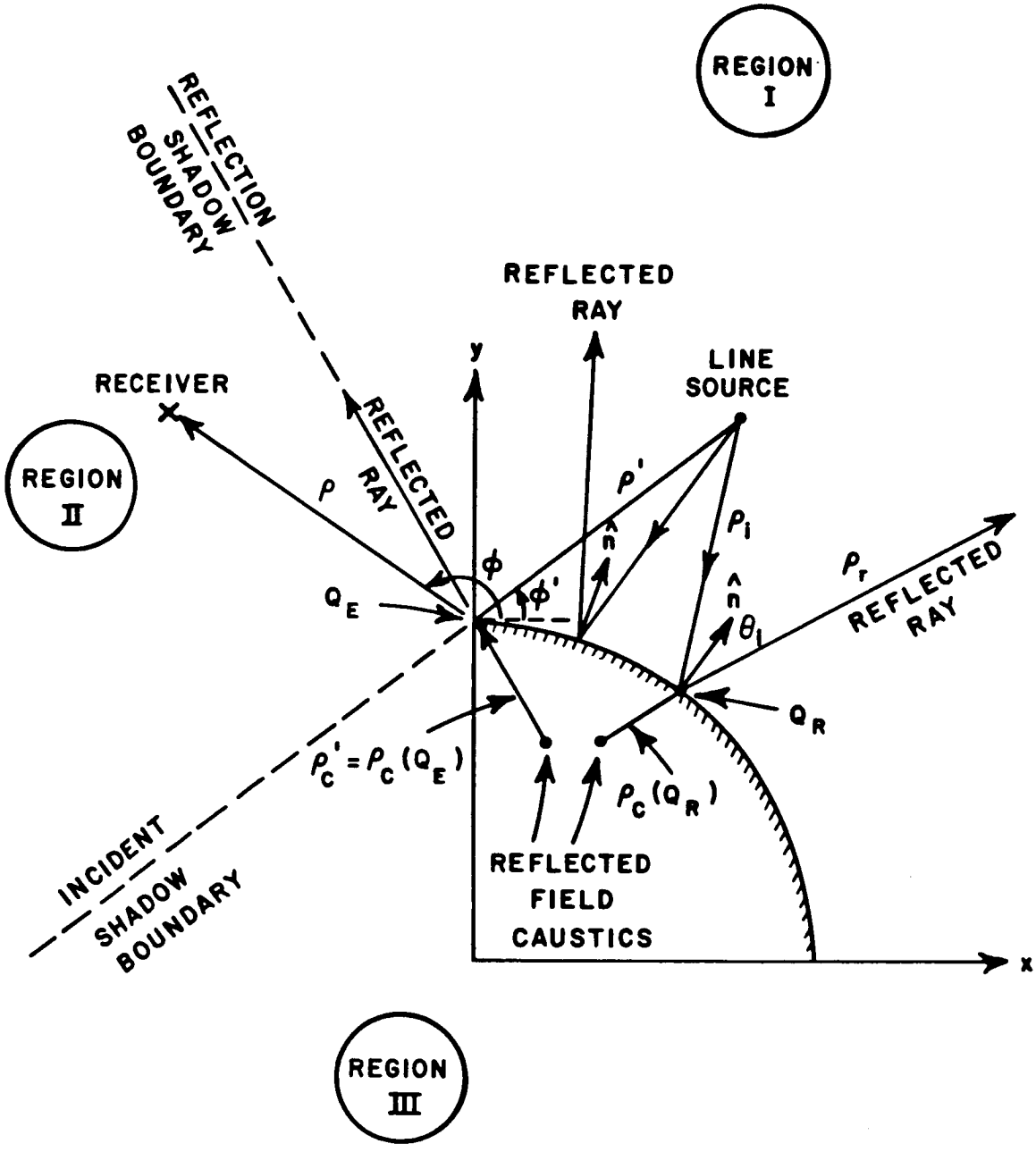

Figure 2.11 Curved conducting strip.

$$F(KLa(\beta)) = 2j\sqrt{KLa(\beta)}\, e^{jkLa(\beta)} \int_{\sqrt{KLa(\beta)}}^{\infty} e^{-j\tau^2} d\tau, \text{ and} \qquad (2.34)$$

$$a(\beta) = 2\cos^2(\beta/2) \quad . \qquad (2.35)$$

The diffracted field given is sufficient for the knife edge case but the general form of the diffraction coefficient is also needed. So more generally, the diffracted field is expressed by

$$U^{DIFF} = D_{\substack{S \\ H}} U^i(Q_E) \frac{e^{-jk\rho}}{\sqrt{\rho}} \qquad (2.36)$$

where $U^i(Q_E)$ is the incident field on the edge, and

$$D_{\substack{S \\ H}}(\phi, \phi', n) = \frac{-e^{-j\pi/4}}{2n\sqrt{2\pi k}} \; x$$

$$\left[\cot\left(\frac{\pi+(\phi-\phi')}{2n}\right) F\left[KL^i a^+(\phi-\phi')\right] + \cot\left(\frac{\pi-(\phi-\phi')}{2n}\right) F\left[KL^i a^-(\phi-\phi')\right] \mp \right.$$

$$\left.\left\{\cot\left(\frac{\pi+(\phi+\phi')}{2n}\right) F\left[KL^{rn} a^+(\phi+\phi')\right] + \cot\left(\frac{\pi-(\phi+\phi')}{2n}\right) F\left[KL^{ro} a^-(\phi+\phi')\right]\right\}\right] \qquad (2.37)$$

where

$$F(x) = 2j\sqrt{x}\, e^{jx} \int_{\sqrt{x}}^{\infty} e^{-j\tau^2} d\tau, \text{ and} \qquad (2.38)$$

$$a^{\pm}(\beta) = 2\cos^2\frac{(2n\pi N^{\pm}-\beta)}{2} \quad . \tag{2.39}$$

Note that $N^{\pm}$ are integers most nearly satisfying the following expressions:

$$2\pi nN^{+}-(\beta) = \pi, \text{ and} \tag{2.40}$$

$$2\pi nN^{-}-(\beta) = -\pi. \tag{2.41}$$

These expressions are valid for both the soft and hard diffraction coefficients but only the hard case is used here with a magnetic line source. The transition function F(x) involves a Fresnel integral, and a plot of F(x) is shown in Figure 2.12.

The diffraction coefficient may also be written as

$$D_{\substack{S\\H}} = D(L^i,L^i,\phi-\phi',n) \mp D(L^{rn},L^{ro},\phi+\phi',n) \tag{2.42}$$

where

$$D(L_1,L_2,\phi\pm\phi',n) = \left[\cot\left(\frac{\pi+(\phi\pm\phi')}{2n}\right) F(KL_1a^{+}(\phi\pm\phi')) + \right.$$

$$\left. \cot\left(\frac{\pi-(\phi\pm\phi')}{2n}\right) F(KL_2a^{-}(\phi\pm\phi'))\right] \frac{-e^{-j\pi/4}}{2n\sqrt{2\pi k}} \quad . \tag{2.43}$$

Figure 2.13 shows a more generalized structure. Depending on the positioning of the line source, reflected fields may emanate from both surfaces. So two reflection shadow boundaries may exist, and hence the reason $D(L^{rn},L^{ro},\phi+\phi',n)$ is composed of two terms. The first term is associated with the n face boundary and the second with the o face

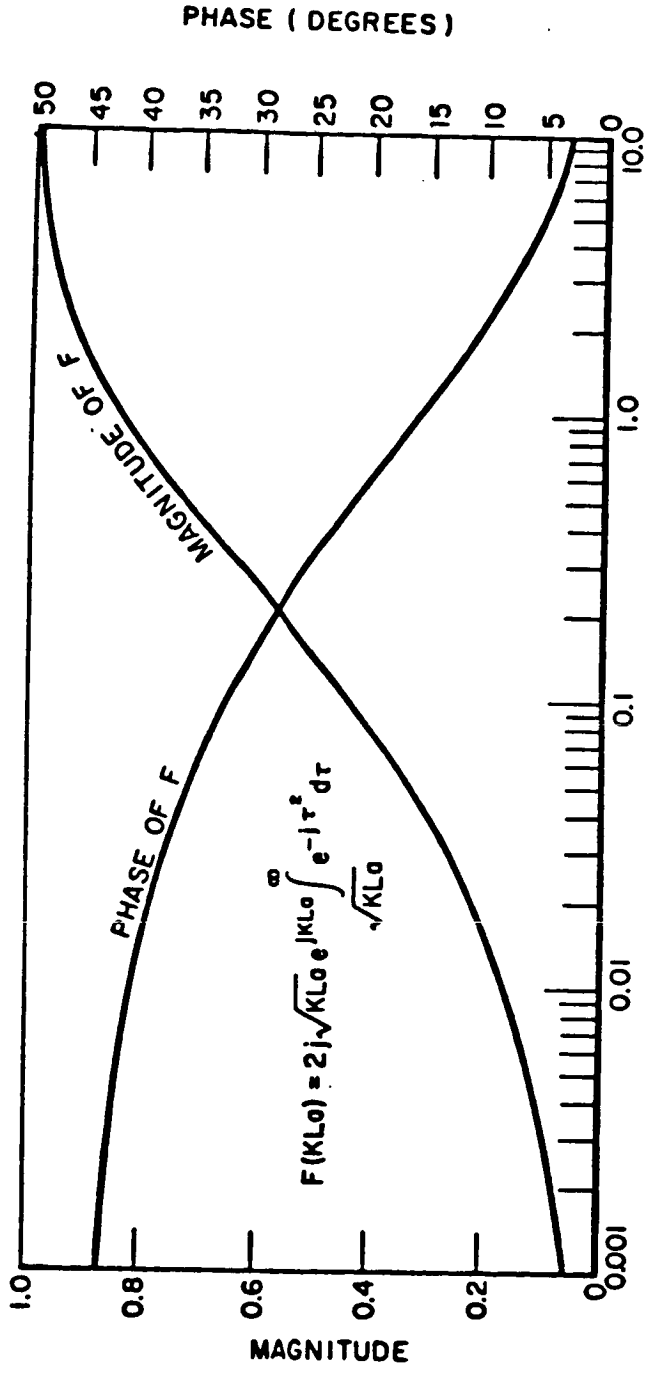

Figure 2.12 Transition function.

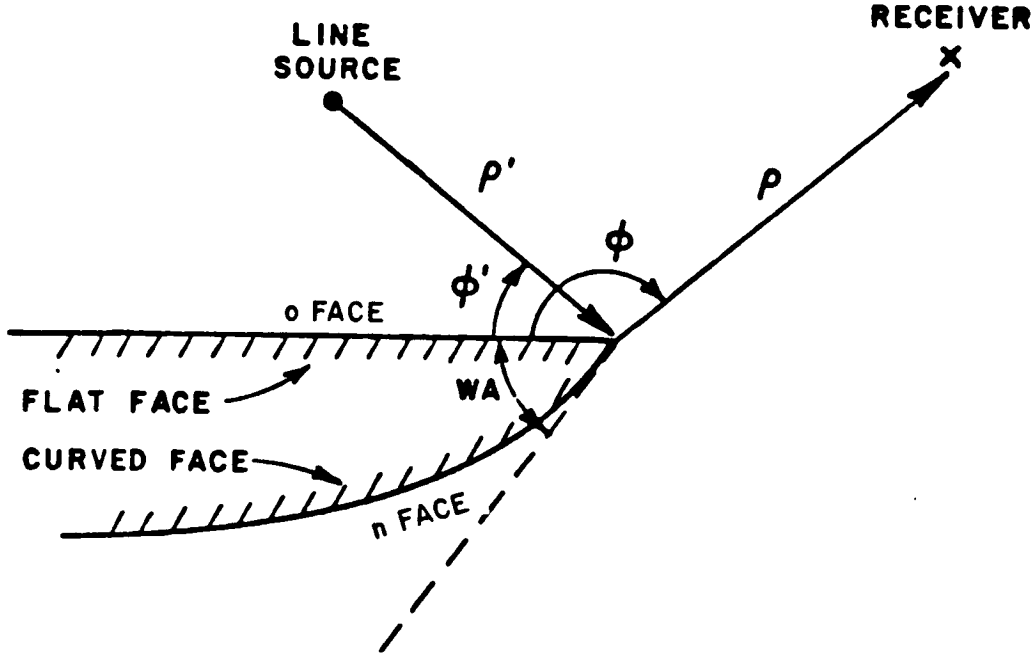

Figure 2.13 One face of a general wedge structure is illuminated.

boundary. The o face is defined as the face where the angles ϕ and ϕ' are measured. The n face is the opposing surface. Also, the range parameters are given by

$$L^{rn} = \frac{\overset{n}{\rho_c}\rho}{\overset{n}{\rho_c}+\rho}, \text{ and} \tag{2.44}$$

$$L^{ro} = \frac{\overset{o}{\rho_c}\rho}{\overset{o}{\rho_c}+\rho} \tag{2.45}$$

where $\overset{n}{\rho_c}$ and $\overset{o}{\rho_c}$ are the caustic distances for the reflected waves emanating from the edge for the n and o faces, respectively. Similarly, two incident shadow boundaries may exist, and two terms are also associated with these. In this case, the range parameter is given by

$$L^{i} = \frac{\rho'\rho}{\rho'+\rho} \tag{2.46}$$

This completes the basic theory and more detailed analysis may be found in the class notes by Burnside [7] for microwave optics. In later chapters some additional details of the theory are needed, and they are presented when needed.

One final technique used in this analysis is physical optics. This involves rather simple analysis and will be described later when actually implemented.

The three analysis techniques may now be compared to see the advantages and disadvantages in each for analyzing the Cassegrain system. The Uniform Geometrical Theory of Diffraction (UTD) requires

analysis of the geometry which may or may not be easily implemented. Including enough terms to accurately predict performance may be difficult but if possible, UTD provides results with very little computation time required. The UTD is also well suited for large electrical objects such as the Cassegrain system. If results are consistent with other techniques, UTD may be used as a valuable design tool because of its high frequency capability and ease of computation. The physical optics technique is also easy to implement and its results may be easily compared with the other techniques. Physical optics is an approximation though, and this is a limitation. Finally, the moment method technique provides the greatest accuracy but at the expense of ease of computation. Much computational work must be done so moment method results require much time and space on a computer. The moment method is also limited by object size. In the case of the large Cassegrain system, this limits the upper frequency that may be examined. Since the moment method provides accurate results, it may be compared with UTD to see what field components are dominant. So the faster UTD may be used to initialize a design and the slower moment method to finalize it. The moment method will also give more accurate results at lower frequencies; whereas, UTD may be used to predict the high frequency behavior.

CHAPTER III

CASSEGRAIN SYSTEM CONSIDERATIONS

A simple single parabolic reflector is considered initially. A line source is placed in the presence of half a parabola (see Figure 3.1) whose focal length is specified by f. The reflected field and the edge diffracted field are examined along a line parallel to the x-axis and a distance f from the origin. All path lengths from the focal point to the reflector and onto this line are equidistant and have a value of 2f implying constant phase across the plane for the reflected field. Now the reflected field in Figure 3.2 is given by the geometrical optics expression such that

$$U^{REF} = \pm\sqrt{\frac{\rho_c}{\rho_c+\rho_r}}\, C\, \frac{e^{-jk\rho_i}}{\sqrt{\rho_i}}\, e^{-jk\rho_r} \quad . \tag{3.1}$$

The caustic distance is given by

$$\frac{1}{\rho_c} = \frac{1}{\rho_i} + \frac{2}{R_c\cos(\pi-\theta_i)} \tag{3.2}$$

where

$$R_c = \left|\frac{1}{\text{CURVATURE}}\right| \quad , \quad \text{and} \tag{3.3}$$

$$\text{CURVATURE} = \frac{y''}{(1+(y')^2)^{3/2}} \quad . \tag{3.4}$$

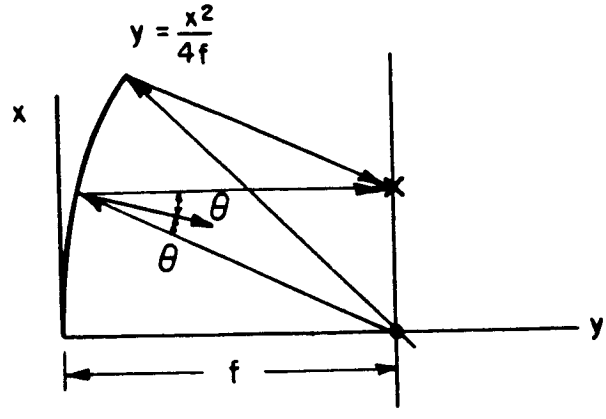

Figure 3.1 Parabolic reflector.

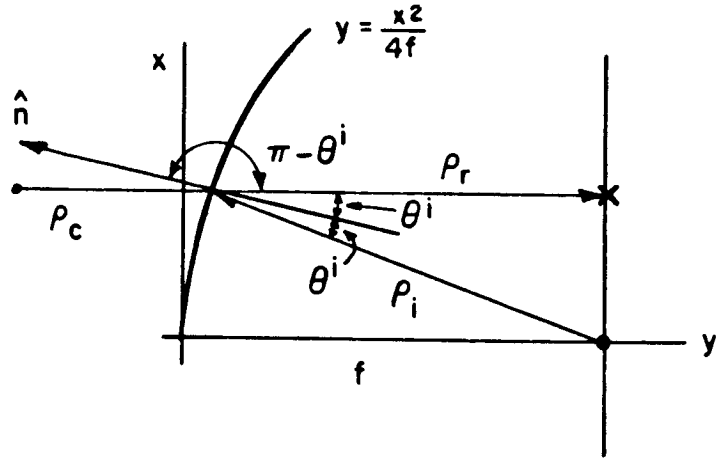

Figure 3.2 Reflected field.

Solving these expressions for R_c, one finds that

$$R_c = \left| 2f(1+x^2/(4f^2))^{3/2} \right| . \qquad (3.5)$$

In addition, one obtains the following:

$$\cos(2\theta_i) = \rho_c/\rho_i$$

$$\cos^2\theta_i = (1 + \cos(2\theta_i)/2$$

$$\cos\theta_i = \sqrt{(1+\rho_r/\rho_i)/2} \ . \qquad (3.6)$$

$$\cos(\pi-\theta_i) = -\cos\theta_i \ , \text{ and} \qquad (3.7)$$

$$\rho_r + \rho_i = 2f \ . \qquad (3.8)$$

Substituting thse into Equation (3.2), one obtains

$$\rho_c = \frac{1}{\frac{1}{\rho_i} - \frac{1}{f\left[1+\frac{x2}{4f^2}\right]^{3/2}\left[\frac{f}{\rho_i}\right]^{1/2}}} \ . \qquad (3.9)$$

Now

$$\rho_r = f - x^2/(4f)$$

or

$$\frac{\rho r}{f} = 1 - \frac{x^2}{4f^2} \ . \qquad (3.10)$$

Substituting this result into Equation (3.9), one finds as expected that

$$\rho_c = \infty \ , \text{ and} \qquad (3.11)$$

$$U^{REF} = \pm c \frac{e^{-jk(\rho_i+\rho_r)}}{\sqrt{\rho_i}} \tag{3.12}$$

with

$$\rho_r = f - x^2/(4f) \quad , \quad \text{and} \tag{3.13}$$

$$\rho_i = \sqrt{x^2 + \rho_r^2} \, . \tag{3.14}$$

Now U^{REF} is known as a function of x.

The edge diffracted field in Figure 3.3 is given by

$$U^{DIFF} = \left[D\left(\frac{\rho'\rho}{\rho'+\rho}, \phi-\phi', n\right) \pm D\left(\frac{\rho_c'\rho}{\rho_c'+\rho}, \phi-\phi', n\right)\right] c \frac{e^{-jk\rho'}}{\sqrt{\rho'}} \frac{e^{-jk\rho}}{\sqrt{\rho}} \, . \tag{3.15}$$

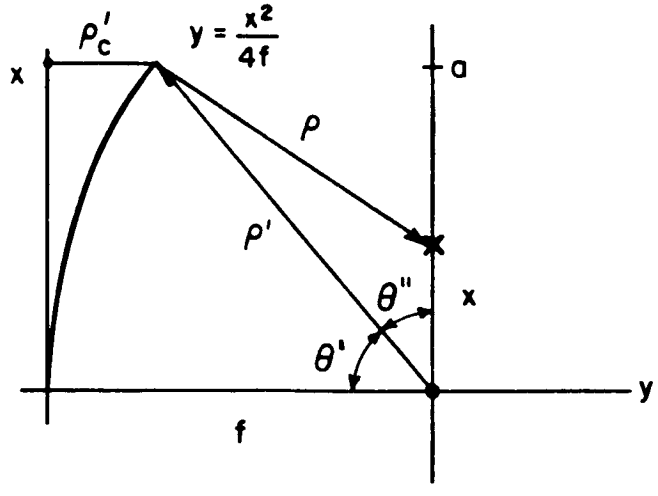

Figure 3.3 Edge diffracted field.

Since n = 2 in this case, one finds that

$$D(L,\beta,n=2) = \frac{-e^{-j\pi/4}}{2\sqrt{2\pi k}} \frac{F(kLa(\beta))}{\cos(\beta/2)} \tag{3.16}$$

$$F(kLa(\beta) = 2j\sqrt{kLa(\beta)}\, e^{jkLa(\beta)} \int_{\sqrt{kLa(\beta)}}^{\infty} e^{-j\tau^2} d\tau, \text{ and} \tag{3.17}$$

$$a(\beta) = 2\cos^2(\beta/2) \quad . \tag{3.18}$$

From Figure 3.3, one obtains

$$\rho' = \sqrt{a^2 + (f - a^2/4f)^2} \text{ , and} \tag{3.19}$$

$$\rho_c' = \infty \tag{3.20}$$

as calculated earlier. Also, the following expressions are found

$$\rho^2 = x^2+(\rho')^2 - 2x\rho'\cos\theta''$$

$$\theta'' = \pi/2 - \theta'$$

$$\theta' = \sin^{-1}(a/\rho')$$

$$\cos(\pi/2 - \theta') = \sin\theta'$$

$$\sin\theta' = a/\rho' \text{ , and}$$

$$\rho = (x^2 + (\rho')^2 - 2xa)^{1/2} \quad . \tag{3.21}$$

Now ϕ' and ϕ need to be determined. From Figure 3.4, one obtains the following:

$$\sin(2\theta^i) = a/\rho'$$

$$\theta^i = 1/2 \sin^{-1}(a/\rho') \tag{3.22}$$

$$\phi' = \pi/2 - \theta^i \tag{3.23}$$

$$x^2 = (\rho')^2 + \rho^2 - 2\rho'\rho\cos\gamma$$

$$\gamma = \cos^{-1}\left(\frac{-x^2+(\rho')^2 + \rho^2}{2\rho'\rho}\right) \qquad (3.24)$$

$$\phi = \phi' + \gamma \qquad (3.25)$$

$$\beta^- = \phi - \phi'$$

$$\beta^- = \gamma \text{ , and} \qquad (3.26)$$

$$\beta^+ = \phi + \phi' \text{ .}$$

Substituting Equations (3.25) and (3.23) into (3.22), one finds that

$$\beta^+ = \pi - \sin^{-1}(a/\rho') + \gamma \text{ .} \qquad (3.27)$$

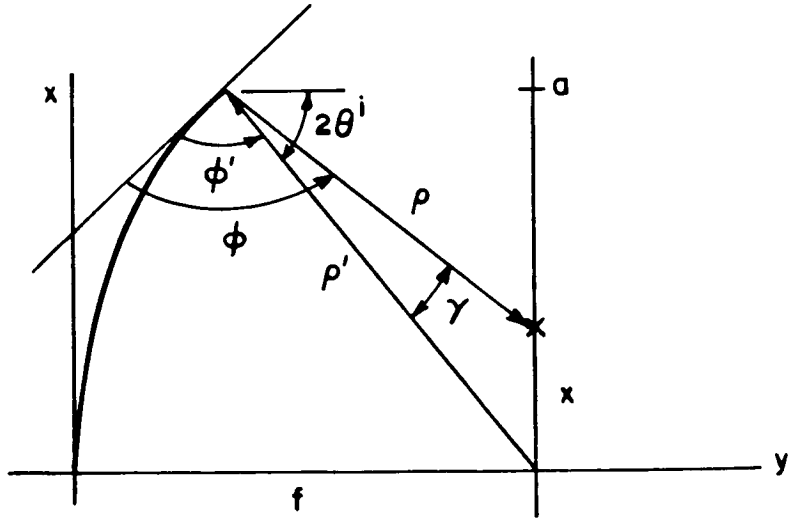

Figure 3.4 Edge diffacted field.

The range parameters are given by

$$L^- = \frac{\rho' \rho}{\rho' + \rho} \quad , \quad \text{and} \tag{3.28}$$

$$L^+ = \frac{\rho_c' \rho}{\rho_c' + \rho} = \rho \tag{3.29}$$

since $\rho_c' = \infty$.

Now the edge diffracted field is known from

$$U^{DIFF} = \frac{-e^{-j\pi/4}}{2\sqrt{2\pi k}} \left(\frac{F(kL^- a(\beta^-))}{\cos(\beta^-/2)} \pm \frac{F(kL^+ a(\beta^+))}{\cos(\beta^+/2)} \right) c \, \frac{e^{-jk(\rho'+\rho)}}{\sqrt{\rho' \rho}} \quad . \tag{3.30}$$

Then the total field is given by $U^{REF} + U^{DIFF}$ in Equations (3.1) and (3.30). A typical plot is given in Figure 3.5.

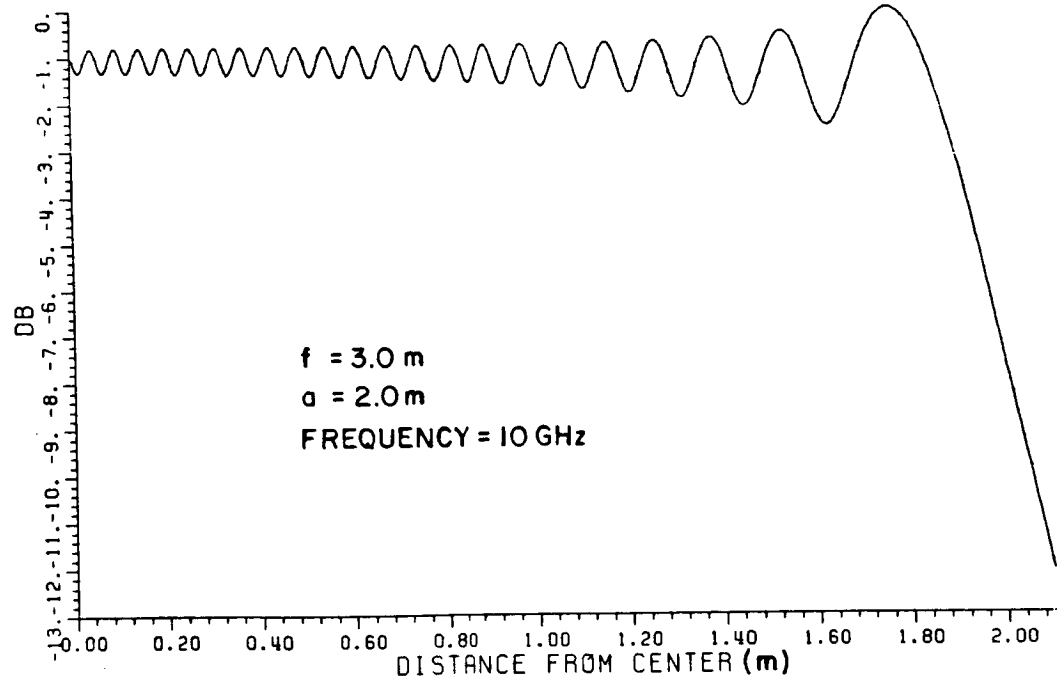

Figure 3.5 $U^{REF} + U^{DIFF}$.

Now the addition of a rolled edge is made to the parabola to reduce the ripple generated by the diffracted field (see Figure 3.6). The diffracted field at the junction must now be recalculated. More generally, one obtains that

$$U^{DIFF} = D_{\substack{S \\ H}} \mu^i(Q_E) \frac{e^{-jk\rho}}{\sqrt{\rho}} \tag{3.31}$$

$$\mu^i(Q_E) = c \frac{e^{-jk\rho'}}{\sqrt{\rho'}} \tag{3.32}$$

$$D_{\substack{S \\ H}} = D(L^i, L^i, \phi-\phi', n) \mp D(L^{rn}, L^{ro}, \phi+\phi', n), \text{ and} \tag{3.33}$$

$$D(L_1, L_2, \phi\pm\phi', n) = \left[\cot\left(\frac{\pi+(\phi\pm\phi')}{2n}\right)F(kL_1a^+(\phi\pm\phi')) + \cot\left(\frac{\pi-(\phi\pm\phi')}{2n}\right)F(kL_2a^-(\phi\pm\phi'))\right] \frac{e^{-j\pi/4}}{2n\sqrt{2\pi k}} . \tag{3.34}$$

The distance given by ρ and ρ' have been previously calculated but the two terms of $D_{\substack{S \\ H}}$ need to be considered. Looking at $D(L^i, L^i, \phi-\phi', n)$, one finds that

$$D(L^i, L^i, \phi-\phi', n) = \frac{-e^{-j\pi/4}}{2n\sqrt{2\pi k}} \left[\cot\left(\frac{\pi+(\phi-\phi')}{2n}\right)F(kL^ia^+(\phi-\phi')) + \cot\left(\frac{\pi-(\phi-\phi')}{2n}\right)F(kL^ia^-(\phi-\phi'))\right] \tag{3.35}$$

with

$$n = 1 \tag{3.36}$$

$$L^i = \frac{\rho'\rho}{\rho'+\rho} \tag{3.37}$$

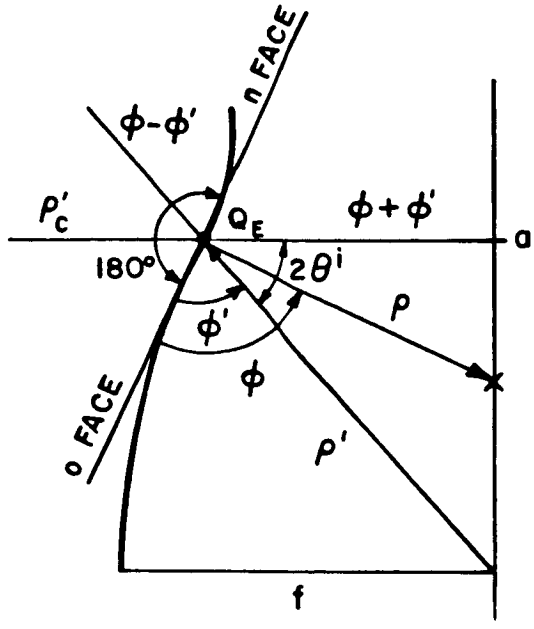

Figure 3.6 Rolled edge addition.

and ϕ and ϕ' are also known. Recall that

$$a^{\pm}(\beta) = 2\cos^2\left(\frac{2n\pi N^{\pm} - (\beta)}{2}\right)$$

where $N^{\pm}$ are integers which most nearly satisfy the following:

$$2\pi n N^{+} - (\beta) = \pi \quad , \text{ and}$$

$$2\pi n N^{-} - (\beta) = -\pi \quad .$$

But n=1, so

$$a^{\pm}(\beta) = 2\cos^2(\pi N^{\pm} - \beta/2) \quad , \text{ or}$$

$$a^{\pm}(\beta) = 2\cos^2(\beta/2)$$

which implies that

$$a^{+}(\beta) = a^{-}(\beta) \quad . \tag{3.38}$$

Inserting Equation (3.38) into (3.35) yields

$$D(L^i,L^i,\phi-\phi',1) = \frac{-e^{-j\pi/4}}{2\sqrt{2\pi k}} \{\cot(\pi/2 +(\phi-\phi')/2) + \cot(\pi/2 -(\phi-\phi')/2)\} F(kL^i a^+(\phi-\phi') \ . \tag{3.39}$$

From the geometry, one finds that

$$\cot(\pi/2 + \alpha) + \cot(\pi/2 - \alpha) = \frac{\cos(\pi/2 + \alpha)}{\sin(\pi/2 + \alpha)} + \frac{\cos(\pi/2 - \alpha)}{\sin(\pi/2 - \alpha)}$$

$$= \frac{-\sin\alpha}{\cos\alpha} + \frac{\sin\alpha}{\cos\alpha}$$

$$= 0 \ .$$

Thus, the incident shadow boundary terms are given by

$$D(L^i,L^i,\phi-\phi',1) = 0 \tag{3.40}$$

Now looking at the remaining terms, one obtains

$$D(L^{rn},L^{ro},\phi+\phi',1) = \frac{-e^{-j\pi/4}}{2\sqrt{2\pi k}} [\cot(\pi/2 + (\phi+\phi')/2)F(kL^{rn}a^+(\phi+\phi')) + \cot(\pi/2 - (\phi+\phi')/2)F(kL^{ro}a^-(\phi+\phi'))]. \tag{3.41}$$

But as before,

$$a^+(\beta) = a^-(\beta) = a(\beta) \ . \tag{3.42}$$

Now

$$L^{ro} = \frac{\rho_c^o \rho}{\rho_c^o + \rho} = \rho \tag{3.43}$$

since ρ_c^o is infinity from previous calculations.

For the n face, one obtains that

$$L^{rn} = \frac{\rho_c{}^n \rho}{\rho_c{}^n + \rho} \quad , \text{ and} \tag{3.44}$$

$$\frac{1}{\rho_c^n} = \frac{1}{\rho'} + \frac{2}{R\cos\theta^i} \quad . \tag{3.45}$$

But ρ' is known and R_c is given leaving

$$\theta^i = 1/2 \sin^{-1}(a/\rho')$$

or

$$\cos\theta^i = \cos[1/2 \sin^{-1}(a/\rho')] \quad . \tag{3.46}$$

Note that ρ_c^n is known from Equation (3.45) and L^{rn} from Equation (3.44). Finally $\phi+\phi'$ is given by Equation (3.27) and the diffraction coefficient is known from Equation (3.41). The diffracted field is then obtained using Equation (3.31). Again the reflected field and recalculated diffracted field are summed for various radii of curvature. In Figure 3.7, the reduction in ripple is evident with increasing radii of curvature. The discontinuity at the edge is also apparent resulting from the absence of the edge reflected field.

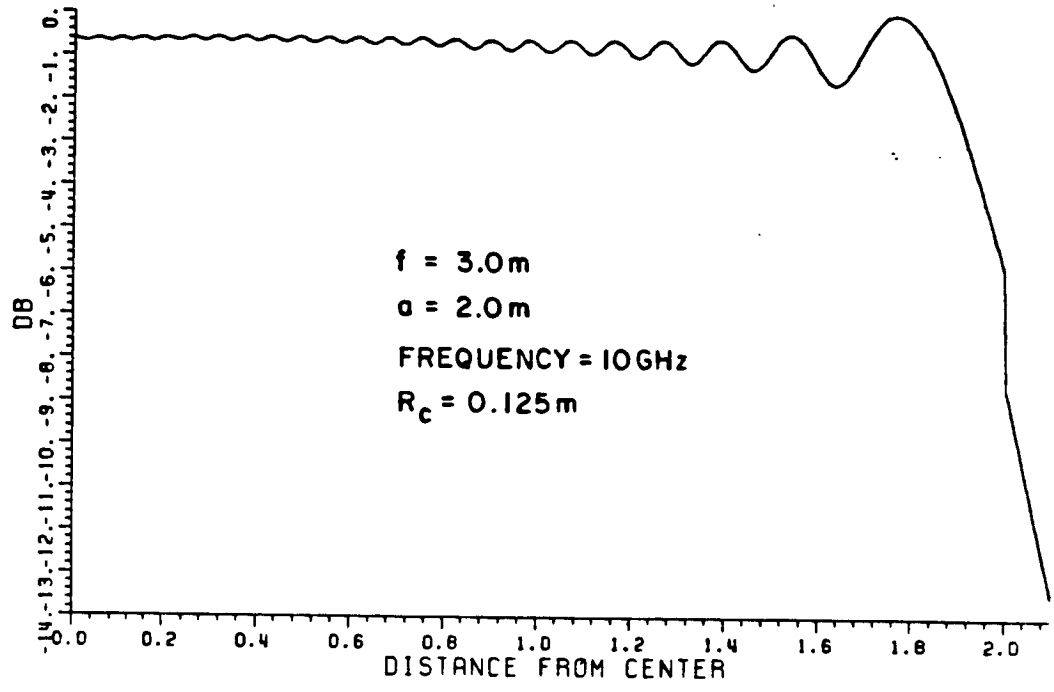

(a) R_c = 0.125 m.

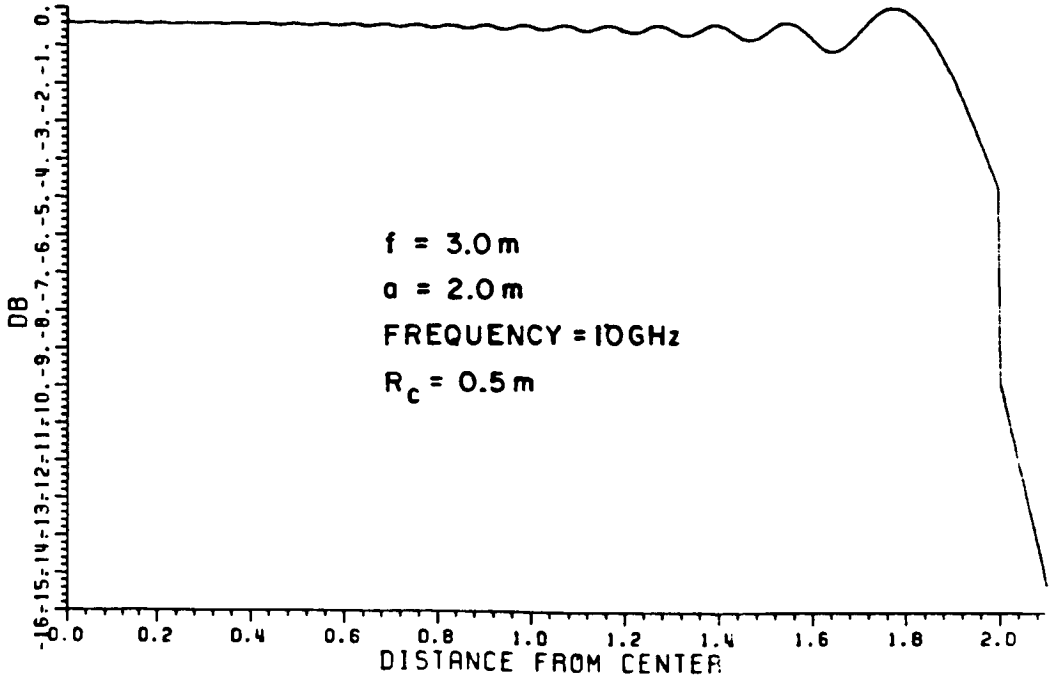

(b) R_c = 0.5 m.

Figure 3.7 $U^{REF} + U^{DIFF}$.

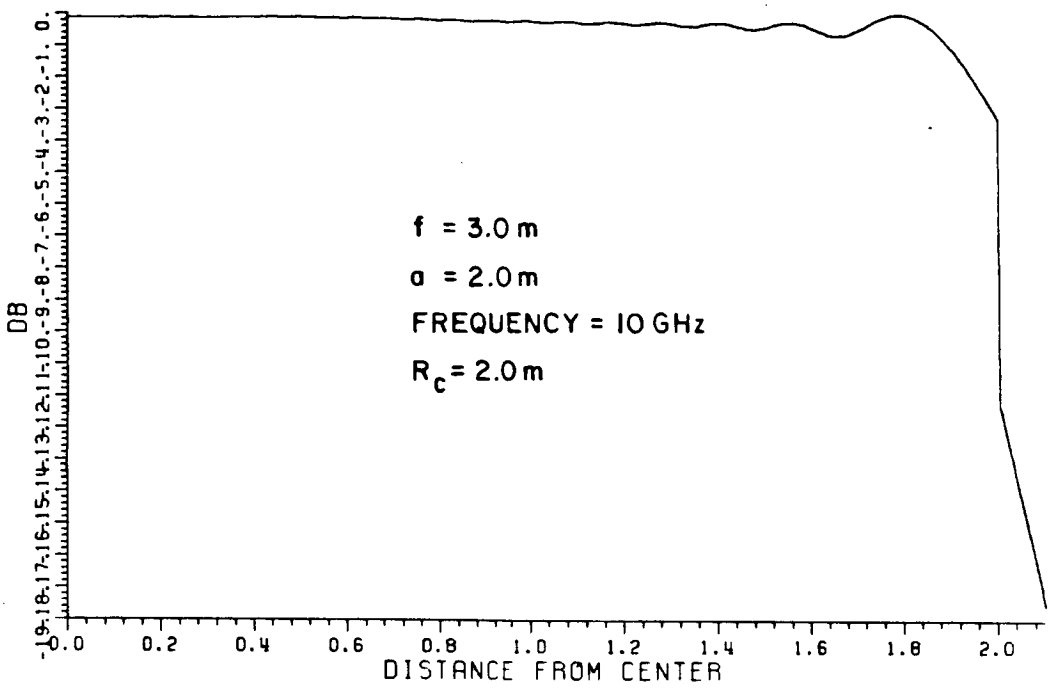

(c) R_c = 2.0m.

Figure 3.7 (Continued).

Now consider the Cassegrain system. The governing equations have previously been described in the theory section. Again, the reflected field is analyzed first (see Figure 3.8) and is given by

$$U_1^{REF} = \sqrt{\frac{\rho_{c1}}{\rho_{c1}+\rho_{r1}}}\, c\, \frac{e^{-jk\rho_i}}{\sqrt{\rho_i}}\, e^{-jk\rho_i} . \tag{3.47}$$

The reflected field caustic position is calculated easily from the following geometrical considerations:

$$\rho_{c1}^2 = (Lv-x_s)^2 + y_s^2 \tag{3.48}$$

$$\rho_i^2 = y_s^2 + (Fc-Lv+x_s)^2 \text{ , and} \tag{3.49}$$

$$\rho_{r1}^2 = (y_m-y_s)^2 + (\rho_{r2} - (Lv-x_s))^2 . \tag{3.50}$$

Now it is necessary to relate y_s in terms of y_m, the desired field point. First, one obtains that

$$\rho_{r2} = Fm - y_m^2/(4Fm) \tag{3.51}$$

$$x_s = a\,[\sqrt{1 + (y_s/b)^2} - 1]\ , \text{ and} \tag{3.52}$$

$$\tan\alpha = \frac{\rho_{r2}}{y_m} = \frac{Lv - x_s}{y_s}\ . \tag{3.53}$$

Substituting Equations (3.51) and (3.52) into (3.53) yields

$$y_s = \frac{Lv + a - a\sqrt{1 + \dfrac{Lv^2 + 2aLv}{(bc_1)^2}}}{c_1 - (1/c_1)(a/b)^2} \tag{3.54}$$

where

$$c_1 = \frac{F_m}{y_m} - \frac{y_m}{4f_m}\ . \tag{3.55}$$

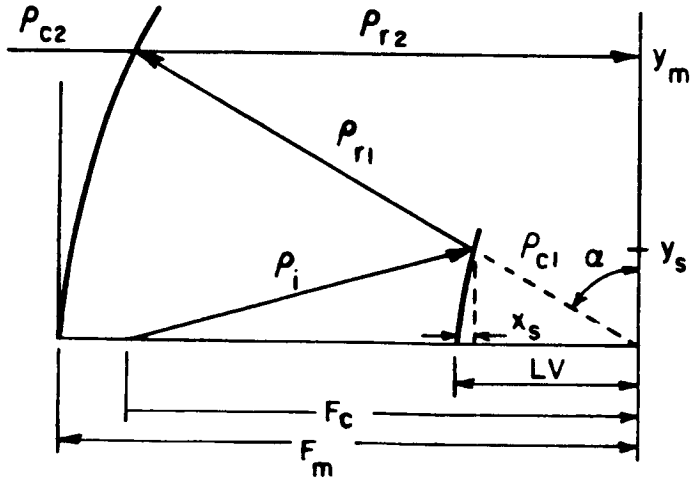

Figure 3.8 Reflected field.

So now ρ_{c1}, ρ_i, and ρ_{r1} are in terms of y_m, and U_1^{REF} may be calculated from Equation (3.47). Then, the reflected field along the observation line is given by

$$U_2^{REF} = U_1^{REF} e^{-jk\rho_{r2}} \tag{3.56}$$

since $\rho_{c2} = \infty$. Note that ρ_{r2} is given by Equation (3.51).

The diffracted field from the main reflector edge is computed now. As with the parabolic problem, one finds that

$$U_1^{DIFF} = U_{1E}^{REF} \frac{e^{-j\kappa\rho}}{\sqrt{\rho}} \left[D\left(\frac{(\overset{E}{\rho}_{r1}+\overset{E}{\rho}_{c1})\rho}{\overset{E}{\rho}_{r1}+\overset{E}{\rho}_{c1}+\rho}, \phi+\phi', n\right) + D\left(\frac{\rho_{c2}\rho}{\rho_{c2}+\rho}, \phi+\phi', n\right)\right] \tag{3.57}$$

where

$$U_{1E}^{REF} = \sqrt{\frac{\overset{E}{\rho}_{c1}}{\overset{E}{\rho}_{c1}+\overset{E}{\rho}_{r1}}}\; c\, \frac{e^{-jk\overset{E}{\rho}_i}}{\sqrt{\overset{E}{\rho}_i}}\, e^{-jk\overset{E}{\rho}_{r1}} \tag{3.58}$$

$$\overset{E}{\rho}_c = \sqrt{(Lv-\overset{E}{x}_s)^2+(Ds/2)^2} \tag{3.59}$$

$$\overset{E}{x}_s = a\left[\sqrt{1+\left(\frac{Ds/2}{b}\right)^2}-1\right] \tag{3.60}$$

$$\overset{E}{\rho}_i = \sqrt{(Ds/2)^2 + (Fc-Lv+\overset{E}{x}_s)^2} \tag{3.61}$$

$$\rho_{r1}^{E} = \sqrt{(Dm/2-Ds/2)^2 + (\rho_{r2}^{E}-(Lv-x_s^{E}))^2} \quad , \text{ and} \tag{3.62}$$

$$\rho_{r2}^{E} = Fm - \frac{(Dm/2)^2}{4fm} \quad . \tag{3.63}$$

Again, the diffraction coefficient consists of terms as follows:

$$D(L,\beta,n=2) = \frac{-e^{-j\pi/4}}{2\sqrt{2\pi k}} \frac{F(kLa(\beta))}{\cos(\beta/2)} \tag{3.16}$$

and

$$a(\beta) = 2\cos^2(\beta/2) \quad . \tag{3.18}$$

From parabolic edge calculations, one obtains that

$$\rho = (y_m^2 + (\rho_{r1}^{E}+\rho_{c1}^{E})^2 - y_m Dm)^{1/2} \tag{3.64}$$

$$\rho_{c2} = \infty \, ,$$

$$\beta^- = \phi - \phi'$$

$$\beta^- = \cos^{-1} \left[\frac{-y_m^2+(\rho_{r1}^{E}+\rho_{c1}^{E})^2 + \rho^2}{2(\rho_{r1}^{E}+\rho_{c1}^{E})\rho}\right] \tag{3.65}$$

$$\beta^+ = \phi + \phi'$$

$$\beta^+ = \pi - \sin^{-1} \frac{Dm}{2(\rho_{r1}^{E}+\rho_{c1}^{E})} + \beta^- \tag{3.66}$$

$$L^- = \frac{(\rho_{r1}^{E}+\rho_{c1}^{E})\rho}{(\rho_{r1}^{E}+\rho_{c1}^{E}+\rho)} \, , \text{ and} \tag{3.67}$$

$$L^+ = \rho \tag{3.68}$$

since $\rho_{c2} = \infty$. So finally, the diffracted field is given by

$$U_1^{DIFF} = U_{1E}^{REF} \frac{e^{-jk\rho}}{2\sqrt{\rho}} \cdot \frac{-e^{-j\pi/4}}{2\sqrt{2\pi k}} \left[\frac{F(kL^-a(\beta^-))}{\cos(\beta^-/2)} + \frac{F(kL^+a(\beta^+))}{\cos(\beta^+/2)}\right] . \tag{3.69}$$

The sum of U_2^{REF} and U_1^{DIFF} is shown in Figure 3.9 for one example.

Another major field component is the diffracted reflected field from the subreflector edge (see Figure 3.10). This field is given by

$$U_2^{DIFF} = \sqrt{\frac{\rho_c}{\rho_c+\rho_2}} \{ c \frac{e^{-jk\rho_i^E}}{\sqrt{\rho_i^E}} \frac{e^{-jk\rho_1}}{\sqrt{\rho_1}} [D(\frac{\rho_i^E \rho_1}{\rho_i^E+\rho_1}, \phi-\phi', 2)$$

$$+ D(\frac{\rho_c^E \rho_1}{\rho_c^E+\rho_1}, \phi+\phi', 2)]\} e^{-jk\rho_2} \tag{3.70}$$

with

$$D(L, \beta, n=2) = \frac{-e^{-j\pi/4}}{2\sqrt{2\pi k}} \frac{F(kLa(\beta))}{\cos(\beta/2)} \tag{3.16}$$

and

$$a(\beta) = 2\cos^2(\beta/2) . \tag{3.18}$$

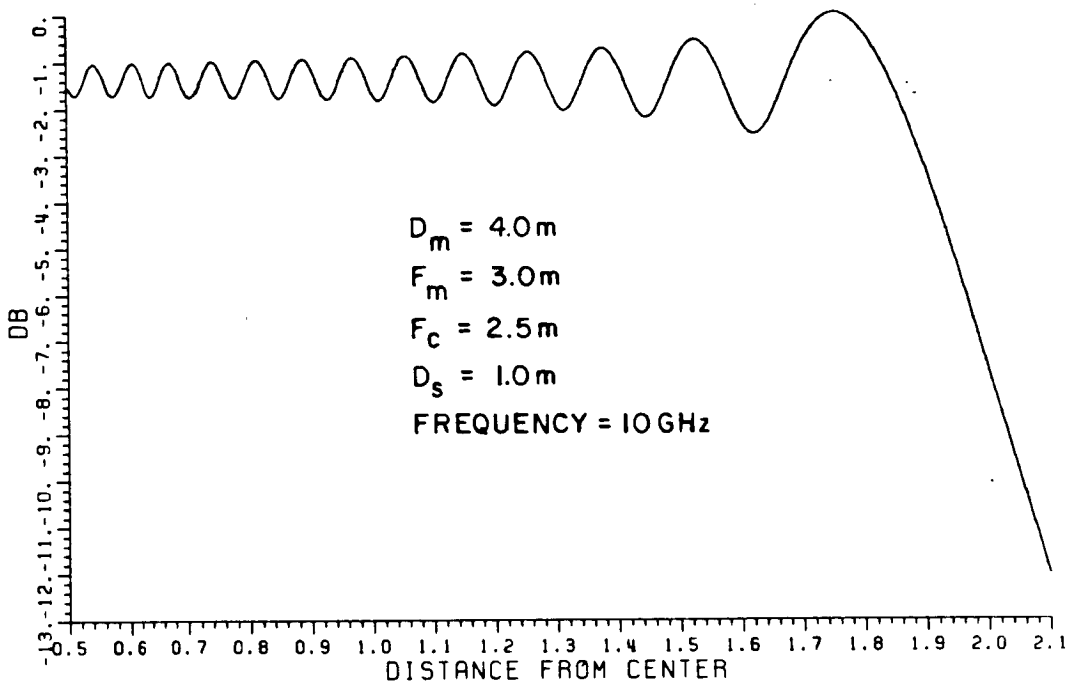

Figure 3.9 $U_2^{REF} + U_1^{DIFF}$.

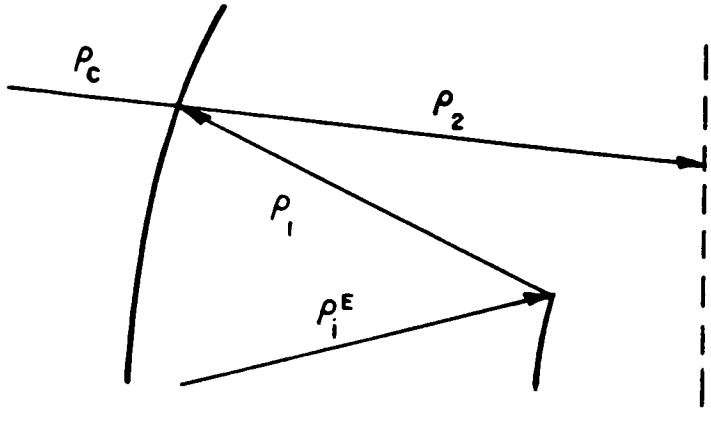

Figure 3.10 Subreflector diffracted field.

The geometry for this field analysis is given in Figure 3.11. The needed relationships between the various parameters are given as follows:

$$X_m^E = (Dm/2)^2/(4Fm) \tag{3.71}$$

$$s^2 = (X_m^E - (Fm-Fc)^2)^2 + (Dm/2)^2 \tag{3.72}$$

$$\theta^i = 1/2 \cos^{-1}\left[\frac{(\rho_i^E)^2+(\rho_{r1}^E)^2-s^2}{2\rho_i^E\rho_{r1}^E}\right] \tag{3.73}$$

$$\phi' = \frac{\pi}{2} - \theta_i \tag{3.74}$$

$$(s')^2 = y_m^2 + (Fm-Fc-y_m^2/(4Fm)^2 \tag{3.75}$$

$$\beta^- = \phi-\phi' = \cos^{-1}\left[\frac{(\rho_i^E)^2+(\rho_1)^2-(s')^2}{2\rho_i^E\rho_1}\right] \tag{3.76}$$

$$\beta^+ = \phi+\phi' = \beta^- +\pi-2\theta_i \tag{3.77}$$

$$L^- = \frac{\rho_i^E\rho_1}{\rho_i^E+\rho_1} \quad , \quad \text{and} \tag{3.78}$$

$$L^+ = \frac{\rho_c^E\rho_1}{\rho_c^E+\rho_1} \quad . \tag{3.79}$$

Now ρ_c in Figure 3.12 is given by

$$\frac{1}{\rho_c} = \frac{1}{\rho_1} + \frac{2}{R_c\cos(\pi-\theta_i)} \tag{3.80}$$

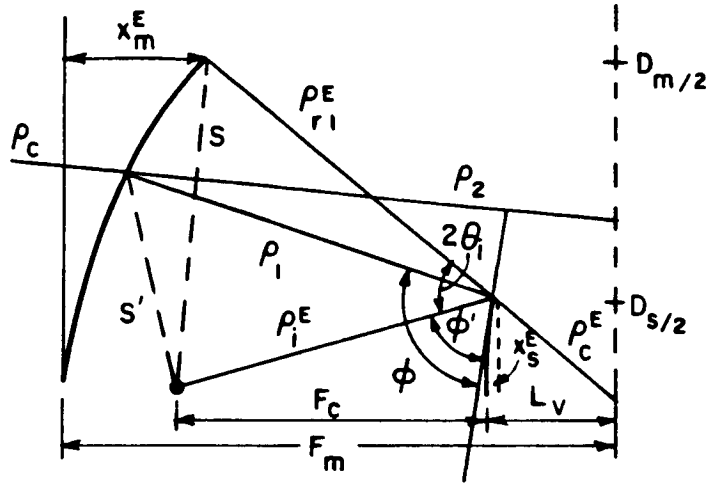

Figure 3.11 Subreflector diffracted field.

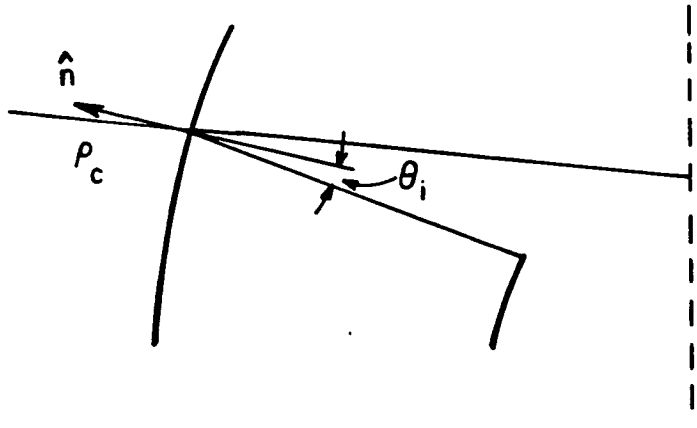

Figure 3.12 Caustic distance.

and

$$R_c = \left| 2Fm(1+y_m^2/(4Fm^2)^{3/2} \right| \tag{3.81}$$

from Equation (3.5). The reflection point is found from an iterative routine given in Appendix A. Now U_2^{DIFF} is known from Equation (3.70). The sum of U_2^{REF}, U_1^{DIFF} and U_2^{DIFF} is given in Figure 3.13 as a sample geometry.

The discontinuity in Figure 3.13 may be alleviated somewhat by extending the subreflector and reducing doubly diffracted fields (see Figure 3.14). The subreflector size is now determined by ϕ_S; whereas, D_E may be found from

$$TAN\phi_S = \left. \frac{D_E/2}{Lv-xs} \right|_{D_E/2} . \tag{3.82}$$

Inserting the system parameters into this equation and solving for D_E yields

$$D_E = (TAN\phi_S) \frac{[a+Lv \pm \sqrt{a^2+(2aLv+Lv^2)((a^2TAN^2\phi s)/b^2)}]}{\frac{1}{2} - \frac{a^2TAN^2\phi_S}{2b^2}} \tag{3.83}$$

with the minus sign giving the desired solution.

The diffracted reflected field may now be recalculated (see Figure 3.15) using

$$x_s^{DEED} = a\left[\sqrt{1+\left(\frac{DE/2}{b}\right)^2} - 1\right] \tag{3.84}$$

$$\rho_i^{DEED} = \sqrt{(D_E/2)^2 + (Fc-Lv+x_s^{DEED})^2} \tag{3.85}$$

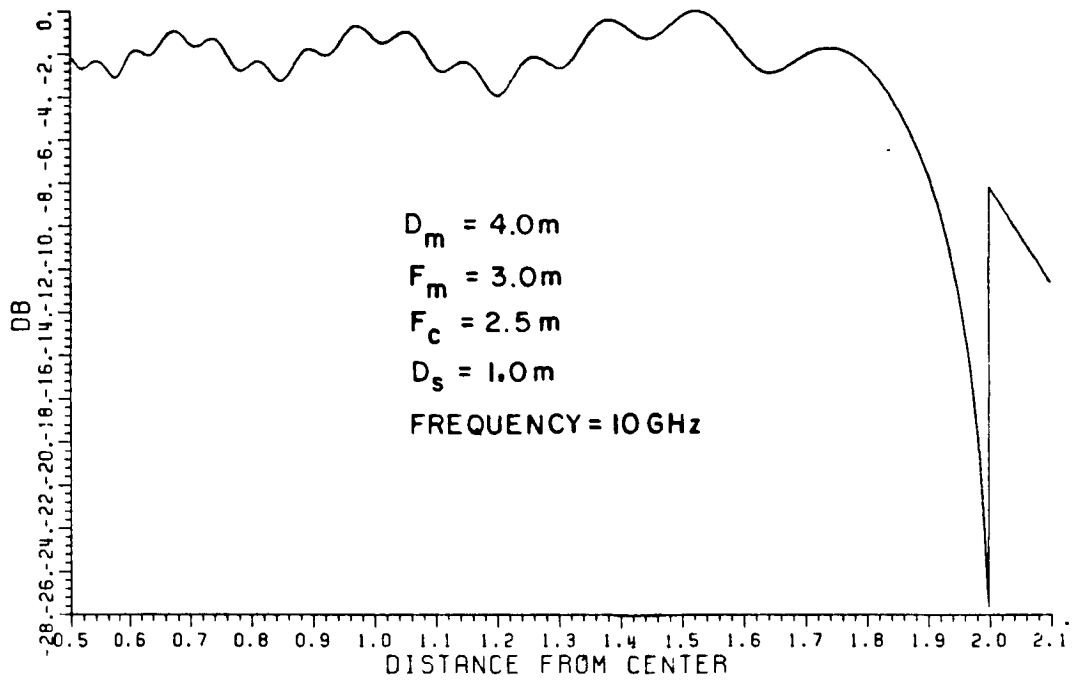

Figure 3.13 $U_2^{REF} + U_1^{DIFF} + U_2^{DIFF}$.

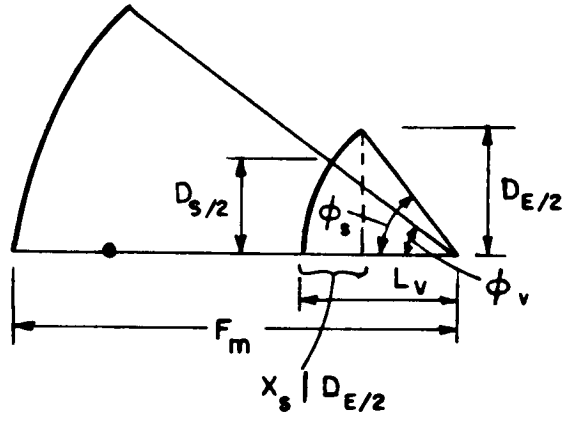

Figure 3.14 Subreflector extension.

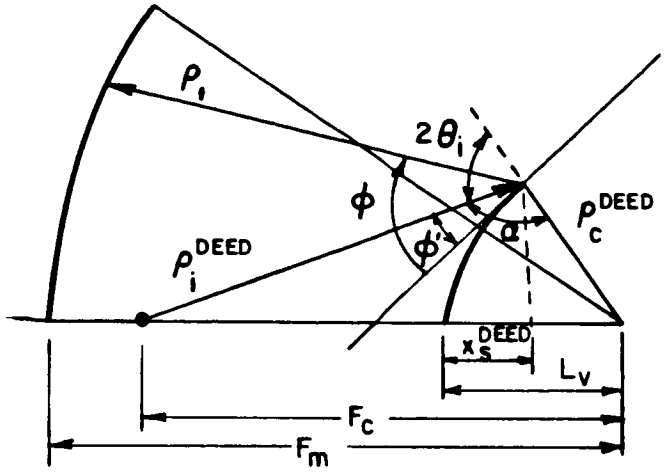

Figure 3.15 Subreflector diffracted field.

$$\rho_c^{DEED} = \sqrt{(D_E/2)^2 + (L_v - x_s^{DEED})^2} \quad , \text{ and} \tag{3.86}$$

$$U_2^{DIFF} = \sqrt{\frac{\rho_c}{\rho_c+\rho_2}}\left\{ c\, \frac{e^{-jk\rho_i^{DEED}}}{\sqrt{\rho_i^{DEED}}} \frac{e^{-jk\rho_1}}{\sqrt{\rho_1}} \left[D\left(\frac{\rho_i^{DEED}\rho_1}{\rho_i^{DEED}+\rho_1}, \phi-\phi', 2\right)\right.\right.$$

$$\left.\left. + D\left(\frac{\rho_c^{DEED}\rho_1}{\rho_c^{DEED}+\rho_1}, \phi+\phi', 2\right)\right]\right\} e^{-jk\rho_2} \, . \tag{3.87}$$

In this case, one finds that

$$2\theta_i = \pi - \alpha$$

where

$$\alpha = \cos^{-1}\left[\frac{(\rho_i^{DEED})^2 + (\rho_c^{DEED})^2 - F_c^2}{2\rho_i^{DEED}\rho_c^{DEED}}\right] \, . \tag{3.88}$$

In addition,

$$\phi' = \pi/2 - \theta_i . \tag{3.90}$$

Again, β^- is given by Equation (3.76); whereas,

$$\beta^+ = \phi+\phi' = \beta^-+\alpha . \tag{3.91}$$

The sum of U_2^{REF}, U_1^{DIFF} and U_2^{DIFF} is again shown in Figure 3.16. The reduction in the discontinuity is obvious.

To reduce the ripple, a rolled edge is now attached to the main reflector (see Figure 3.17). The analysis is similar to the single reflector design discussed previously. First, the diffracted is given by

$$U_1^{DIFF} = D\, U^i(Q_E)\frac{e^{-jk\rho}}{\sqrt{\rho}} \tag{3.92}$$

and

$$U^i(Q_E) = U_1^{REF}\Big|_{Q_E} \tag{3.93}$$

which is known from Equation (3.58) and those that follow. Again, one obtains the following:

$$L^{ro} = \rho \tag{3.94}$$

$$L^{rn} = \frac{\rho_c^n \rho}{\rho_c^n+\rho} \tag{3.95}$$

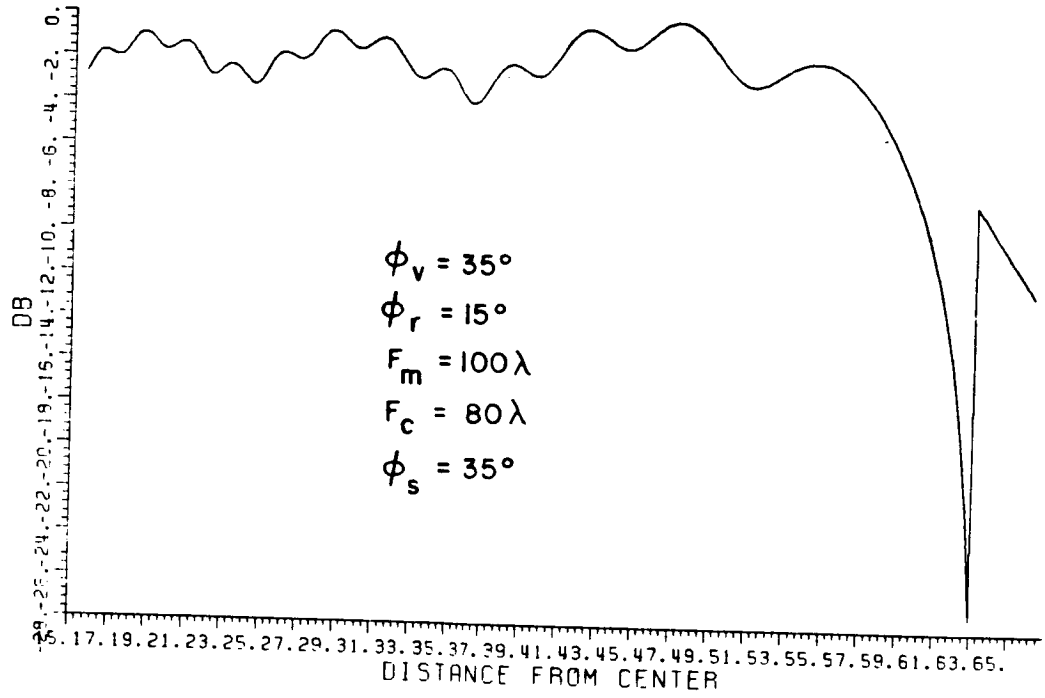

(a) $\phi_S = 35°$.

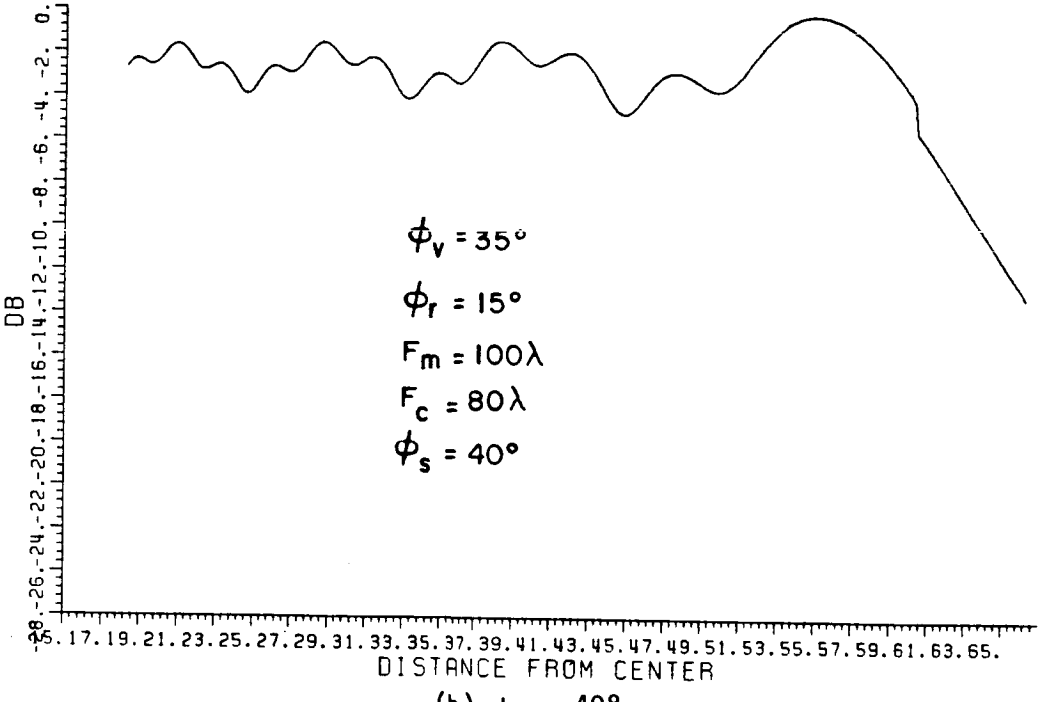

(b) $\phi_S = 40°$.

Figure 3.16 $U_2REF + U_1DIFF + U_2DIFF$.

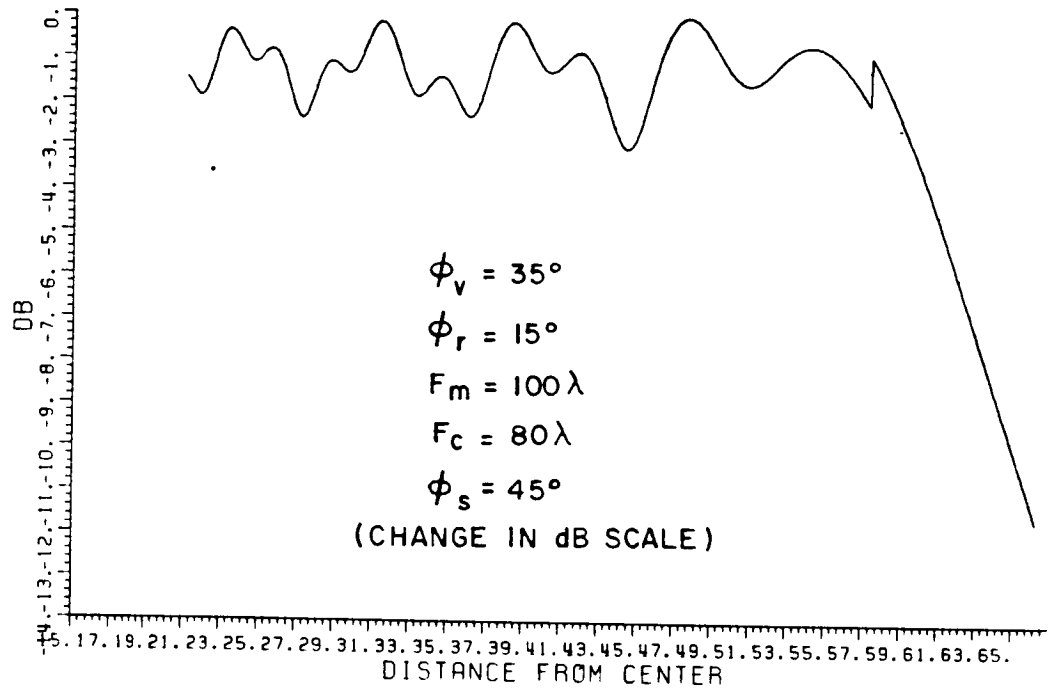

(c) $\phi_S = 45°$.

Figure 3.16 (Continued).

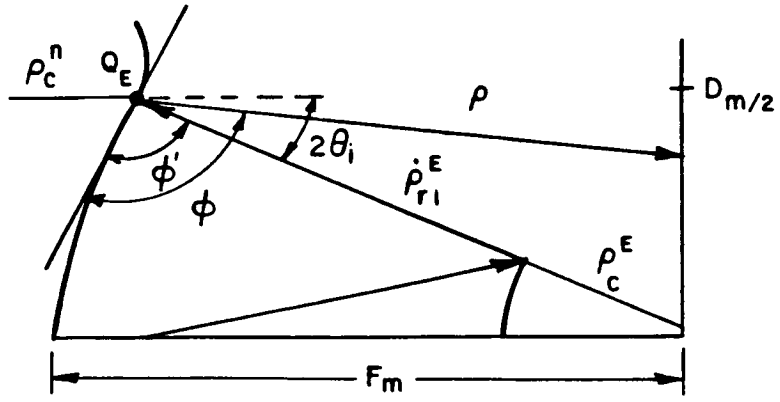

Figure 3.17 Rolled edge addition to main reflector.

$$\frac{1}{\rho_c^n} = \frac{1}{\rho_i} + \frac{1}{R_c \cos\theta_i} \tag{3.96}$$

$$\rho_i = \rho_c^E + \rho_{r1}^E \text{ , and} \tag{3.97}$$

$$\theta_i = \frac{1}{2} \sin^{-1} \frac{Dm}{2\rho_i} \text{ .} \tag{3.98}$$

Then, the diffraction coefficient is given by

$$D = \frac{-e^{-j\pi/4}}{2\sqrt{2\pi k}} [\cot(\pi/2 + (\phi+\phi')/2)F(kL^{rn}a(\phi+\phi')) + \cot(\pi/2 - (\phi+\phi')/2)F(kL^{ro}a(\phi+\phi'))] \tag{3.99}$$

and U_1^{DIFF} is known from Equation (3.92). The effect of increasing R_c on the reduction of the fast varying ripple is shown in Figure 3.18.

The slow varying ripple may now be reduced by attaching a rolled edge to the subreflector (see Figure 3.19). In this case, one finds that

$$U_2^{DIFF} = \sqrt{\frac{\rho_c}{\rho_c+\rho_2}}\, U^{DIFF}\, e^{-jk\rho_2} \tag{3.100}$$

where

$$U^{DIFF} = c\, \frac{e^{-jk\rho_i^{DEED}}}{\sqrt{\rho_i^{DEED}}} \frac{e^{-jk\rho_1}}{\sqrt{\rho_1}} D. \tag{3.101}$$

In addition, the range parameters are given by

$$L^{ro} = \frac{\rho_c^{DEED}\, \rho_1}{\rho_c^{DEED} + \rho_1} \tag{3.102}$$

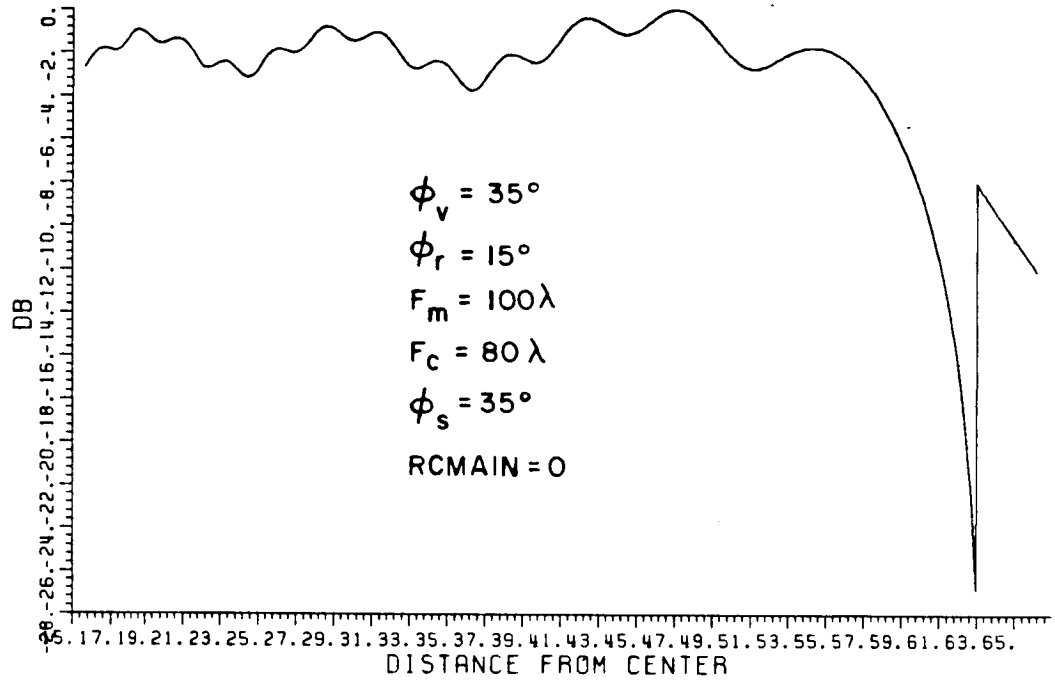

(a) R_cMAIN = 0.

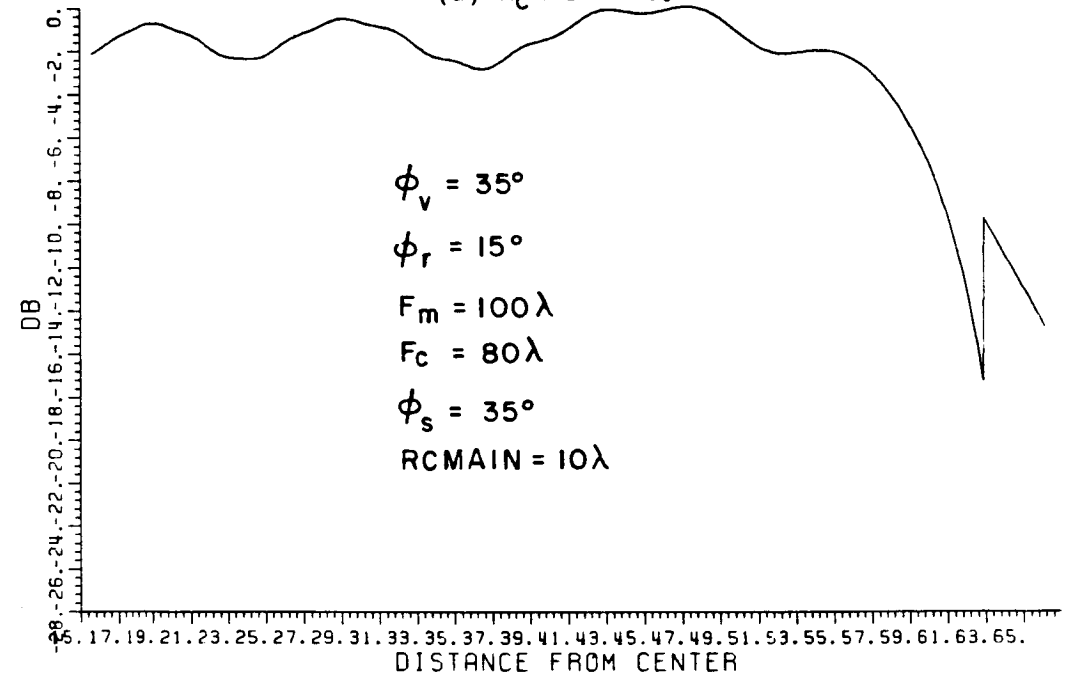

(b) R_cMAIN = 10λ.

Figure 3.18 $U_2^{REF} + U_1^{DIFF} + U_2^{DIFF}$.

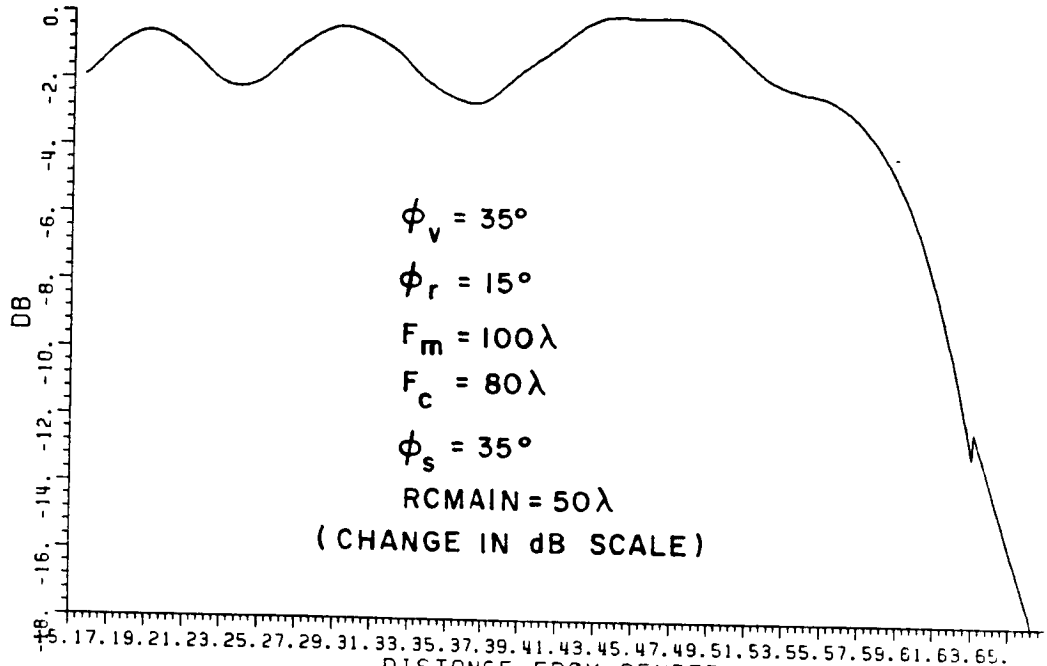

(c) R_cMAIN = 50λ.

Figure 3.18 (Continued).

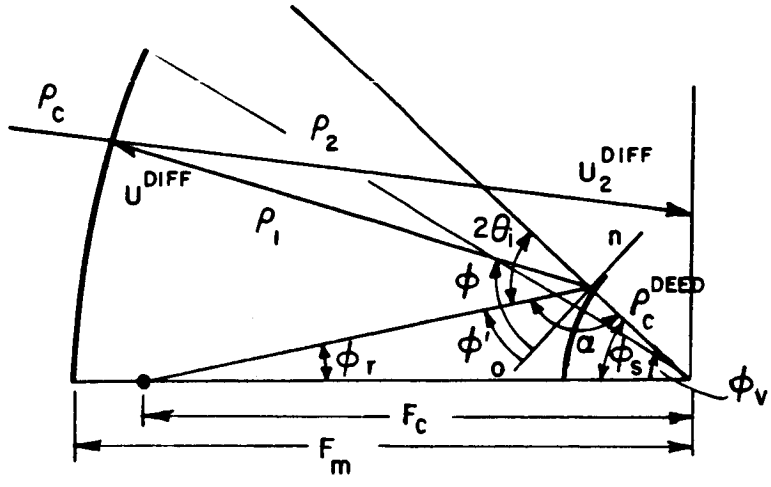

Figure 3.19 Rolled edge addition to subreflector.

$$L^{rn} = \frac{\rho_c^n \rho_1}{\rho_c^n + \rho_1} \quad , \text{ and} \tag{3.103}$$

$$\frac{1}{\rho_c^n} = \frac{1}{\rho_i^{DEED}} + \frac{2}{R_c \cos\theta_i} \quad . \tag{3.104}$$

As before,

$$2\theta_i = \pi - \alpha \tag{3.105}$$

where

$$\alpha = \cos^{-1}\left[\frac{(\rho_i^{DEED})^2 + (\rho_c^{DEED})^2 - Fc^2}{2\rho_i^{DEED}\,\rho_c^{DEED}}\right] . \tag{3.106}$$

The diffraction coefficient is given by

$$D = \frac{-e^{-j\pi/4}}{2\sqrt{2\pi k}}\left[\cot(\pi/2 + (\phi+\phi')/2)F(kL^{rn}a(\phi+\phi')\right.$$

$$\left. + \cot(\pi/2 - (\phi+\phi')/2)F(kL^{ro}a(\phi+\phi'))\right] \tag{3.107}$$

and β^- is given by Equation (3.76) and

$$\beta^+ = \phi+\phi' = \beta^-+\alpha \quad . \tag{3.108}$$

The new diffracted reflected field is then given by Equation (3.100). The effect of increasing R_c on the reduction of the slow ripple is shown in Figure 3.20.

Another field component that needs to be considered is the reflected-reflected-diffracted field (see Figure 3.21). U_1^{REF} has been computed previously and is given by

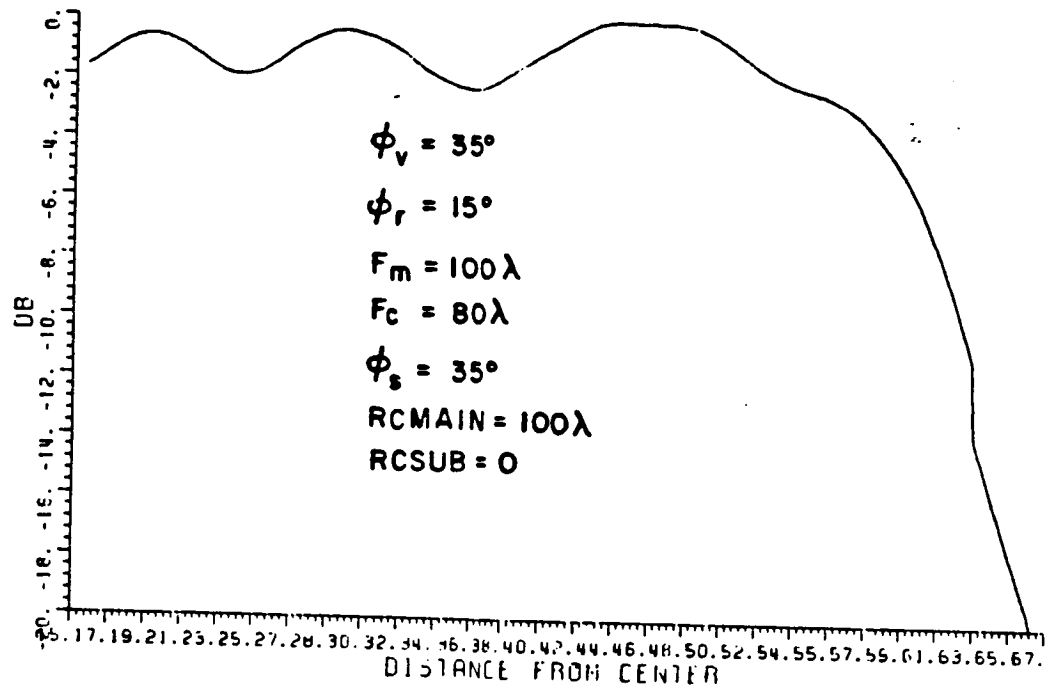

(a) R_CSUB = 0.

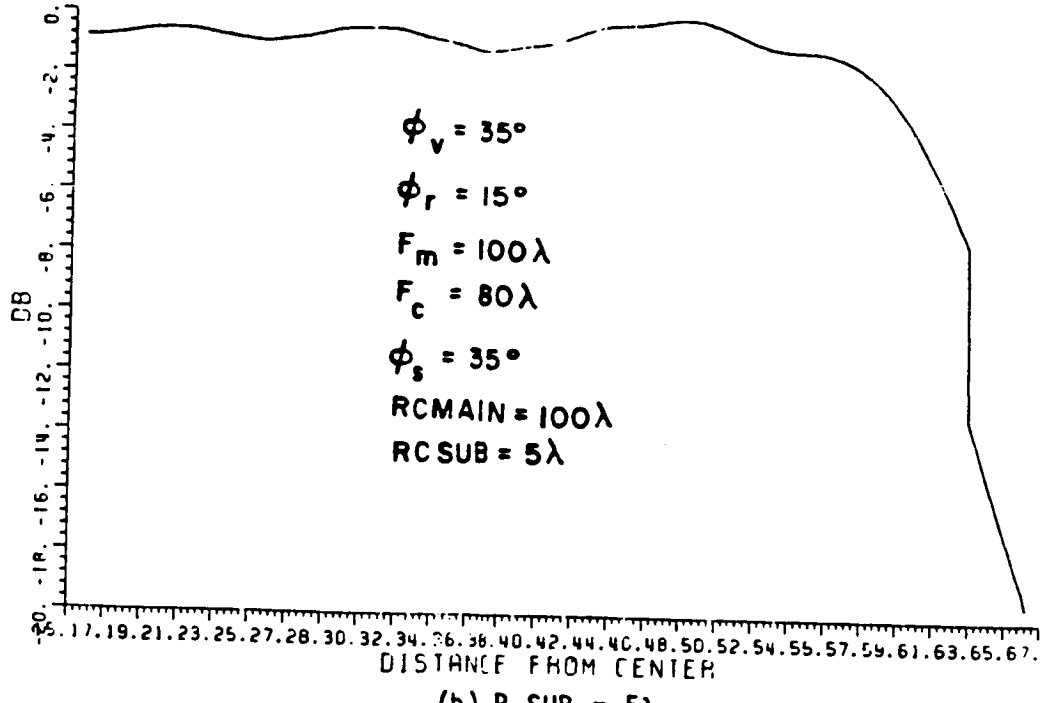

(b) R_CSUB = 5λ.

Figure 3.20 U_2^{REF} + U_1DIFF + U_2DIFF.

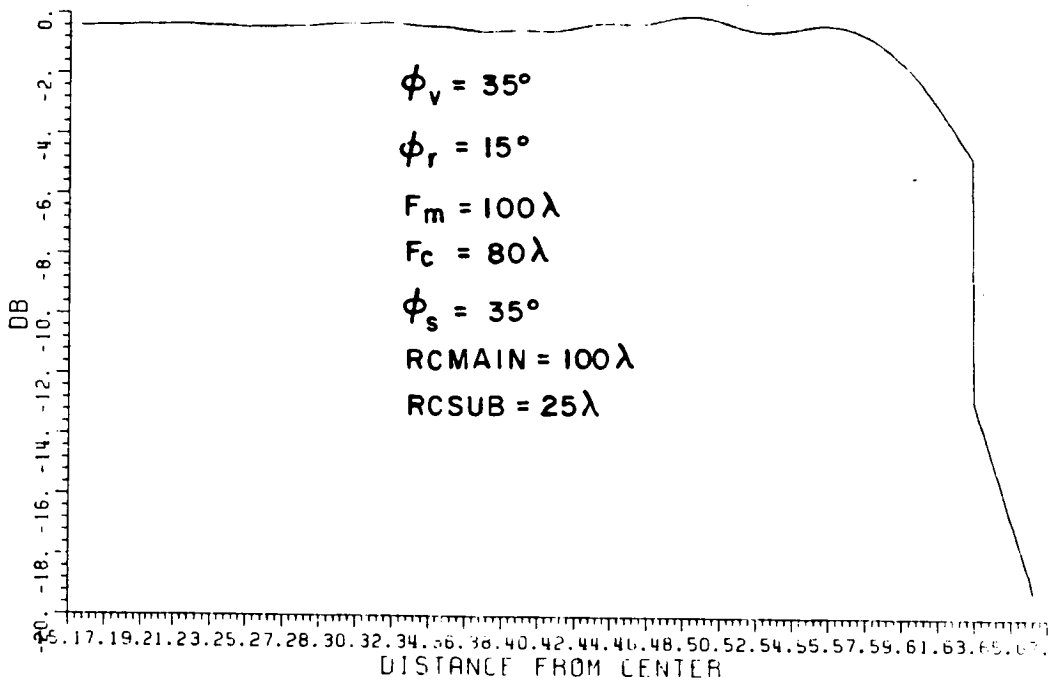

(c) R_cSUB = 25λ.

Figure 3.20 (Continued).

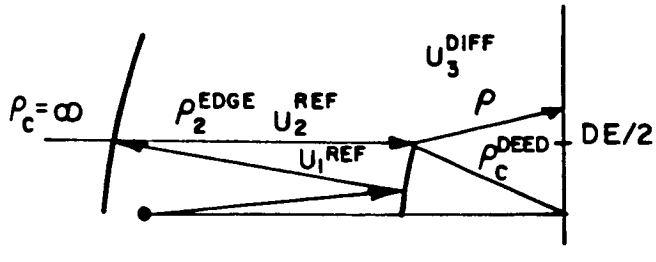

Figure 3.21 Reflected-reflected-diffracted field.

$$U_2^{REF} = U_1^{REF}\, e^{-jk\rho_2^{EDGE}} \quad . \tag{3.109}$$

Now, the reflected-reflected-diffracted field is given by

$$U_3^{DIFF} = U_2^{REF}\, \frac{e^{-jk\rho}}{\sqrt{\rho}} \left[D(\rho, \phi-\phi', 2) + D\left(\frac{\rho_c^{DEED}\,\rho}{\rho_c^{DEED}+\rho}, \phi+\phi', 2\right)\right] \tag{3.110}$$

with $D(L, \beta, n=2)$ as before. From Figures 3.22 and 3.23, one obtains the following:

$$\rho_2^{EDGE} = Fm - Lv + x_s^{DEED} - (D_E/2)^2/(4Fm) \tag{3.111}$$

$$\rho = \left[(y-DE/2)^2 + (Lv - x_s^{DEED})^2\right]^{1/2} \tag{3.112}$$

$$\beta^- = \phi - \phi' = \pi - \sin^{-1}\left(\frac{y - D_E/2}{\rho}\right) \tag{3.113}$$

$$\alpha = \cos^{-1}\left[\frac{(\rho_i^{DEED})^2 + (\rho_c^{DEED})^2 - Fc^2}{2\rho_i^{DEED}\,\rho_c^{DEED}}\right] \tag{3.114}$$

$$\theta_i = \frac{\pi - \alpha}{2}$$

$$\gamma = \pi/2 - \theta_i \quad , \text{ and}$$

$$\phi' = \gamma + \sin^{-1}\left[\left[\frac{D_E/2}{\rho_i^{DEED}}\right]\right] .$$

Now, the diffraction angles are given by

$$\beta^+ = \phi + \phi' = \beta^- + 2\phi' \quad , \text{ or}$$

$$\beta^+ = \beta^- + \alpha + 2\sin^{-1}\left[\left[\frac{D_E/2}{\rho_i^{DEED}}\right]\right]. \tag{3.115}$$

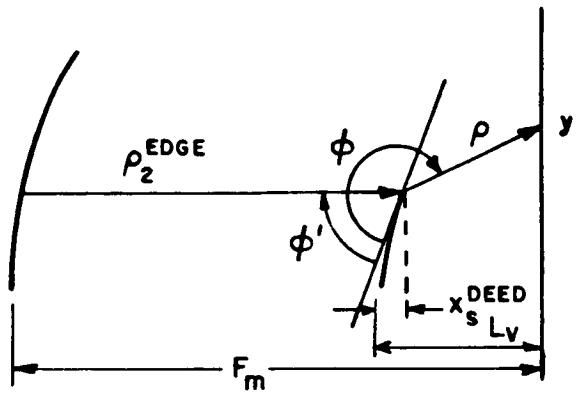

Figure 3.22 Reflected-reflected-diffracted field.

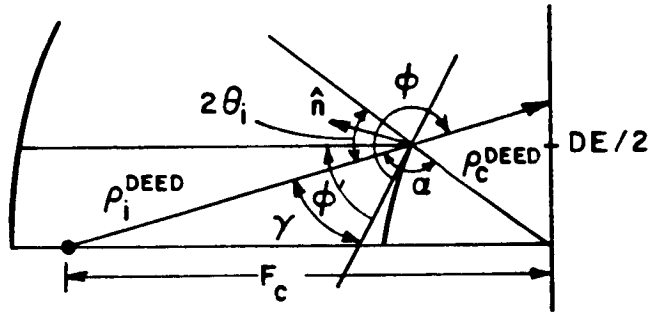

Figure 3.23 Reflected-reflected-diffracted field.

Note that U_3^{DIFF} follows from Equation (3.110). A typical plot is shown in Figure 3.24 that also includes the previously calculated terms.

As can be seen in the previous figure, the knife edge is undesirable. An elliptical rolled edge is now attached to the subreflector to eliminate the reflected-reflected-diffracted field and reduce the diffracted-reflected field at the expense of introducing a triple reflected field (see Figure 3.25). This field will be analyzed next. U_1^{REF} has been calculated previously and

$$U_2^{REF} = U_1^{REF} e^{-jk\rho_2} \tag{3.116}$$

where ρ_2 must be determined. Now the normal of the hyperbolic subreflector is given by

$$\hat{n} = \hat{x}_s - \frac{(a/b^2)y_s \hat{y}_s}{\sqrt{1+(y_s/b)^2}} \Bigg/ \sqrt{1+\frac{((a/b^2)y_s)^2}{1+(y_s/b)^2}} \tag{3.117}$$

and the center of the ellipse is specified by

$$X_E\hat{x}_s + Y_E\hat{y}_s = x_s(D_E/2)\hat{x}_s + (D_E/2)\hat{y}_s + B\hat{n} \tag{3.118}$$

(see Figure 3.26). Now the ellipse is paramaterized by

$$x = A\cos v, \text{ and} \tag{3.119}$$

$$y = B\sin v \tag{3.120}$$

for $0 < v < 2\pi$ (see Figure 3.27). Tilting the ellipse and shifting its center result in Figure 3.28, and one obtains

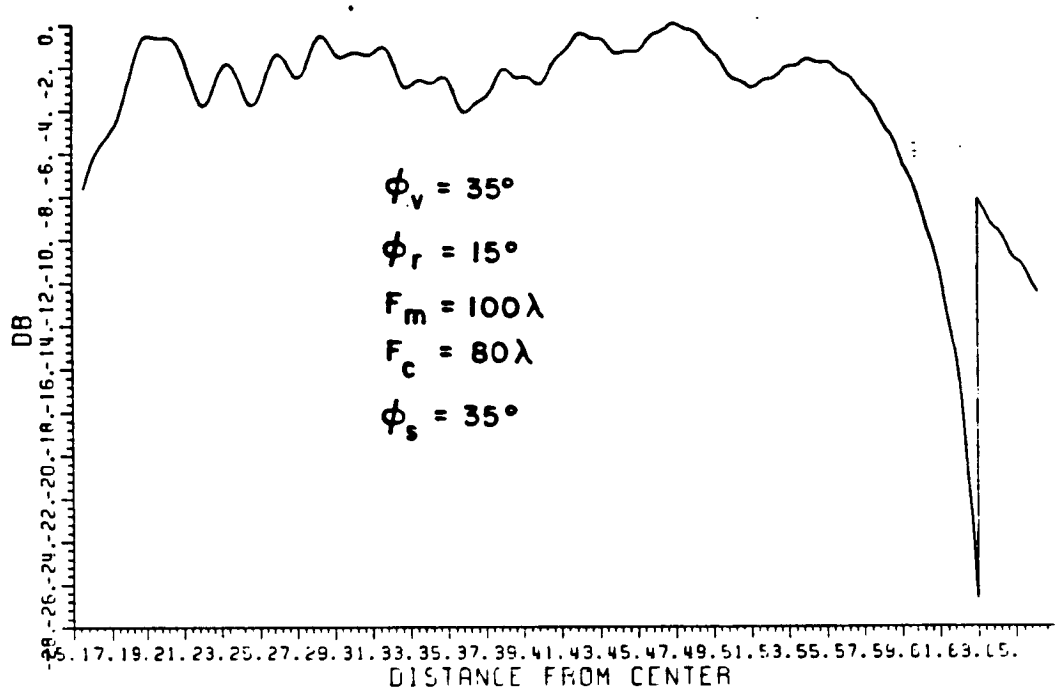

Figure 3.24 Addition of U_3^{DIFF}.

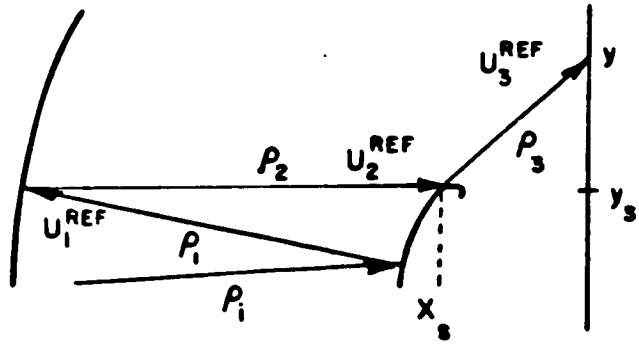

Figure 3.25 Triple reflected field.

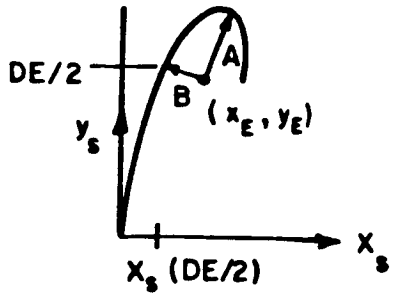

Figure 3.26 Ellipse addition.

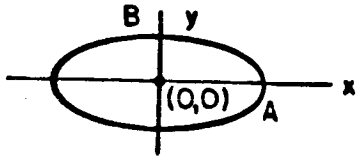

Figure 3.27 Ellipse.

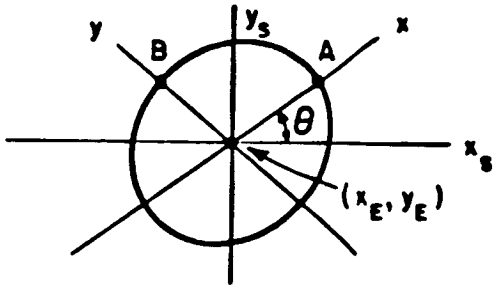

Figure 3.28 Tilted ellipse.

$$x_s = x\cos\theta - y\sin\theta + X_E, \text{ and} \tag{3.121}$$

$$y_s = x\sin\theta + y\cos\theta + Y_E \tag{3.122}$$

with

$$\theta = \sin^{-1}\left[\frac{X_E - X_s(D_E/2)}{\beta}\right] . \tag{3.123}$$

So the subreflector surface is now completely described. Then ρ_2 and U_2^{REF} are known. In Figure 3.25, U_3^{REF} is given by

$$U_3^{REF} = U_2^{REF}\sqrt{\frac{\rho_c}{\rho_c+\rho_3}}\, e^{-jk\rho_3} \tag{3.124}$$

$$\rho_3 = [(y-y_s)^2 + (Lv-x_s)^2]^{1/2} \tag{3.125}$$

$$\frac{1}{\rho_c} = \frac{2}{R_c\cos\theta_i} , \text{ and} \tag{3.126}$$

$$R_c = \frac{1}{AB}[A^2\sin^2 v + B^2\cos^2 v]^{3/2} \tag{3.127}$$

where v is given for the ellipse. To determine x_s, y_s, and θ_i, the reflection point on the subreflector is found from the iterative routine given in Appendix B. The triple reflected field is then known and a plot of this field, the reflected field, the diffracted field from the rolled main reflector, and the diffracted reflected field from the rolled subreflector is shown in Figure 3.29.

Two additional fields will now be included for completeness sake. They are the spillover incident field and the reflected field from the elliptical rolled edge on the subreflector (see Figure 3.30). Now the

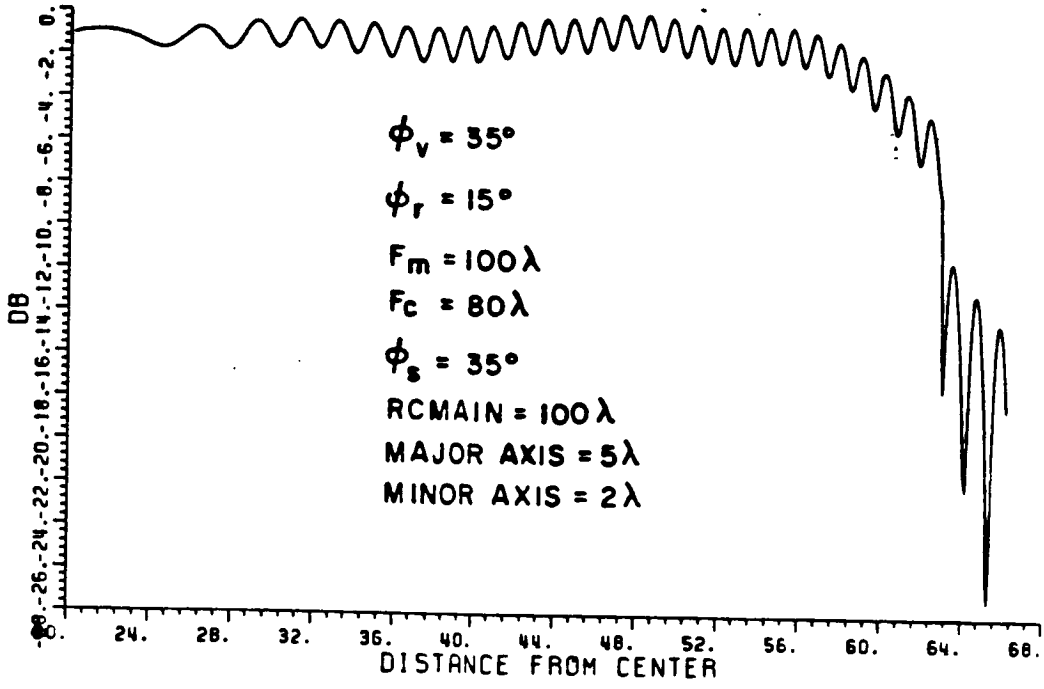

Figure 3.29 Addition of triple reflected field.

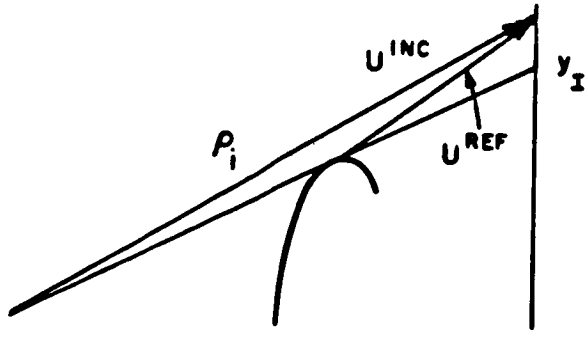

Figure 3.30 Spillover incident field and reflected field.

spillover incident field is simply given by

$$U^{INC} = c\,\frac{e^{-jk\rho_i}}{\sqrt{\rho_i}} \tag{3.128}$$

with

$$\rho_i = \sqrt{y^2+Fc^2}\ . \tag{3.129}$$

The shadow boundary designated by y_I may be determined analytically. The reflected field in Figure 3.31 is given by

$$U^{REF} = c\,\frac{e^{-jk\rho_i}}{\sqrt{\rho_i}}\sqrt{\frac{\rho_c}{\rho_c+\rho_r}}\,e^{-jk\rho_r} \tag{3.130}$$

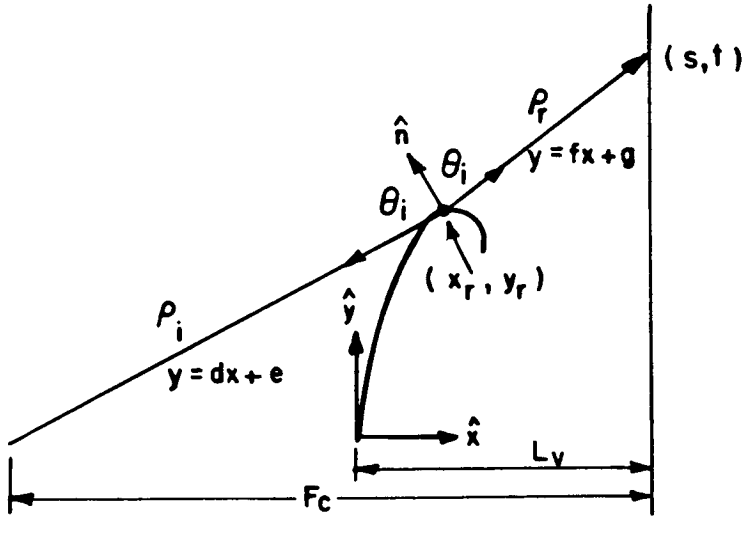

Figure 3.31 Reflected field.

with

$$\frac{1}{\rho_c} = \frac{1}{\rho_i} + \frac{2}{R_c \cos\theta_i} \tag{3.131}$$

and

$$R_c = \frac{1}{AB}\left[A^2\sin^2 v + B^2\cos^2 v\right]^{3/2} . \tag{3.132}$$

To solve for these variables, the reflection point is found using the same procedure as that in Appendix B. From Figure 3.31 the dot product is given by

$$\frac{\bar{i}\cdot\hat{n}}{|\bar{i}|} = \frac{\bar{r}\cdot\hat{n}}{|\bar{r}|} \tag{3.133}$$

with

$$\hat{n} = x_o\hat{x} + y_o\hat{y} \tag{3.134}$$

$$\bar{i} = -\hat{x} - d\hat{y} \text{ , and} \tag{3.135}$$

$$\bar{r} = \hat{x} + f\hat{y} . \tag{3.136}$$

The normal, $\hat{n}$, is given in Appendix B. Solving for f and d yields

$$f = \frac{A\sin\theta\cos v + B\cos\theta\sin v + YE - t}{A\cos v\cos\theta - B\sin v\sin\theta + YE - s} \tag{3.137}$$

and

$$d = \frac{A\sin\theta\cos v + B\cos\theta\sin v + YE}{A\cos v\cos\theta - B\sin v\sin\theta + XE + Fc\text{-}Lv} . \tag{3.138}$$

Once the reflection point is known, one finds that

$$\cos\theta_i = \frac{B\cos v\cos\theta - A\sin v\sin\theta + f[B\cos v\sin\theta + A\sin v\cos\theta]}{[B^2\cos^2 v + A^2\sin^2 v]^{1/2}[1 + f^2]^{1/2}} , \tag{3.139}$$

$$\rho_i = [y_r^2 + (Fc-Lv+x_r)^2]^{1/2} \text{ , and} \tag{3.140}$$

$$\rho_r = [(t-y_r)^2 + (Lv-x_r)^2]^{1/2} \text{ .} \tag{3.141}$$

Finally, Figure 3.32 shows the addition of these two additional field components as well as those already included in Figure 3.29.

As can be seen from this last figure, it appears that the Cassegrain system fails miserably when all the major field components are included but the last two components examined need not pose any concern. First, the feed design itself will include a taper so that the spillover and single reflected field will be reduced in magnitude. But this is trivial because these fields may be eliminated altogether by

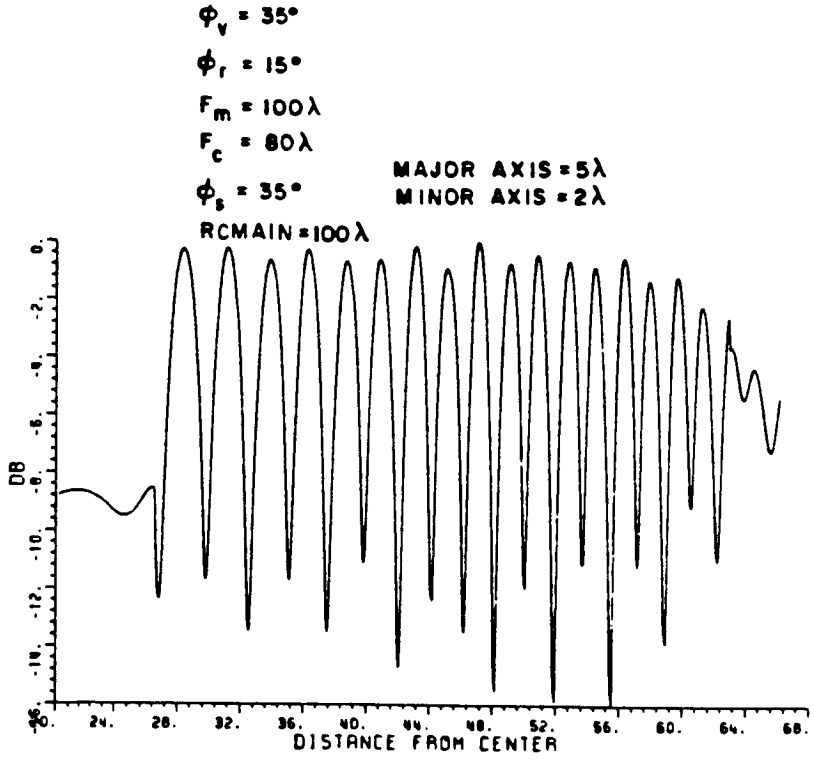

Figure 3.32 Spillover field and reflected field additions.

using a pulse radar system. In this system, the length of the pulse width determines a window through which the return from the target is examined. Because the pathlengths of the spillover field and single reflected field differ greatly from the desired target return, the pulse radar does not see these returns since they are not in that selective window. But, the triple reflected field has nearly the same pathlength as the desired reflected field so this component can't be overlooked. The same is true with the diffracted fields, but these are under relatively good control. So the triple reflected field is seen to be the major obstacle to good system performance. This field will now be examined a little more closely.

Up to this point, the target area or plane of interest has been placed at the focal length. Now it is advantageous to allow this distance to vary for added flexibility (see Figure 3.33). The four field components being examined must be modified, and this is done in Appendix C. In Figure 3.34, a representative plot shows the total field and the total field less the triple reflected field. The triple reflected field at grazing incidence is not accurately portrayed in this figure. To increase the accuracy, an additional factor is included in the triple reflected field expression as follows:

$$R_{s,h} = -\sqrt{\frac{-4}{\xi^L}}\, e^{-j\xi L^3/12}\, e^{-j\pi/4} \left[\frac{-1}{2\xi^L\sqrt{\pi}} F(X^L) + \left\{ \frac{p^*(\xi^L)}{q^*(\xi^L)} \right\} \right]. \quad (3.142)$$

But for a magnetic line source

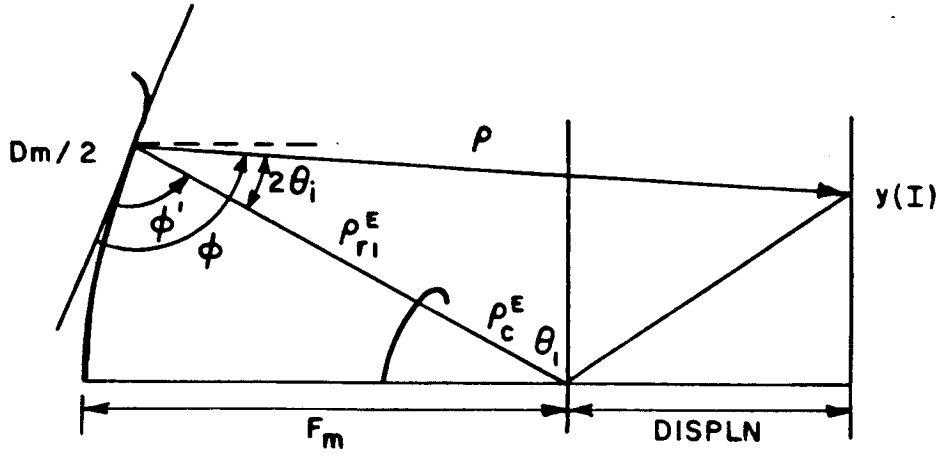

Figure 3.33 Target area at variable distance.

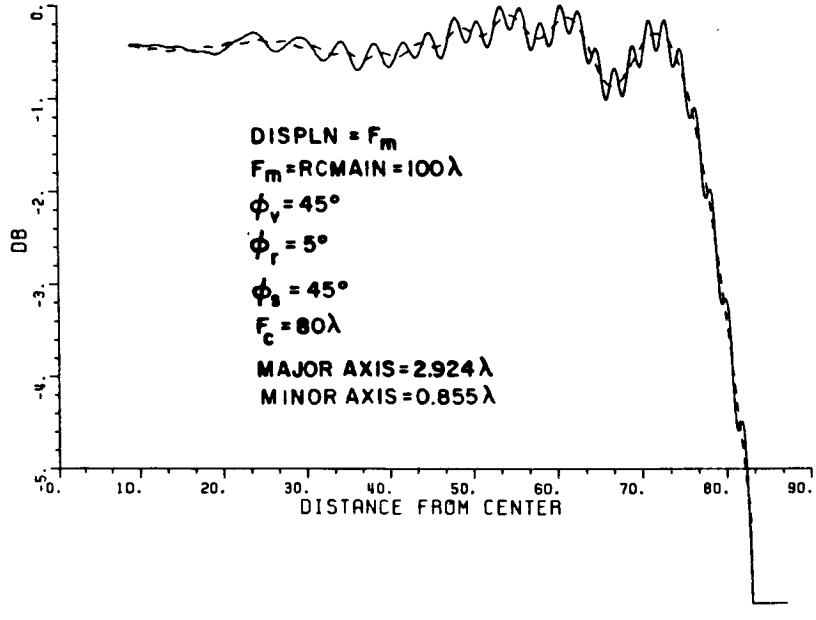

Figure 3.34 Total field (_____)and total field less triple reflected field(- - - -).

$$R_h = -\sqrt{\frac{-4}{\xi^L}}\, e^{-j\xi L^3/12}\, e^{-j\pi/4} \left[\frac{-1}{2\xi^L\sqrt{\pi}} F(X^L) + q^*(\xi^L) \right] \tag{3.143}$$

$$\xi^L = -2m(Q_R)\cos\theta_i \tag{3.144}$$

$$X^L = 2kL^L\cos^2\theta_i \tag{3.145}$$

$$L^L = \frac{s^r s'}{s^r + s'} \tag{3.146}$$

$$m(Q) = \frac{[k\rho_g(Q)]^{1/3}}{2} \tag{3.147}$$

and $\rho_g(Q)$ is the radius of curvature of the surface at the reflection point. This is already known, s^r is ρ_3, and s' is ∞ so

$$L^L = \rho_3 \,. \tag{3.148}$$

Note that $\cos\theta_i$ was calculated before and q^* is the Fock integral which is given by

$$q^*(\delta) = \frac{1}{\sqrt{\pi}} \int_{-\infty}^{\infty} \frac{v'(\tau)}{w_2'(\tau)}\, e^{-j\delta\tau} d\tau \tag{3.149}$$

with

$$2jv(\tau) = w_1(\tau) - w_2(\tau) \tag{3.150}$$

and

$$w_{1,2}(\tau) = \frac{1}{\sqrt{\pi}} \int_{\infty e^{\mp j2\pi/3}}^{\infty - j\varepsilon} e^{\tau t - t^3/3}\, dt \tag{3.151}$$

and ε arbitrarily small and positive.

Now inserting this factor yields Figure 3.35 as a representative plot. It is apparent that this increased accuracy shows that the triple reflected field is a serious problem in the Cassegrain system.

To begin to reduce this field, first consider a Gregorian subreflector system as shown in Figure 3.36. With this offset design and the subreflector placed low, the triple reflected field is virtually eliminated. But this configuration introduces a doubly reflected field that was not present before and must be considered. First, the normal reflected field is found (see Figure 3.37). The expression for the first reflected field is

$$U_1^{REF} = \frac{e^{-jk\rho_i}}{\sqrt{\rho_i}} \sqrt{\frac{\rho_c}{\rho_1}}\, e^{-jk(\rho_c+\rho_1)}\, e^{j\pi/2} . \tag{3.152}$$

The caustic distance ρ_c may be calculated from geometrical considerations. So, one obtains that

$$\rho_c = [(Lv+x_s)^2+y_s^2]^{1/2} \tag{3.153}$$

$$\rho_i = [(Fc+Lv+x_s)^2+y_s^2]^{1/2}, \text{ and} \tag{3.154}$$

$$\rho_1 = [(y_m-y_s)^2+(Fm+Lv+x_s - \frac{ym^2}{4Fm})]^{1/2}. \tag{3.155}$$

Then U_2^{REF} is given by

$$U_2^{REF} = U_1^{REF}\, e^{-jk\rho_2} \tag{3.156}$$

with

$$\rho_2 = DISPLN + Fm+Lv\ \frac{-ym^2}{4Fm} \tag{3.157}$$

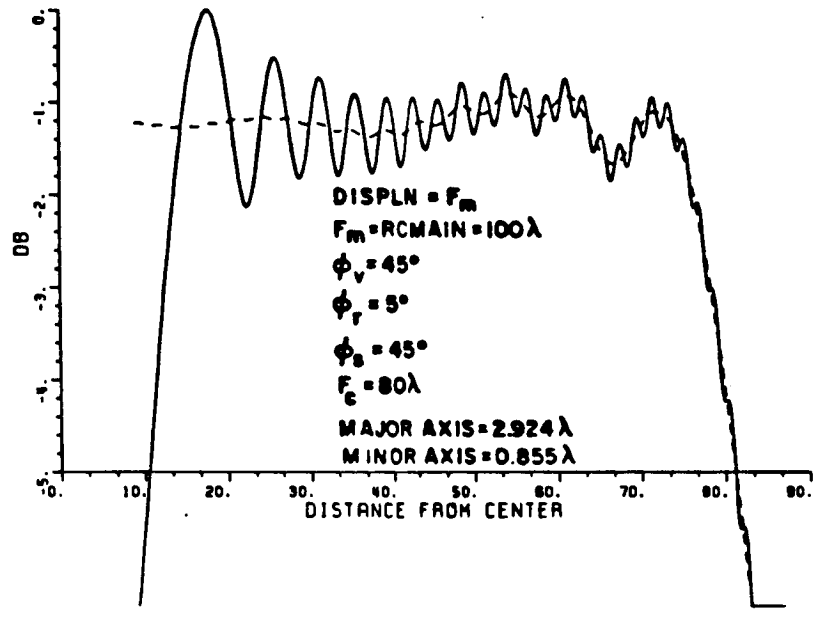

Figure 3.35 Total field (_____) and total field less triple reflected field (_ _ _ _).

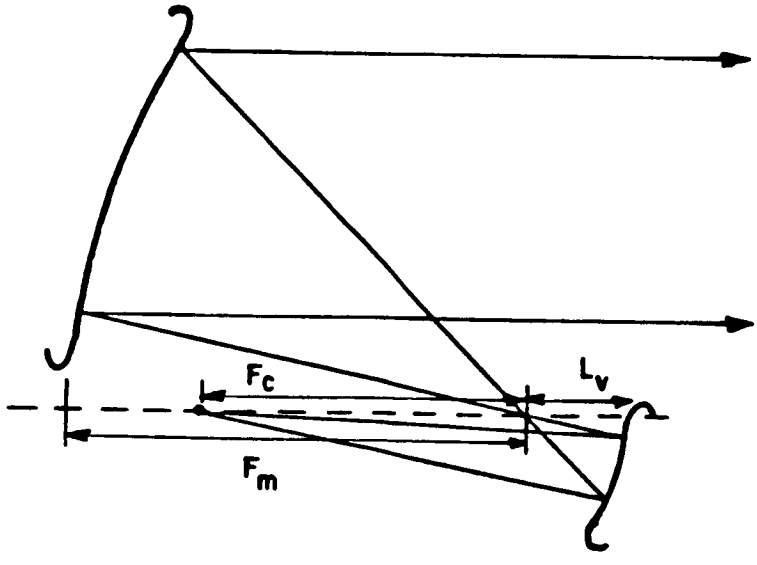

Figure 3.36 Gregorian subreflector system.

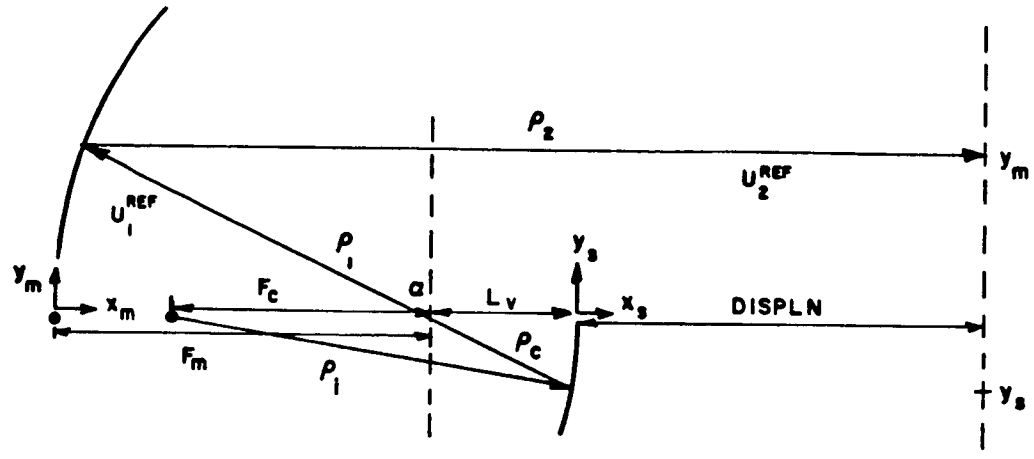

Figure 3.37 Reflected field.

since the caustic distance in this case is infinity. Finally, y_s may be expressed in terms of y_m by noting that

$$\text{TAN}\alpha = \frac{\rho_2 - \text{DISPLN} - Lv}{y_m} = \frac{Lv + x_s}{-y_s}$$

which yields

$$y_s = \frac{-Lv + a - a\sqrt{1 + \frac{Lv^2 - 2aLv}{(bc)^2}}}{c - \frac{1}{c}\left(\frac{a}{b}\right)^2} \tag{3.158}$$

with

$$c = \frac{-Lv - x_s}{y_s} \, . \tag{3.159}$$

Now consider the doubly reflected field shown in Figure 3.38. Again, attach an elliptical rolled edge to the subreflector. The analysis proceeds as with the triple reflected field. The angle θ needs to be examined more closely in this situation. If the ellipse is attached below or at the main axis (Figure 3.39), then

$$\theta = \theta_1 = \sin^{-1}\left[\frac{XE - x_s(\text{ATTACH POINT})}{B}\right] \tag{3.160}$$

but if it is attached above the main axis (Figure 3.40), then

$$\theta = \pi - \theta_1 \ . \tag{3.161}$$

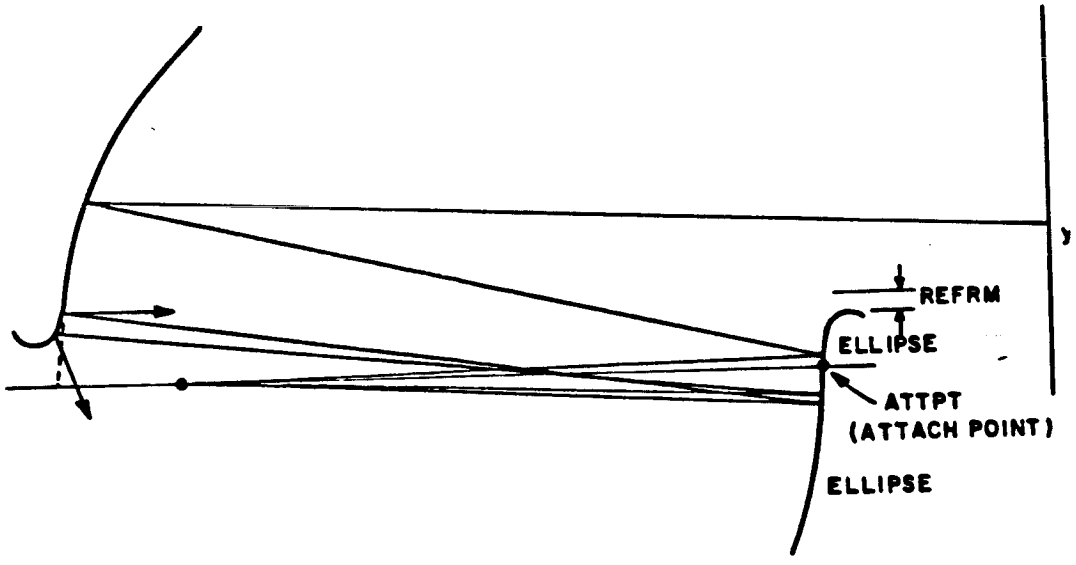

Figure 3.38 Doubly reflected field.

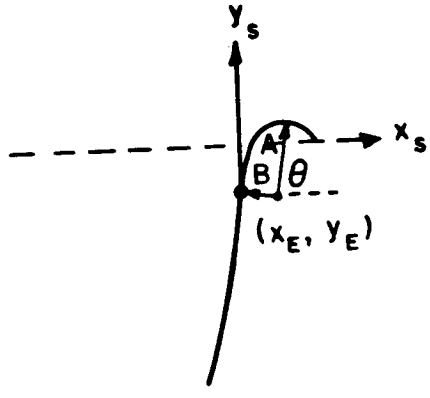

Figure 3.39 Attachment of ellipse.

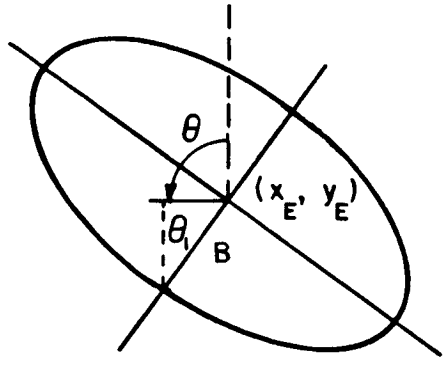

Figure 3.40 Attachment of ellipse.

For a given point in the plane of interest, two reflection points need to be found simultaneously as illustrated in Figure 3.41. Proceeding as in Appendix B, the first dot product is

$$\frac{\hat{n}_1 \cdot \bar{r}_1}{|\bar{r}_1|} = \frac{\hat{n}_1 \cdot \bar{i}_1}{|\bar{i}_1|} \tag{3.162}$$

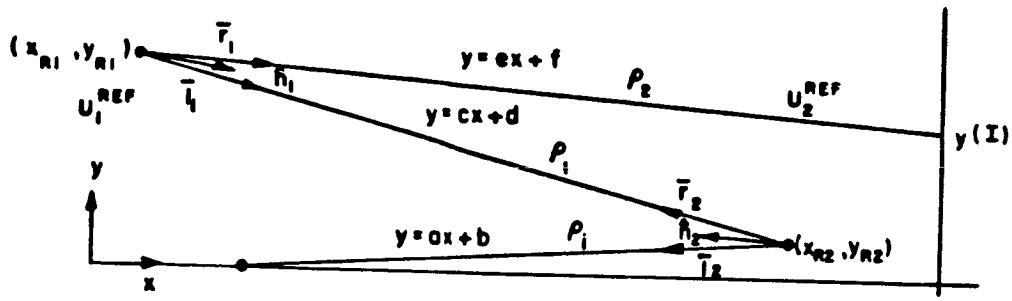

Figure 3.41 Doubly reflected field.

with

$$\hat{n}_1 = \frac{\hat{x} - \frac{y_{RI}\,\hat{y}}{2Fm}}{\left(1 + \frac{y_{RI}^2}{4Fm^2}\right)^{1/2}}, \tag{3.163}$$

$$\bar{r}_1 = \hat{x} + e\hat{y}, \quad \text{and} \tag{3.164}$$

$$T_1 = \hat{x} + c\hat{y}. \tag{3.165}$$

Solving for e and c yields that

$$e = \frac{y_{R1} - y_{(I)}}{\left[\frac{y_{R1}^2}{4Fm} - (Fm+Lv+DISPLN)\right]} \tag{3.166}$$

and

$$c = \frac{y_{R1} - (A\sin\theta\cos v + B\cos\theta\sin v = Y_E}{\left[\frac{y_{R1}^2}{4Fm} - (Fm+Lv+A\cos\theta\cos v - B\sin\theta\sin v + X_E\right]}. \tag{3.167}$$

The second dot product is

$$\frac{\hat{n}_2\cdot\bar{r}_2}{|\bar{r}_2|} = \frac{\hat{n}_2\cdot\bar{r}_1}{|\bar{r}_1|} \tag{3.168}$$

with

$$\hat{n}_2 = \frac{B\cos v\cos\theta - A\sin v\sin\theta}{[B^2\cos^2 v + A^2\sin^2 v]^{1/2}}\hat{x} + \frac{B\cos v\sin\theta + A\sin v\cos\theta}{[B^2\cos^2 v + A^2\sin^2 v]^{1/2}}\hat{y} \tag{3.169}$$

$$\bar{r}_2 = -\hat{x} - c\hat{y}\ , \text{ and} \tag{3.170}$$

$$\bar{I}_2 = -\hat{x} - a\hat{y}. \tag{3.171}$$

Thus, one finds that

$$a = \frac{A\cos v\sin\theta + B\sin v\cos\theta + Y_E}{Lv+Fc+A\cos v\cos\theta - B\sin v\sin\theta + X_E}. \tag{3.172}$$

Now the simultaneous solution to the two dot products in Equations (3.162) and (3.168) is needed to find the reflection point. This is done

iteratively using bisection methods over the v and y_{R1} intervals until these values are found within some specified error. Then v and y_{R1} give the two reflection points as

$$x_{R1} = y_{R1}^2/(4Fm) \tag{3.173}$$

$$x_{R2} = A\cos v\cos\theta - B\sin v\sin\theta + X_E, \text{ and} \tag{3.174}$$

$$y_{R2} = A\cos v\sin\theta + B\sin v\cos\theta + Y_E \, . \tag{3.175}$$

Then

$$U_1^{REF} = \frac{e^{-jk\rho i}}{\sqrt{\rho_i}} \sqrt{\frac{\rho_{cs}}{\rho_{cs}+\rho_1}}\, e^{-jk\rho_1} \tag{3.176}$$

where

$$\rho_i = [(Fc+Lv+x_{R2})^2 + y_{R2}^2]^{1/2} \tag{3.177}$$

$$\rho_1 = [(Fc+Lv+x_{R2}-x_{R1})^2 + y_{R1} - y_{R2})^2]^{1/2} \tag{3.178}$$

$$\frac{1}{\rho_{cs}} = \frac{1}{\rho_i} + \frac{2}{R_c\cos\theta_i} \tag{3.179}$$

$$R_c = \frac{1}{AB}\,(A^2\sin^2 v + B^2\cos^2 v)^{3/2} \tag{3.180}$$

and $\cos\theta_i$ may be found from the second dot product. Next the second reflected field is

$$U_2^{REF} = U_1^{REF} \sqrt{\frac{\rho_{cm}}{\rho_{cm} + \rho_2}}\, e^{-jk\rho_2} \tag{3.181}$$

where

$$\frac{1}{\rho_{cm}} = \frac{1}{\rho_{im}} + \frac{2}{R_c\cos(\pi-\theta_i)} \tag{3.182}$$

$$\rho_{im} = \rho_1 + \rho_{cs} \tag{3.183}$$

$$R_c = 2Fm \left[1 + \left(\frac{y_{R1}^2}{4Fm^2}\right) \right]^{3/2} \tag{3.184}$$

$$\cos(\pi-\theta_i) = -\cos\theta_i \tag{3.185}$$

and $\cos\theta_i$ may be found from the first dot product. Finally the caustic distance is

$$\rho_2 = [(Fm+Lv+DISPLN-y_{R1}^2/(4Fm))^2 + (y_{R1}-y(I))^2]^{1/2} \tag{3.186}$$

and U_2^{REF} is known. Typical plots for the sum of this doubly reflected field and the normally reflected field are shown in Figure 3.42. It is apparent that attaching the edge higher on the subreflector reduces the field ripple but intuitively this will increase the triple reflected field effect which was the original problem. In any case, the effect of the doubly reflected field with the Gregorian system is unacceptable. But this system does provide insight into reducing the triple reflected field by using an offset reflector type of design. So, next let us try utilizing the offset design with the classical Cassegrain system.

Initially, this type of design poses problems because edges will be attached to the top and bottom of both reflectors resulting in several diffracted fields at the junctions. Although the triple reflected field

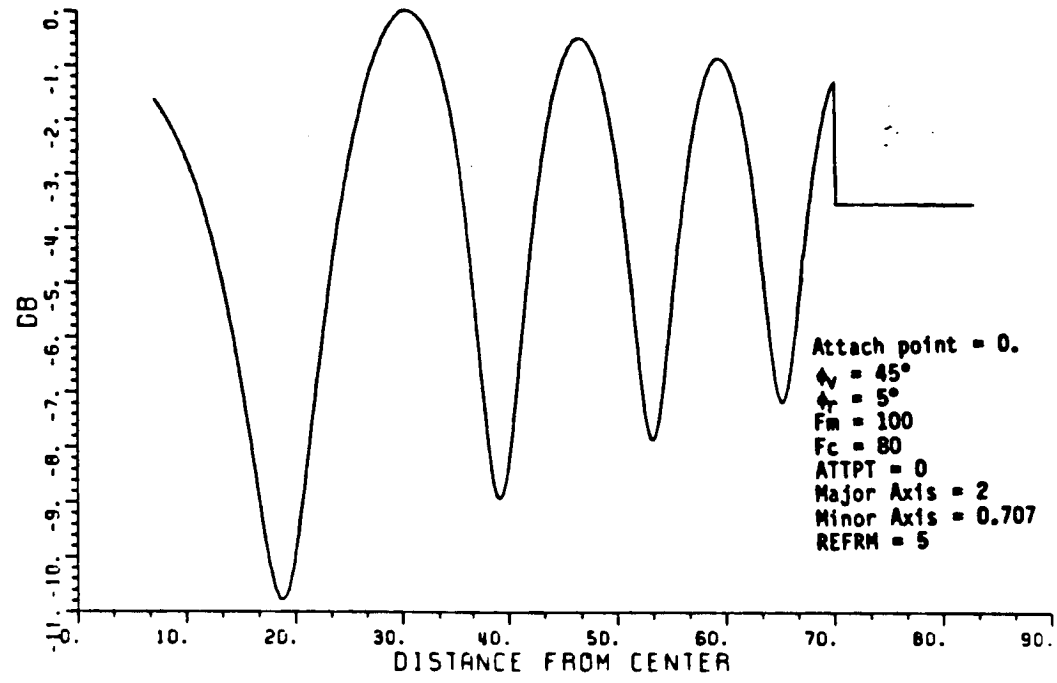

(a) Attach point = 0.

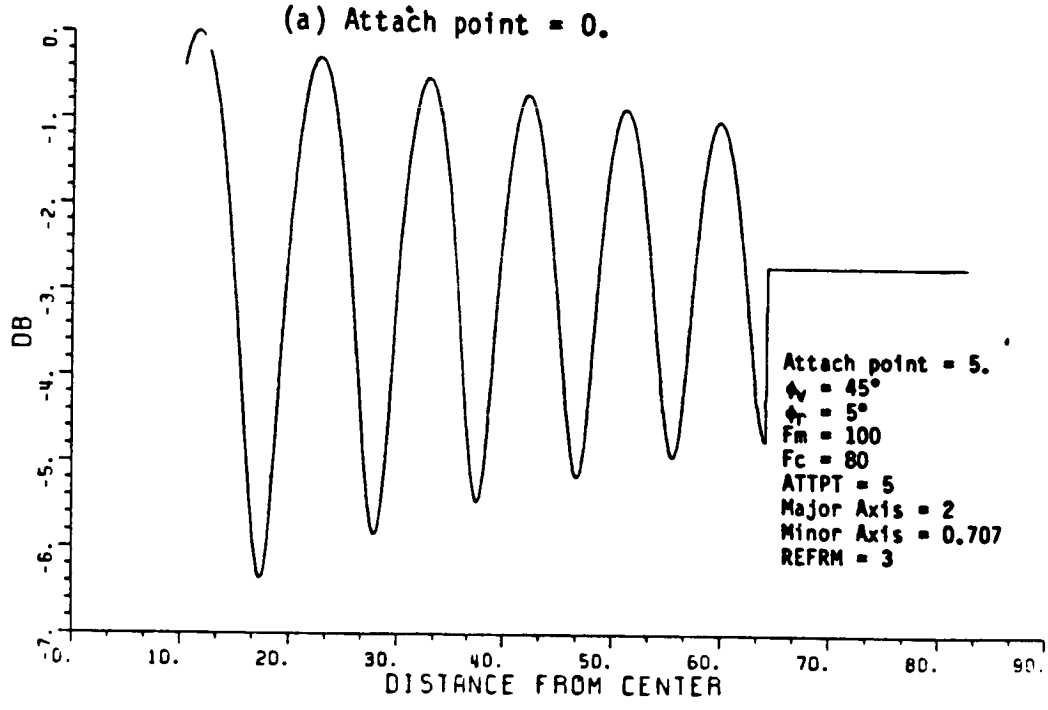

(b) Attach point = 5.

Figure 3.42 Sum of two reflected fields.

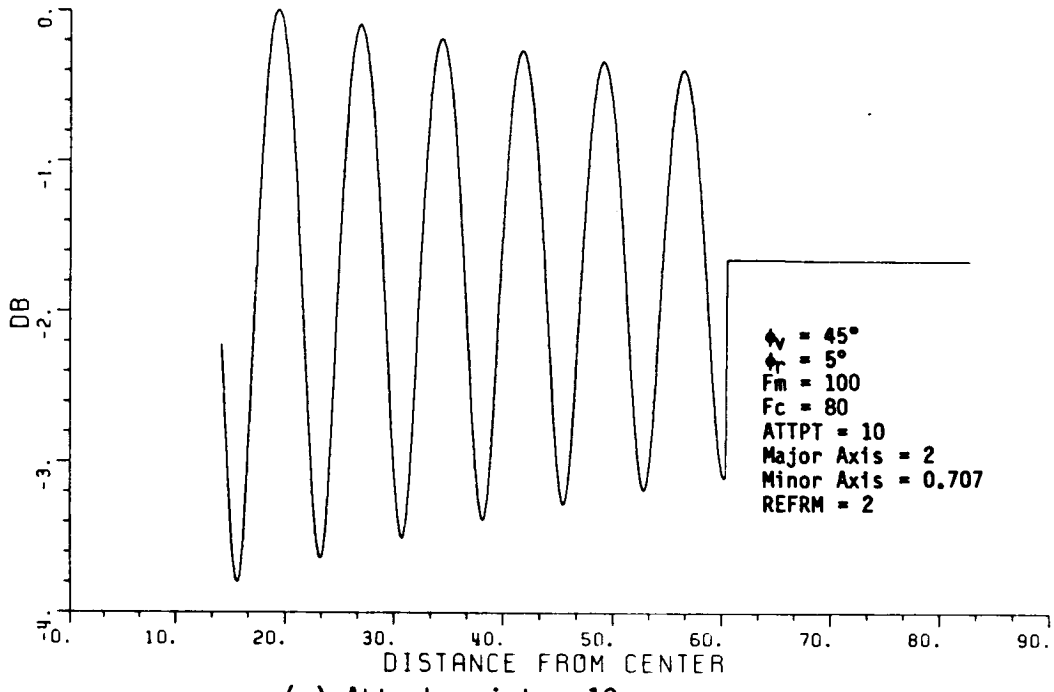

(c) Attach point = 10.

Figure 3.42 (Continued).

may be reduced, the additional diffracted fields will degrade overall system performance. If these diffracted fields could be reduced and the triple reflected field minimized, an acceptable system would be the result. Through the blending of the edges considered in the next chapter, diffracted fields are reduced sufficiently to allow the offset Cassegrain system to work effectively.

CHAPTER IV

THE BLENDED SURFACE

The last chapter brought to view problems encountered in the Cassegrain system. Now a viable solution is presented to solve these problems and obtain satisfactory system performance.

The subreflector edges are the first that will be blended as shown in Figure 4.1. By a blended surface it is meant that the curved surfaces are blended between an ellipse and the original surface to which these surfaces are attached. As before the hyperbola is described by

$$x = a\,[\sqrt{1+(y/b)^2} - 1] \tag{4.1}$$

with

$$e = \frac{\sin(\phi_v+\phi_r)/2}{\sin(\phi_v-\phi_r)/2} \tag{4.2}$$

$$a = \frac{Fc}{2e} \text{ , and} \tag{4.3}$$

$$b = a\sqrt{e^2-1} \text{ .} \tag{4.4}$$

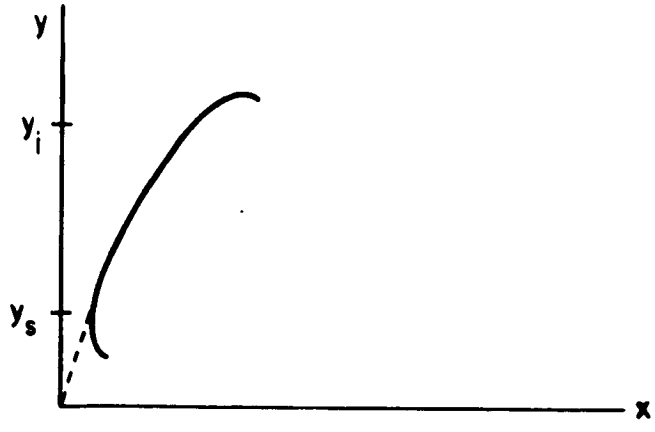

Figure 4.1 Subreflector with blended surfaces.

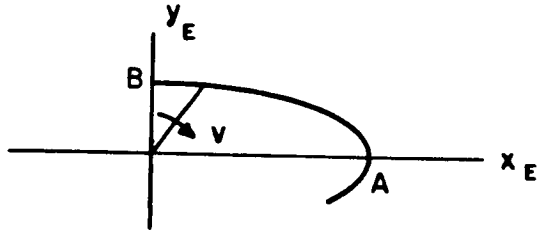

Figure 4.2 Ellipse for upper edge.

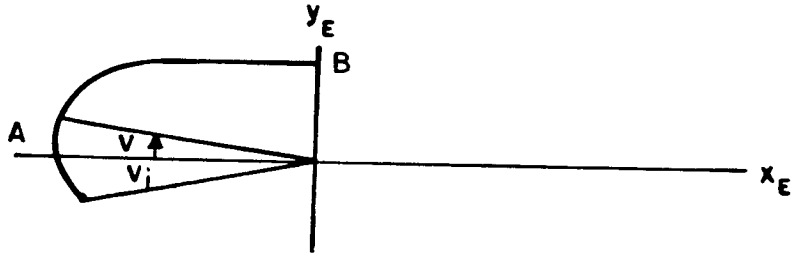

Figure 4.3 Ellipse for bottom edge.

The blended upper surface is given in general by

$$f = f_{HYPERBOLA}P + f_{ELLIPSE}(1-P) \tag{4.5}$$

$$P(v) = \frac{1+\cos(\pi v/v_f)}{2} \quad , \quad 0 \leq P \leq 1, \text{ and} \tag{4.6}$$

$$v = v_f \frac{Y_p - Y_i}{Y_f - Y_i} \quad , \quad 0 \leq v \leq v_f \quad . \tag{4.7}$$

Note that the parameter through which the blended edge is generated is Y_p with Y_i, Y_f and v_f to be specified. Proceeding as in the previous chapter, the ellipse to be blended is given parametrically as

$$X = A\sin v\cos\theta - B\cos v\sin\theta + X_{ELL} \tag{4.8}$$

$$Y = A\sin v\sin\theta + B\cos v\cos\theta + Y_{ELL} \tag{4.9}$$

with

$$\theta = \sin^{-1}\left(\frac{X_{ELL} - X(v=0)}{B}\right) . \tag{4.10}$$

X_{ELL} and Y_{ELL} are calculated as in the previous chapter and increasing v is shown in Figure 4.2. Now Equation (4.5) yields

$$X(Y_p) = X(Y_p)_{HYPERBOLA}P(Y_p) + X(Y_p)_{ELLIPSE}[1-P(Y_p)] \tag{4.11}$$

$$Y(Y_p) = Y_pP(Y_p) + Y(Y_p)_{ELLIPSE}[1-P(Y_p)] \tag{4.12}$$

with the blending function P given by Equation (4.6) and v given by Equation (4.7).

The bottom blended surface is generated in a similar manner. In Figure 4.3, v now varies from a specified v_i to $\pi/2$. The blending function is now

$$P(v) = \frac{1+\cos\pi\left(\frac{v-v_i}{\pi/2-v_i}\right)}{2} \tag{4.13}$$

with

$$v = \left(\frac{\pi}{2} - v_i\right)\left(\frac{Y_p-Y_i}{Y_f-Y_i}\right) + v_i \ , \qquad v_i < v < \pi/2 \tag{4.14}$$

and Y_i and Y_f are to be specified. The ellipse to be blended is given by

$$X = -A\cos v\cos\theta - B\sin v\sin\theta + X_{ELL} \tag{4.15}$$

$$Y = -A\cos v\sin\theta + B\sin v\cos\theta + Y_{ELL} \tag{4.16}$$

with

$$\theta = \sin^{-1}\left(\frac{X_{ELL} - X(v=\pi/2)}{B}\right) \ . \tag{4.17}$$

Again X_{ELL} and Y_{ELL} are calculated as in the previous chapter. The equations generating this blended surface are then given by

$$X(Y_p) = X(Y_p)_{HYPERBOLA}[1-P(Y_p)] + X(Y_p)_{ELLIPSE}P(Y_p) \tag{4.18}$$

and

$$Y(Y_p) = Y_p[1-P(Y_p)] + Y(Y_p)_{ELLIPSE}P(Y_p) \ . \tag{4.19}$$

Of course between the two blended surfaces the normal subreflector is described by Equation (4.1).

Now the centers of the ellipses will be given. The normal to the hyperbola is given by Equation (3.117) and evaluated at Y_i for the top

edge. Then, one finds that

$$X_{ELL}\,\hat{X} + Y_{ELL}\,\hat{Y} = X(Y_i)\hat{X} + Y_i\hat{Y} + B\hat{n} \qquad (4.20)$$

and for the bottom edge with $\hat{n}$ evaluated at Y_f is specified by

$$X_{ELL}\,\hat{X} + Y_{ELL}\,\hat{Y} = X(Y_f)\hat{X} + Y_f\hat{y} + B\hat{n} \quad . \qquad (4.21)$$

Now the offset subreflector with two blended surfaces is completely specified by Equations (4.18), (4.19), (4.11), (4.12), and (4.1). The parameters that can be varied are Y_i and Y_f for the top and bottom, v_i, v_f, and the major and minor axes of both ellipses.

The design of the surfaces may proceed and a few general rules are given here to simplify the procedure. It is convenient to use the same values for the axes of both ellipses and fix v_i at $-\pi/2$ and v_f at π. This allows the knife surfaces to be completely removed from view of the source. The excessive hidden surfaces on the subreflector, as well as the main reflector later on, are removed by limiting the range over which the curve is generated. This is in general better than respecifying v_i and v_f which would lead to surfaces whose shape is changed each time. In general, the larger the surfaces, the flatter the field will be. But small surfaces are also desirable to taper this field to reduce the effect of the triple reflected field. So a tradeoff exists in the size of the surfaces . This size is determined by the major axis of the ellipse as well as the length of the blended hyperbola section (which is determined by Y_i and Y_f). Now the minimum radius of curvature of the edge must be kept greater than a quarter wavelength at

the lowest frequency of operation. Once the general size of the surfaces is decided, the radius of curvature is determined by the minor axis dimension of the ellipse. One final constraint is the relationship between the major axis length and the length of the hyperbola section. By looking at the slope or first derivative of this curve, a gradual transition is best obtained for a hyperbola section length that is approximately four times the major axis length. Again, this constraint is true at v_i equal to $-\pi/2$ and v_f equal to π. So when designing the surfaces , the size for acceptable performance is the overriding consideration. Besides the design of the surfaces, the size of the subreflector itself is another variable. It must be large enough to illuminate satisfactorily the main reflector yet kept as small as possible so that interactions between the two reflectors may be minimized.

The field produced by the subreflector will now be examined. Using UTD and physical optics, the field along a parabolic contour is calculated. Using a magnetic line source (Figure 4.4), one finds that the reflected field is given by

$$U^{REF} = \frac{e^{-jk\rho_i}}{\sqrt{\rho_i}} \sqrt{\frac{\rho_c}{\rho_c+\rho_r}}\, e^{-jk\rho_r} \quad . \tag{4.22}$$

For the region between Y_i and Y_f, U^{REF} has been calculated before with

$$\rho_c = [(Lv-x)^2 + y^2]^{1/2} \tag{4.23}$$

$$\rho_i = [Y^2 + (Fc-Lv+x)^2]^{1/2} \tag{4.24}$$

$$\rho_r = [(YP-Y)^2 + (Fm-Lv+x-YP^2/(4Fm))^2]^{1/2} \tag{4.25}$$

C-2

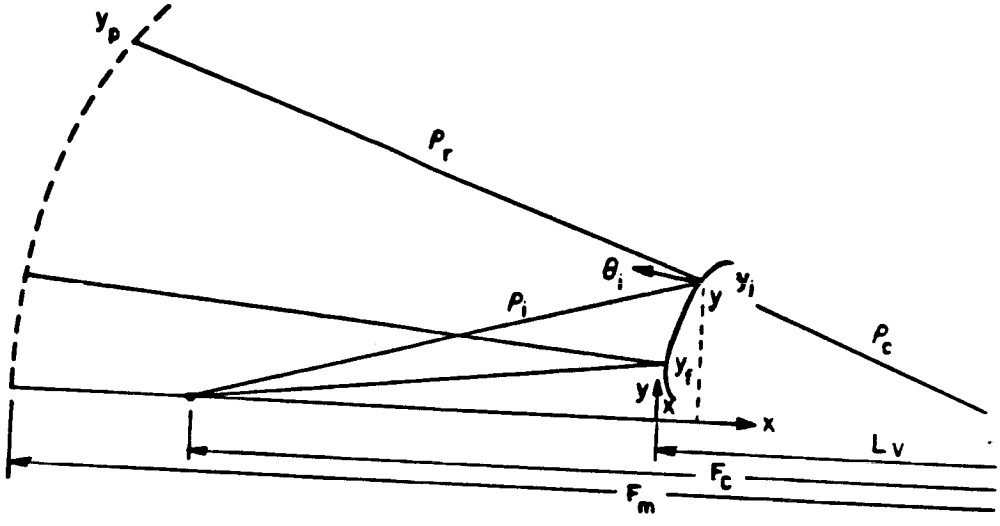

Figure 4.4 Field along a parabolic contour.

Also

$$YP = 2Fm\left[\frac{-1}{c} + \sqrt{\frac{1}{c^2}+1}\right] \tag{4.26}$$

with

$$c = \frac{Y}{Lv-x} \quad . \tag{4.27}$$

Now the reflected field from the edges is more complicated. The caustic distance must be recalculated using

$$1/\rho_c = 1/\rho_i + 2/(R_c \cos\theta_i) \quad . \tag{4.28}$$

For a given point, ρ_i is known from Equation (4.24). Now

$$R_c = |1/CURV| \tag{4.29}$$

where

$$CURV = \frac{y'x'' - x'y''}{[(y')^2+(x')^2]^{3/2}} \tag{4.30}$$

and the derivatives need to be taken with respect to the parameter Y_p. The derivative results for the bottom edge are as follows:

$$X' = X'_{HYP}(1-P) + X_{HYP}(-P') + X'_{ELL}\,P + X_{ELL}\,P' \tag{4.31}$$

$$X'_{HYP}(Y_P) = \frac{ay}{b^2}(1+(y/b)^2)^{-1/2} \tag{4.32}$$

$$P'(Yp) = -\frac{1}{2}\sin[\pi\frac{v-v_i}{\pi/2-v_i}](\frac{\pi}{Y_f-Y_i}) \tag{4.33}$$

$$X'_{ELL}(Y_p) = [A\sin v\cos\theta - B\cos v\sin\theta][\frac{\pi/2-vi}{Y_{f-Y_i}}] \tag{4.34}$$

$$X'' = X''_{HYP}(1-P) + 2X'_{HYP}(-P') + X_{HYP}(-P'') + X''_{ELL}P + 2X'_{ELL}P' + X_{ELL}P'' \quad (4.35)$$

$$X''_{HYP}(Y_P) = \frac{a/b^2}{[1+(Y/b)^2]^{3/2}} \quad (4.36)$$

$$P''(YP) = -\frac{1}{2}\cos\left[\frac{\pi}{\pi/2-vi}\right]\left[\frac{\pi}{Y_f-Y_i}\right]^2 \quad (4.37)$$

$$X''_{ELL}(Y_p) = \left[A\cos v\cos\theta + B\sin v\sin\theta\right]\left[\frac{\pi/2-v_i}{Y_f-Y_i}\right]^2 \quad (4.38)$$

$$Y' = (1-P) + Y_p(-P') + Y'_{ELL}P + Y_{ELL}P' \quad (4.39)$$

$$Y'_{ELL}(Y_p) = (A\cos v\sin\theta + B\cos v\cos\theta)\left[\frac{\pi/2-v_i}{Y_f-Y_i}\right] \quad (4.40)$$

$$Y'' = -2P'' + Y_p(-P'') + Y''_{ELL}P + 2Y'_{ELL}P' + Y_{ELL}P'' \text{ , and} \quad (4.41)$$

$$Y''_{ELL}(Y_p) = (A\cos v\sin\theta - B\sin v\cos\theta)\left[\frac{\pi/2-v_i}{Y_f-Y_i}\right]^2 . \quad (4.42)$$

The derivative results for the top edge are as follows:

$$X' = X'_{HYP}P + X_{HYP}P' + X'_{ELL}(1-P) + X_{ELL}(-P') \quad (4.43)$$

$$P'(Y_p) = -\frac{1}{2}\,SIN\left[\frac{\pi V}{v_f}\right]\left(\frac{\pi}{Y_f-Y_i}\right) \quad (4.44)$$

$$X'_{ELL}(Y_p) = (A\cos v\cos\theta + B\sin v\sin\theta)\left(\frac{v_f}{Y_f-Y_i}\right) \quad (4.45)$$

$$X'' = X''_{HYP}P + 2X'_{HYP}P' + X_{HYP}P'' + X''_{ELL}(1-P) + 2X'_{ELL}(-P') + X_{ELL}(-P'') \tag{4.46}$$

$$P''(Y_p) = -\frac{1}{2}\cos\left[\frac{\pi v}{v_f}\right]\left[\frac{\pi}{Y_f - Y_i}\right]^2 \tag{4.47}$$

$$X''_{ELL}(Y_p) = (-A\sin v\cos\theta + B\cos v\sin\theta)\left[\frac{v_f}{Y_f - Y_i}\right]^2 \tag{4.48}$$

$$Y' = P + Y_pP'' + Y'_{ELL}(1-P) + Y_{ELL}(-P') \tag{4.49}$$

$$Y'_{ELL}(Y_p) = (A\cos v\sin\theta - B\sin v\cos\theta)\left[\frac{v_f}{Y_f - Y_i}\right] \tag{4.50}$$

$$Y'' = 2P' + Y_pP'' + Y''_{ELL}(1-P) + 2Y'_{ELL}(-P') + Y_{ELL}(-P''), \text{ and} \tag{4.51}$$

$$Y''_{ELL}(Y_p) = (-A\sin v\cos\theta + B\cos v\cos\theta)\left[\frac{v_f}{Y_f - Y_i}\right]^2 . \tag{4.52}$$

These derivatives provide the information necessary to compute the radius of curvature. The normal is computed next so that $\cos\theta_i$ may be found. For both edges the slope is given by

$$m = Y'/X' \tag{4.53}$$

and the normal has slope -1/m. For both edges the normal is given by

$$\hat{n} = X_n\hat{x} + Y_n\hat{y} = \frac{-\hat{x} + (1/m)\hat{y}}{[1+1/m^2]^{1/2}} . \tag{4.54}$$

Now forming the dot product with the incident vector, one finds that

$$\hat{\rho}_i = \frac{-(Fc-Lv+x)\hat{x}-Y\hat{y}}{[(Fc-Lv+X)^2+Y^2]^{1/2}} \tag{4.55}$$

which yields

$$\cos\theta_i = \frac{-X_n(Fc-Lv+X)-Y_nY}{[(Fc-Lv+X)^2+Y^2]^{1/2}} \quad . \tag{4.56}$$

Note that the caustic distance ρ_c is known. Equating the angle of incidence with the angle of reflection allows the point YP on the parabola to be found. So one obtains that

$$\hat{\rho}_r = \frac{-(Fm-Lv+X-YP^2/(4Fm))\hat{x}+(YP-Y)\hat{y}}{[(Fm-Lv+X-YP^2/(4Fm))^2+(YP-Y)^2]^{1/2}} \tag{4.57}$$

and

$$\cos\theta_i = \frac{-X_n(Fm-Lv+X-(YP)^2/(4Fm))+Y_n(YP-Y)}{[(Fm-Lv+X-YP^2/(4Fm))^2+(YP-Y)^2]^{1/2}} \quad . \tag{4.58}$$

Using an iterative bisection method, YP may be found numerically. Then the reflected field from the blended surfaces along a parabolic contour is known. Numerically, it is convenient to pick points on the subreflector and ray trace to the corresponding point on the parabolic curve.

The subreflector is now analyzed using the physics optics approximation and the results compared with the reflected field given by geometrical optics. Again using a magnetic line source, the current on the lit side of the subreflector is given by

$$\bar{J}s = 2\hat{n} \times \bar{H}^i \quad . \tag{4.59}$$

In Figure 4.5, $\bar{H}^i$ is $\hat{z}$-directed and the normal $\hat{n}$ lies in the x,y-plane. The two dimensional radiation integral is used to compute the subreflector scattered field which is given by

$$Hz = \sqrt{\frac{k}{8\pi}}\, e^{j\pi/4} \int \hat{z} \cdot (\hat{t} \times \hat{\rho}) J_t \frac{e^{-jk\rho}}{\sqrt{\rho}} (\hat{\rho}_i \cdot \hat{n}) d\ell \tag{4.60}$$

where

$$\bar{H}^i = H_z^i \hat{Z} = \frac{e^{-jk\rho_i}}{\sqrt{\rho_i}} \hat{z} \tag{4.61}$$

and

$$\bar{J}_s = J_t \hat{t} = 2H_z^i \hat{t} \quad . \tag{4.62}$$

The slope (m) is given by Equation (4.53) and the unit tangent by

$$\hat{t} = t_x \hat{x} + t_y \hat{y} = \frac{\hat{x}+m\hat{y}}{\sqrt{1+m^2}} \qquad \text{for m positive} \tag{4.63}$$

$$\hat{t} = t_x \hat{x} + t_y \hat{y} = \frac{-\hat{x}-m\hat{y}}{\sqrt{1+m^2}} \qquad \text{for m negative or m positive on lower edge.} \tag{4.64}$$

Also, one finds that

$$\rho_i = [Y^2 + (Fc-Lv+X)^2]^{1/2} \tag{4.65}$$

and J_t is then known. Now, one obtains the following:

$$\rho = [(Fm-Lv+X-(YPAR)^2/(4Fm))^2 + (YPAR-Y)^2]^{1/2} \tag{4.66}$$

$$\hat{\rho} = \rho_x \hat{x} + \rho_y \hat{y} = \frac{-(Fm-Lv+X-(YPAR)^2/(4Fm))\hat{x} + (YPAR-Y)\hat{y}}{\rho} \tag{4.67}$$

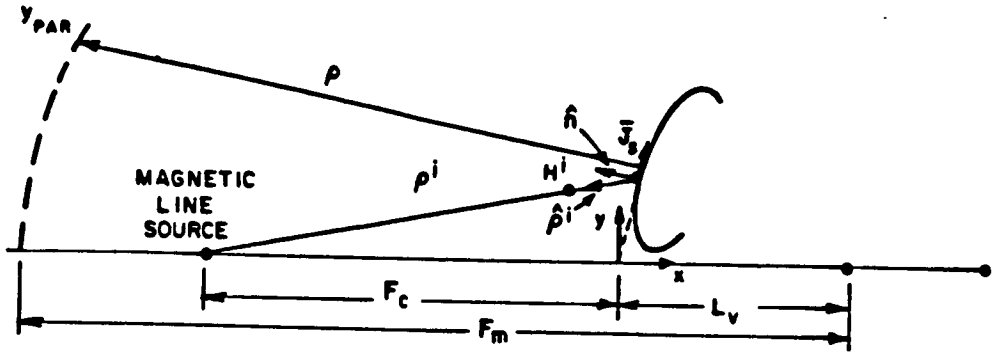

Figure 4.5 Physical optics analysis.

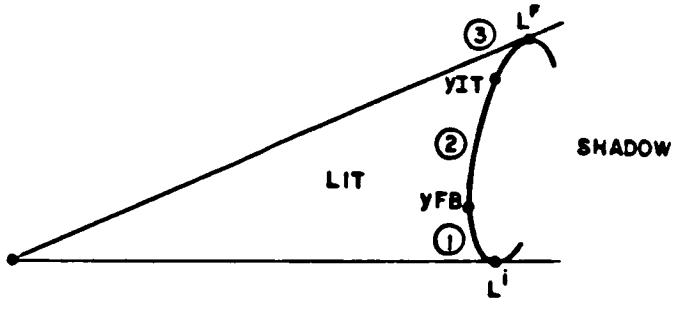

Figure 4.6 Three integration regions.

$$\hat{t} \times \hat{\rho} = (t_x \rho_y - t_y \rho_x)\hat{z} \tag{4.68}$$

$$\hat{z} \cdot (\hat{t} \times \hat{\rho}) = t_x \rho_y - t_y \rho_x, \text{ and} \tag{4.69}$$

$$\hat{\rho}_i = \frac{-(Fc - Lv + x)\hat{X} - Y\hat{y}}{\rho_i} \quad . \tag{4.70}$$

The normal $(\hat{n})$ is known from Equation (4.54) so the remaining dot product is known in the integral. The integration is carried out over three regions as shown in Figure 4.6. The lit region endpoints (L^i and L^f) may be found using an interative bisection technique. Once these points are known, the integration is carried out suppressing the leading constants. Then, the scattered field is given by

$$Hz = \int_{L^i}^{L^f} (t_x \rho_y - t_y \rho_x) \frac{e^{-j2\pi(\rho_i + \rho)}}{\sqrt{\rho_i \rho}} (\hat{\rho}_i \cdot \hat{n}) dY_\rho \tag{4.71}$$

or numerically

$$Hz \approx \sum_{1}^{N} (t_x \rho_y - t_y \rho_x) \frac{e^{-j2\pi(\rho_i + \rho)}}{\sqrt{\rho_i \rho}} (\hat{\rho}_i \cdot \hat{n}) \Delta Y_p \tag{4.72}$$

where Y_p is the parameter defining the curve (or just y in the case of the hyperbola section). This is evaluated using the trapezoidal rule for numerical integration.

A typical subreflector is shown in Figure 4.7. The slope or first derivative is also present to show the slope transition from the reflector to the blended surfaces. The UTD and physical optics plots follow. Next, a smaller subreflector is shown with the same size surfaces (see Figure 4.8). In this case the subreflector is too small

ϕ_v = 45°
ϕ_r = 5°
Fm = 81.33λ
Fc = 81.33λ
Major Axis = 2.67λ
Minor Axis = 1.73λ
Hyperbola Section = 10.67λ
Edges attached
at 4.12λ and 6.543λ

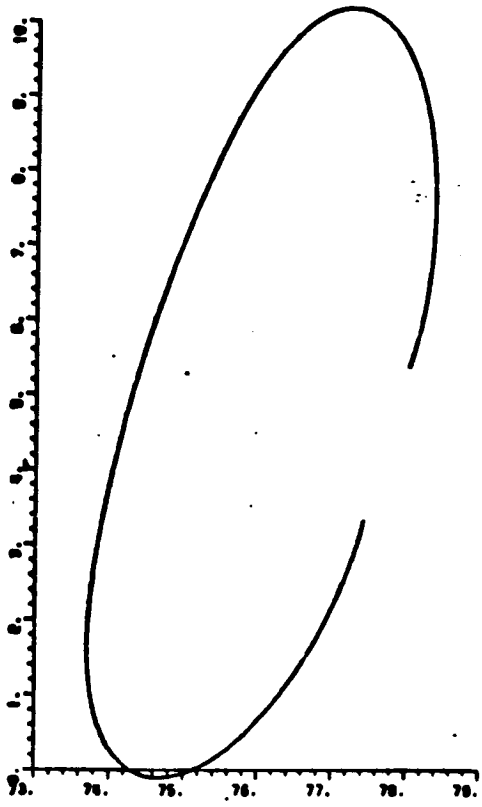

(a) Subreflector with blended edges.

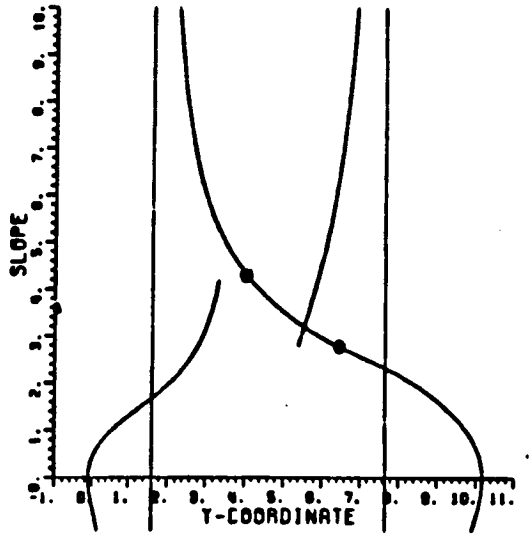

(b) First derivative plot.

Figure 4.7 Subreflector with blended surfaces.

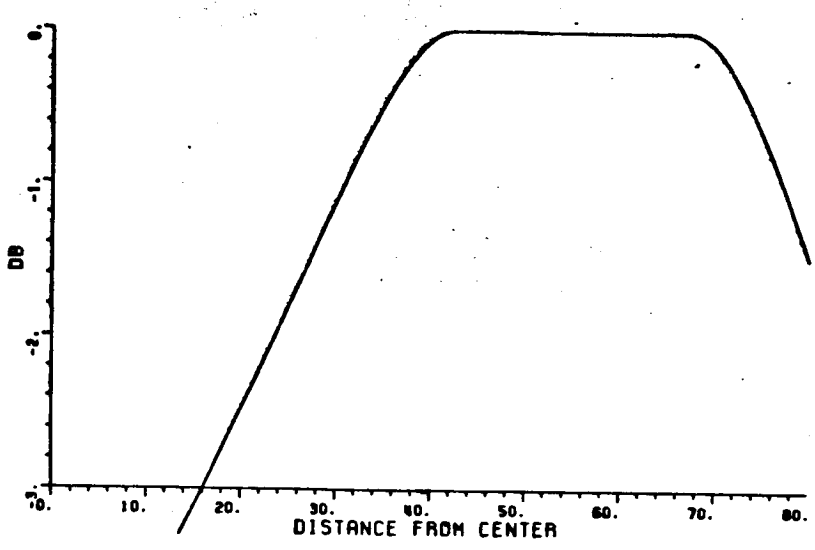

(c) Geometrical optics plot.

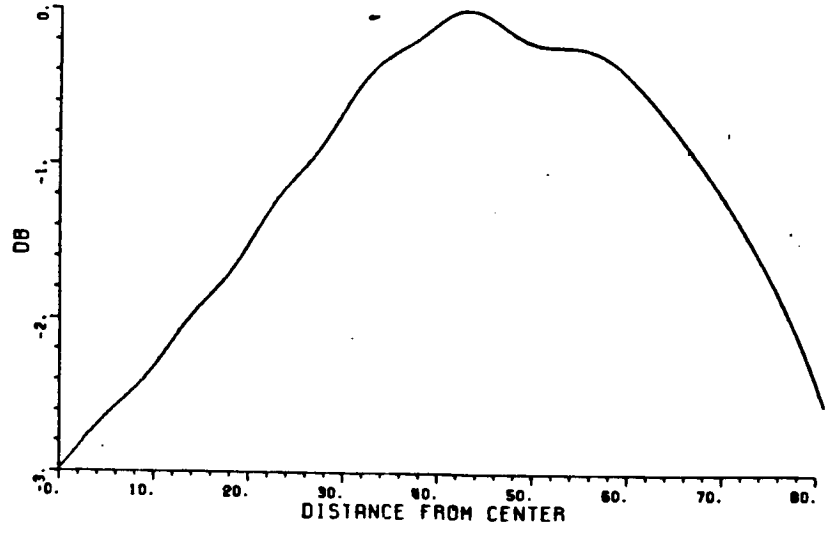

(d) Physical optics plot.

Figure 4.7 (Continued).

ϕ_v = 45°
ϕ_r = 5°
Fm = 81.33λ
Fc = 81.33λ
Major Axis = 2.67λ
Minor Axis = 1.73λ
Hyperbola section = 10.67λ
Edges attached
at 5λ abd 5.5λ

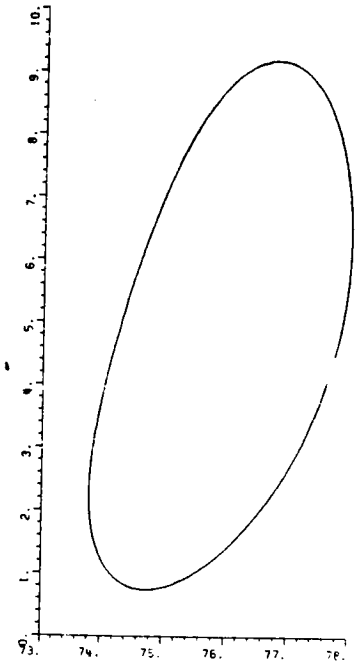

(a) Subreflector with blended surfaces.

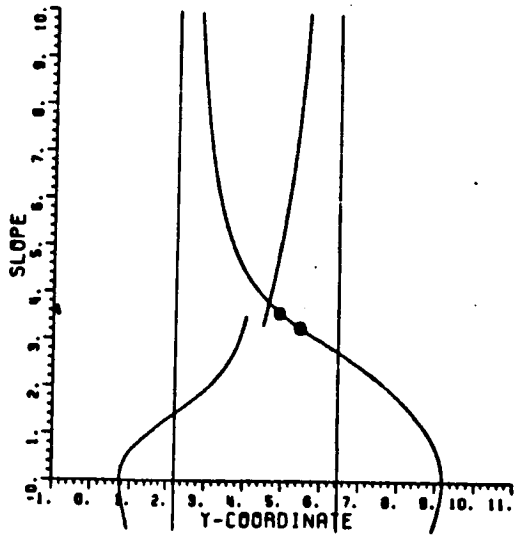

(b) First derivative plot.

Figure 4.8 Smaller subreflector with same size surfaces.

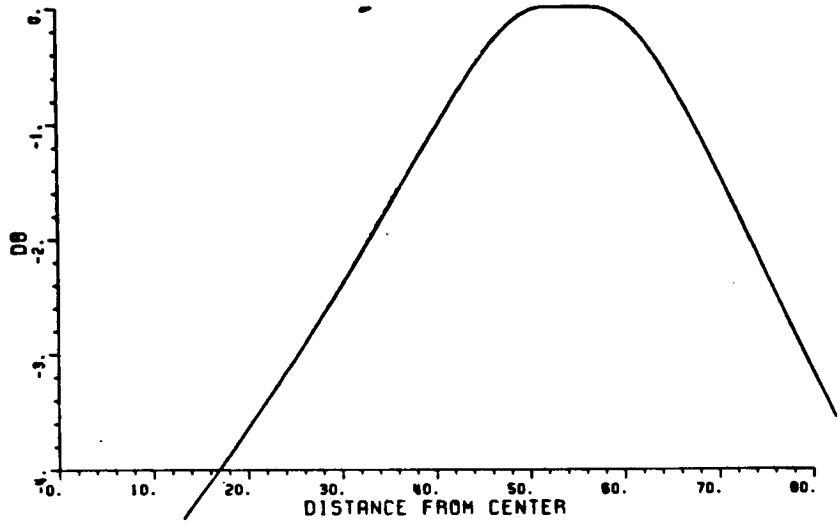

(c) Geometrical optics plot.

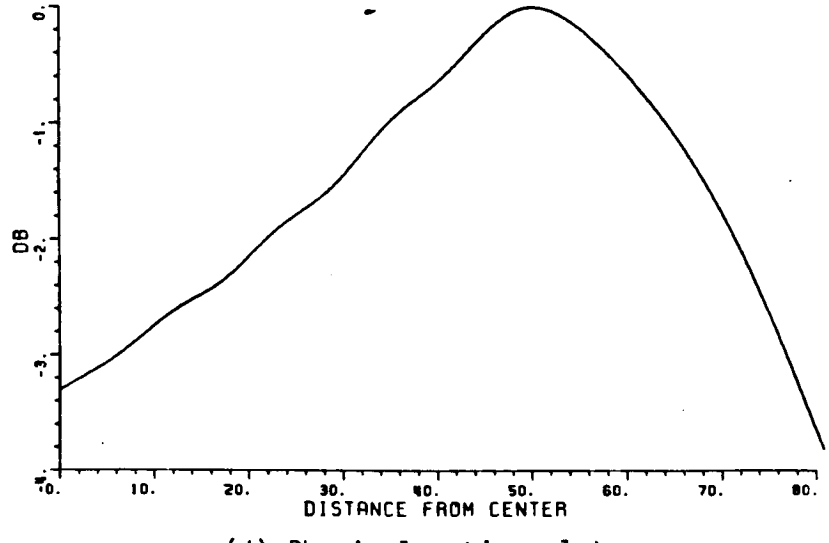

(d) Physical optics plot.

Figure 4.8 (Continued).

in terms of wavelengths. Finally the original size subreflector with smaller surfaces is considered (see Figure 4.9). Again, performance suffers and the slope transition in this last figure is much more abrupt.

It is also helpful and convenient to look at the far field of the subreflector using geometrical optics (GO) and moment method theory. For GO, the far field is given by

$$U = \frac{e^{-jk\rho_i}}{\sqrt{\rho_i}} \sqrt{\frac{\rho_c}{\rho_c+\rho_s}}\, e^{-jk\rho_s} \tag{4.73}$$

with the variables shown in Figure 4.10. Now ρ_s is the far field distance so

$$\rho_c+\rho_s \approx \rho_s \quad , \text{ and} \tag{4.74}$$

$$U = \frac{e^{-jk\rho_i}}{\sqrt{\rho_i}} \sqrt{\rho_c}\, \frac{e^{-jk\rho_s}}{\sqrt{\rho_s}} \quad . \tag{4.75}$$

But this last factor is a common factor and may be ignored yielding

$$U = \sqrt{\frac{\rho_c}{\rho_i}}\, e^{-jk\rho_i} \tag{4.76}$$

at a specified angle ϕ which may be easily found from previous calculations.

For the moment method, points are set up along the curve of the subreflector a distance "ds" apart. The distance used was usually about 0.2 wavelengths at a particular frequency. On the blended surfaces, "ds" was approximated as a small line segment. For the hyperbola section (Figure 4.11), the uniform segments were found using

ϕ_v = 45°
ϕ_r = 5°
Fm = 81.33λ
Fc = 81.33λ
Major Axis = 2.67λ
Minor Axis = 0.433λ
Hyperbola section = 2.67λ
Edges attached at
4.12λ and 6.543λ

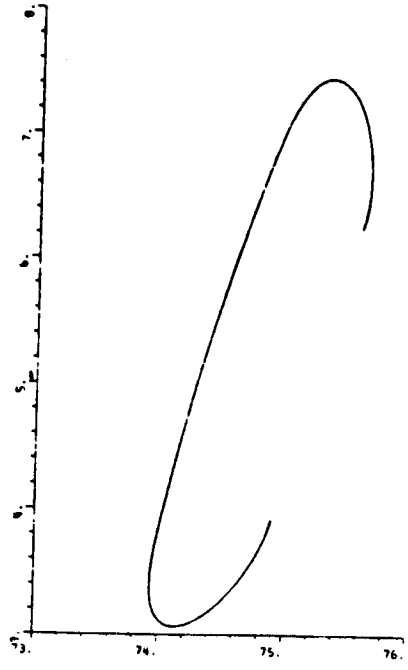

(a) Subreflector with blended edges.

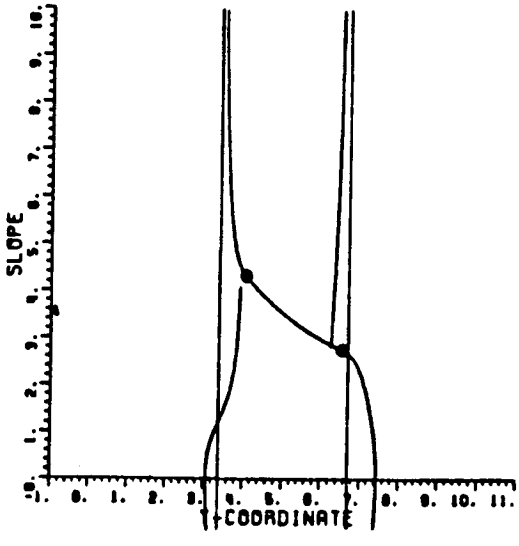

(b) First derivative plot.

Figure 4.9 Original subreflector with smaller blended surfaces.

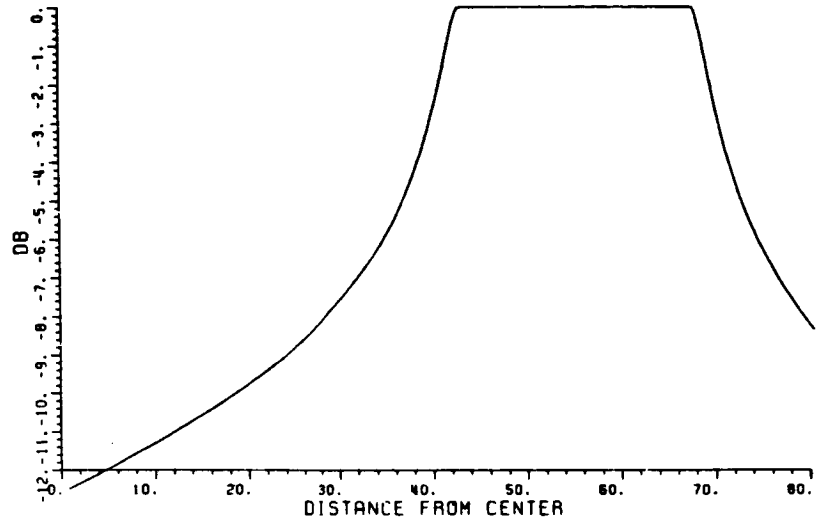

(c) Geometrical optics plot.

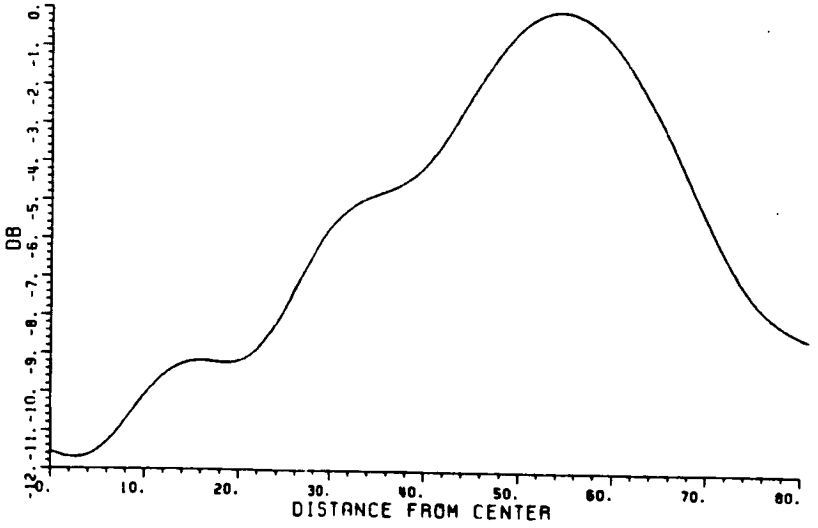

(d) Physical optics plot.

Figure 4.9 (Continued).

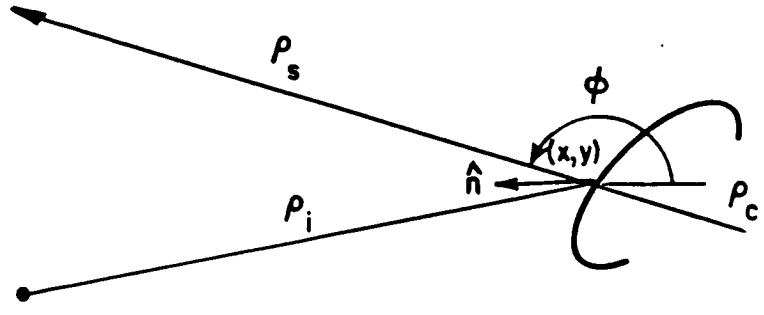

Figure 4.10 Far field from subreflector.

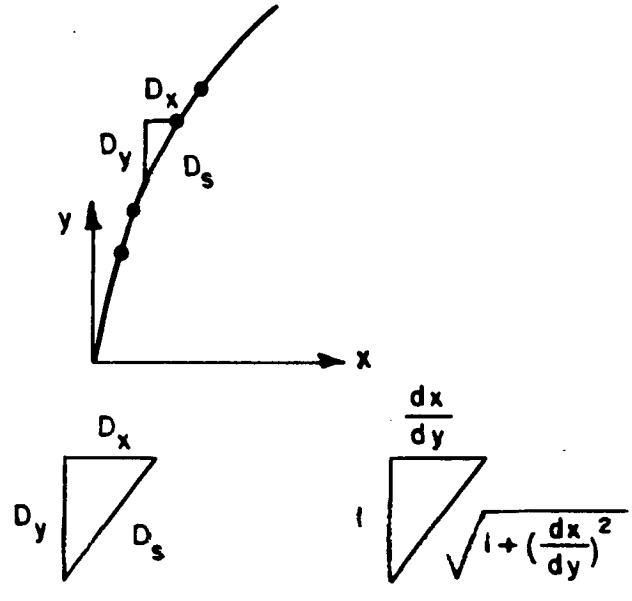

Figure 4.11 Moment method geometry.

$$\frac{dx}{dy} = \frac{ay/b^2}{[1+(y/b)^2]^{1/2}} \tag{4.77}$$

at the bottom point and

$$dy = \frac{ds}{[1+(dx/dy)^2]^{1/2}} \quad . \tag{4.78}$$

This dy is added to the previous y to obtain the next y from which the corresponding x coordinate may be calculated. Once the subreflector is represented by the point geometry spaced ds apart, the moment method program may be run using this information to obtain far field plots. Using the same subreflector geometries as in Figures 4.7 through 4.9, GO and moment method far field patterns are shown in Figures 4.12 through 4.14. The moment method analysis provides accurate results and for the relatively small subreflector is easily and quickly implemented. These results also show the closeness of including only the reflected field in the UTD analysis. When these two procedures yield results that differ greatly, then more than the reflected field is being seen, and the design must be compensated so that it looks more like a simple reflective surface. Once satisfactory performance (flat amplitude over area of main reflector to be illuminated) is obtained, the design of the main reflector may proceed.

As with the subreflector, the main reflector will consist of a parabolic surface with two blended surfaces attached (Figure 4.15). Of course, the parabolic section is given by

$$x = y^2/(4Fm). \tag{4.79}$$

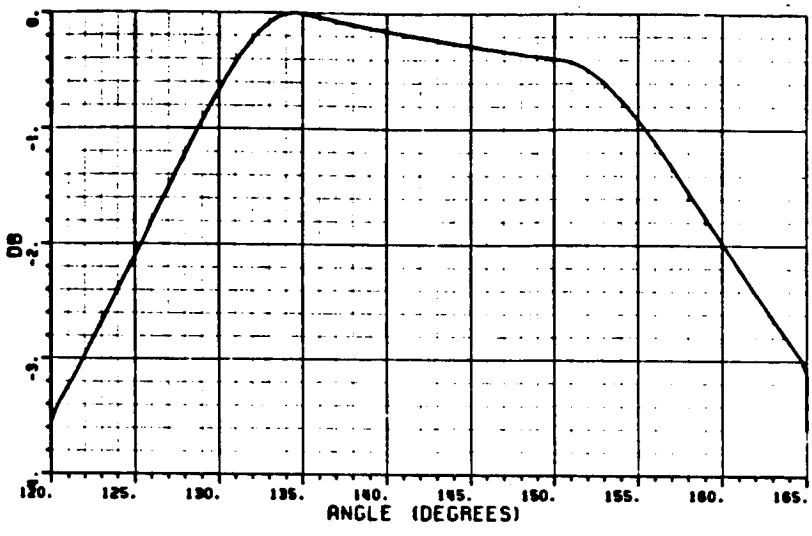

(a) Geometrical optics plot for geometry of Figure 4.7 (a).

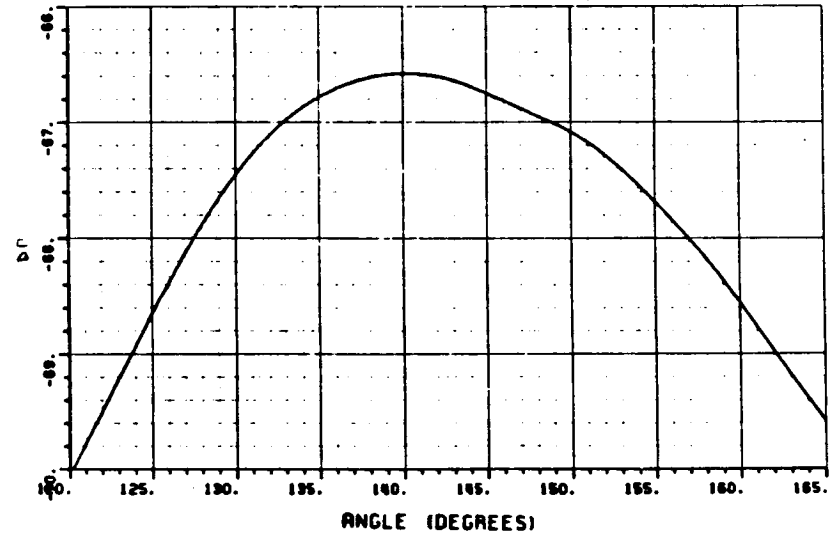

(b) Moment method plot for geometry of Figure 4.7 (a).

Figure 4.12 Field plots for geometry of Figure 4.7 (a).

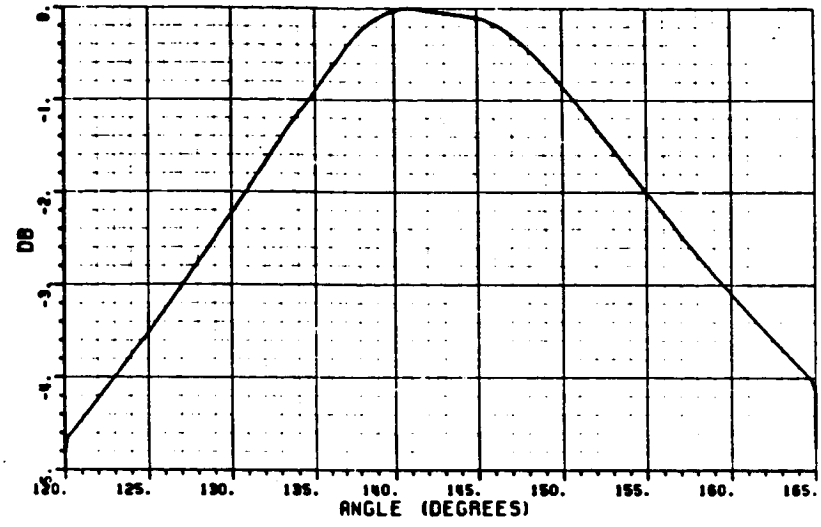

(a) Geometrical optics plot for geometry of Figure 4.8 (a).

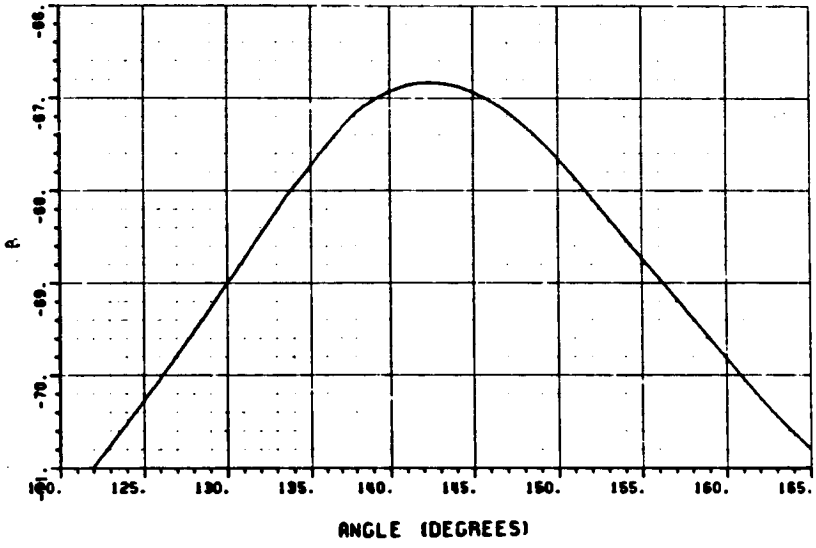

(b) Moment method plot for geometry of Figure 4.8 (a).

Figure 4.13 Field plots for geometry of Figure 4.8 (a).

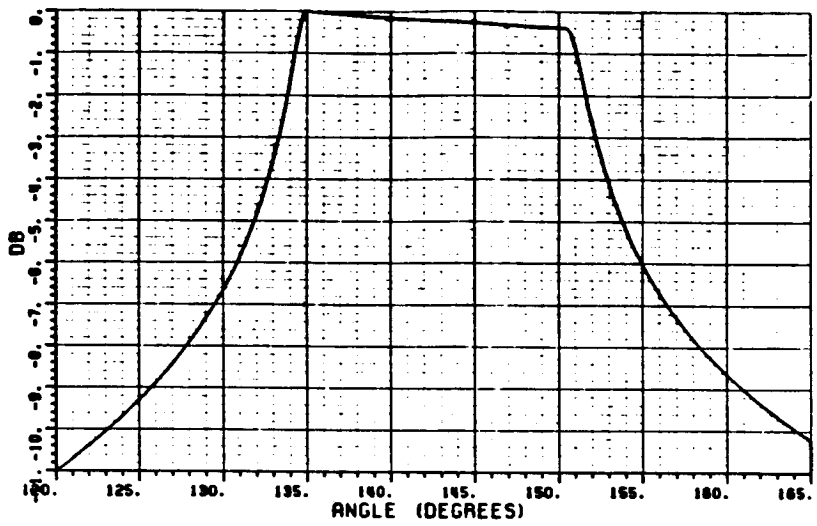

(a) Geometrical optics plot for geometry of Figure 4.9 (a).

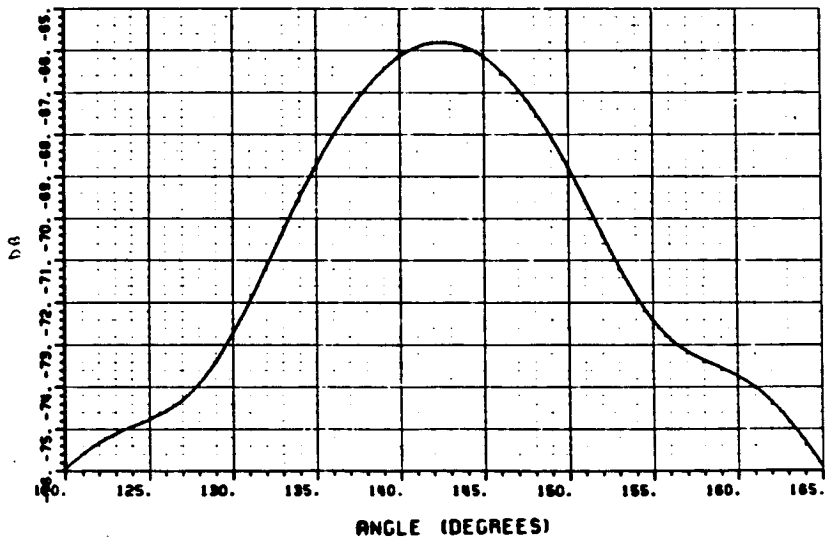

(b) Moment method plot for geometry of Figure 4.9 (a).

Figure 4.14 Field plots for geometry of Figure 4.9 (a).

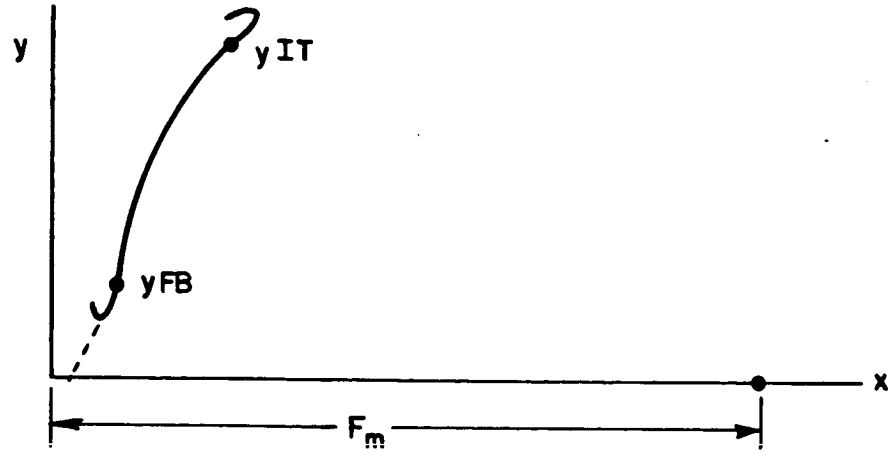

Figure 4.15 Main reflector with blended surfaces.

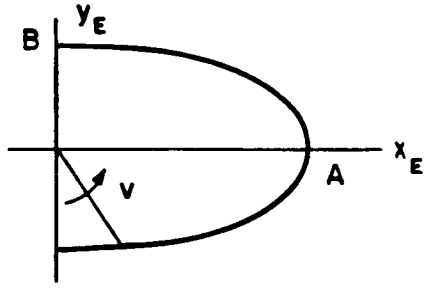

Figure 4.16 Ellipse for upper edge.

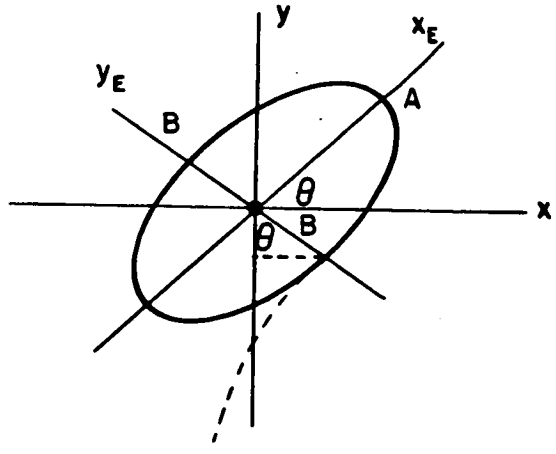

Figure 4.17 Tilted ellipse.

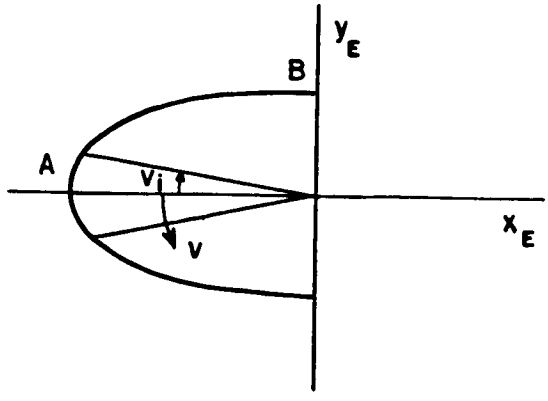

Figure 4.18 Ellipse for bottom edge.

The blending function used on the top edge is

$$P = \frac{1+\cos\frac{\pi v}{vf}}{2} \qquad 0 < P < 1 \tag{4.80}$$

where

$$v = v_f \frac{Y_P - YIT}{YFT - YIT} \qquad 0 < v < v_f \ . \tag{4.81}$$

The ellipse in Figure (4.16) is parameterized by

$$XE = A\sin v, \text{ and} \tag{4.82}$$

$$YE = -B\cos v \ . \tag{4.83}$$

The normal of the parabola is given by

$$\hat{n} = \frac{-\hat{x}+(Y/2Fm)\,\hat{y}}{[1+(Y/2Fm)^2]^{1/2}} \tag{4.84}$$

so the origin of the blended ellipse is located at

$$X_{ELT} = \frac{-B}{[1+(\frac{YIT}{2Fm})^2]^{1/2}} + \frac{YIT^2}{4Fm} \text{ , and} \tag{4.85}$$

$$Y_{ELT} = \frac{\frac{B(YIT)}{2Fm}}{[1+(\frac{YIT}{2Fm})^2]^{1/2}} + YIT. \tag{4.86}$$

The angle of the main axis of the ellipse is now tilted (Figure 4.17) and given by

$$\theta = \sin^{-1} \frac{[YIT^2/(4FM)-X_{ELT}]}{B} \tag{4.87}$$

so that the elliptical curve is generated by

$$X = A\sin v\cos\theta + B\cos v\sin\theta + X_{ELT} \tag{4.88}$$

and

$$Y = A\sin v\sin\theta - B\cos v\cos\theta + Y_{ELT} \text{ .} \tag{4.89}$$

Finally the top blended surface is generated by

$$X = (\frac{Yp2}{4Fm})P + (A\sin v\cos\theta + B\cos v\sin\theta + X_{ELT})(1-P) \tag{4.90}$$

and

$$Y = Y_pP + (A\sin v\sin\theta - B\cos v\cos\theta + Y_{ELT})(1-P) \tag{4.91}$$

where Y_p is a parameter that varies between YIT and YFT.

For the bottom surface, the ellipse (Figure 4.18) is parameterized by

$$XE = -A\cos v \tag{4.92}$$

and

$$YE = -B\sin v \quad . \tag{4.93}$$

The origin of the ellipse in this case is at

$$X_{ELB} = \frac{-B}{[1+(\frac{YFB}{2Fm})^2]^{1/2}} + \frac{YFB^2}{4Fm} \tag{4.94}$$

and

$$Y_{ELB} = \frac{\frac{B(YFB)}{2Fm}}{[1+(\frac{YFB}{2Fm})^2]^{1/2}} + YFB \quad . \tag{4.95}$$

The tilt angle of the ellipse is

$$\theta = \sin^{-1}\left[\frac{YFB^2/(4Fm)-X_{ELB}}{B}\right] \tag{4.96}$$

and the ellipse curve is given by

$$X = -A\cos v\cos\theta + B\sin v\sin\theta + X_{ELB} \quad , \text{ and} \tag{4.97}$$

$$Y = -A\cos v\sin\theta - B\sin v\cos\theta + Y_{ELB} \quad . \tag{4.98}$$

The blending function for this surface is

$$P = \frac{1+\cos\pi\left[\frac{v-v_i}{\pi/2-v_i}\right]}{2} \qquad 0 < P < 1 \tag{4.99}$$

with

$$v = (\pi/2 - v_i)(\frac{Y_P-YIB}{YFB-YIB})+v_i \qquad v_i < v < \pi/2 \quad . \tag{4.100}$$

Then the bottom blended edge is generated by

$$X = \left(\frac{Y_P^2}{4Fm}\right)(1-P)+(-A\cos v\cos\theta + B\sin v\sin\theta + X_{ELB})P \qquad (4.101)$$

and

$$Y = Y_P(1-P) + (-A\cos v\sin\theta - B\sin v\cos\theta + Y_{ELB})P \quad . \qquad (4.102)$$

The entire main reflector surface may now be generated. As in the case of the subreflector, larger surfaces lead to flatter field performance. This overall size is determined by the major axis length plus the parabolic section length blended together. The parabolic section length is determined by (YIT,YFT) and (YIB,YFB) for the top and bottom surfaces , respectively. The minimum radius of curvature of the surface is determined by the minor axis dimension, and this is kept greater than a quarter of wavelength at the lowest frequency of operation. A final rule of thumb is to make the length of the parabolic section about four times longer than the major axis of the ellipse in order to make the slope transition from the parabola to the blended surface as gradual as possible. As in the subreflector case, v_i is fixed at $-\pi/2$, and v_f is fixed at π. This assures that the surface extends well into the back area of the reflector. Since much of this blended surface is excessive, some of it may be eliminated by controlling the range over which the total reflector is generated. This is easier to implement than changing the variables which govern the shape of the curve which would result in a different surface design.

With the geometry given, the field in the plane of interest or target area may now be calculated. The main reflector is analyzed alone

by placing the source at the virtual feed. The moment method procedure and GO are used to analyze the main reflector. First, the moment method is used to consider some special cases.

In Figure 4.19, a typical reflector with sharp edges is shown. The moment method plot follows. The ripple may be greatly reduced by attaching elliptic rolled surfaces with no blending involved as in Figure 4.20. Now using a linear blending function of the form v/v_f instead of the cosine function described earlier, the field plot in Figure 4.21 shows even more improvement. A parabolic blending function of the form $(v/v_f)^2$ is considered next. The improvement of the field in this case is shown in Figure 4.22. Finally, the original cosine blending function is used as shown in Figure 4.23. It and the parabolic blending show similar results. The cosine blending is chosen since it gives the best results and also does a good job of shaping the surfaces in the back region. The distance to the target area or plane of interest is also a variable, and care must be taken in choosing this distance. If the observation plane is too close to the reflector, one is limited by the feed position. If the plane is moved too far away from the reflector, far field effects become apparent, and the plane wave gradually becomes more and more tapered. These effects are shown in Figure 4.24 for various observation plane distances where "DISPLN" is referenced to zero at the virtual feed. The case for DISPLN = 0 is shown already in Figure 4.23b.

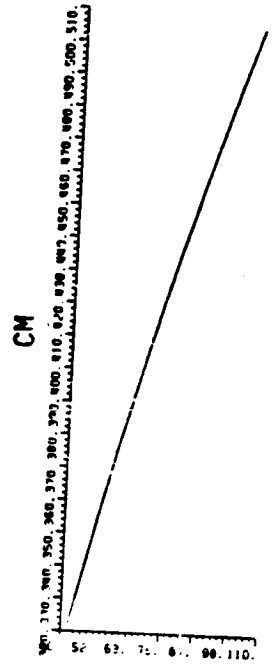

ϕ_v = 45°
ϕ_r = 5°
Fm = 610 cm
Top at 505 cm
Bottom at 322 cm

(a) Parabolic reflector section.

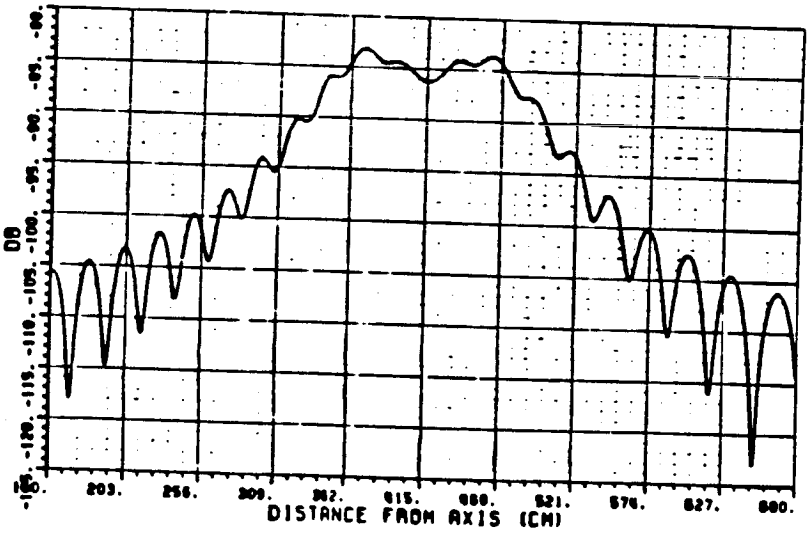

(b) Moment method plot.

Figure 4.19 Parabolic reflector section and field plot.

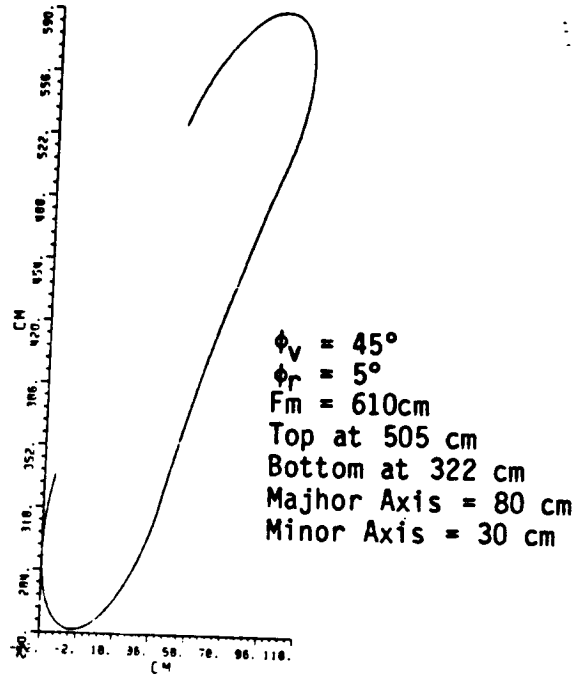

(a) Reflector with elliptic rolled edges.

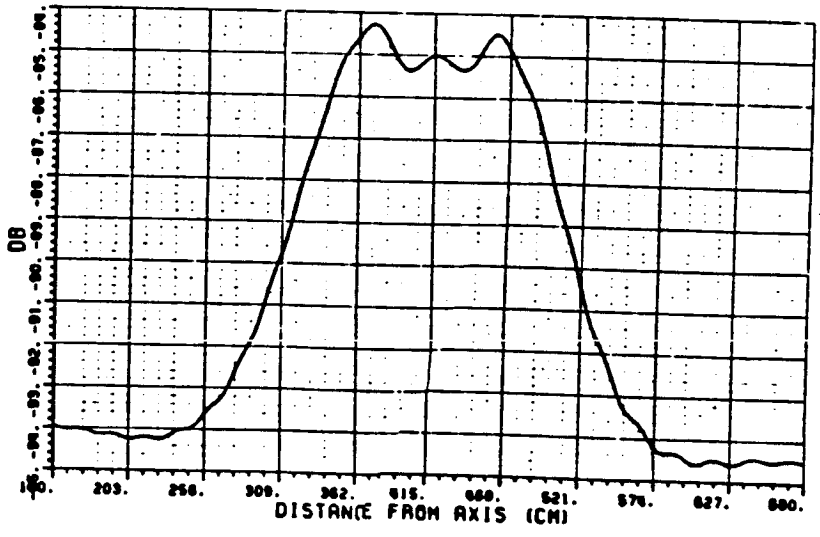

(b) Moment method plot. Frequency = 4 GHz

Figure 4.20 Reflector with elliptic rolled surfaces and field plot.

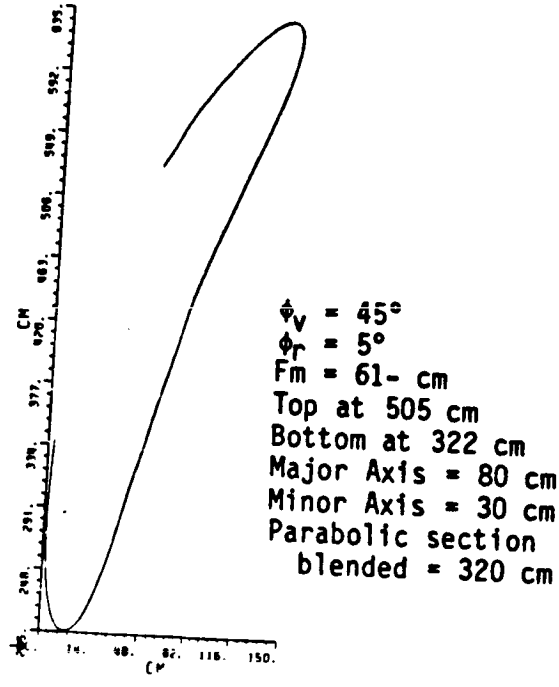

(a) Linearly blended edges.

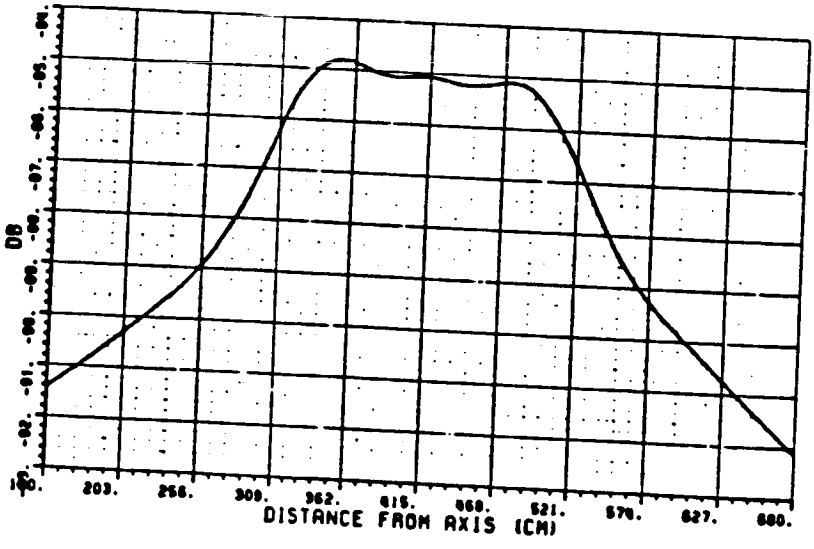

(b) Moment method plot. Frequency = 4 GHz

Figure 4.21 Reflector with linearly blended surfaces and field plot.

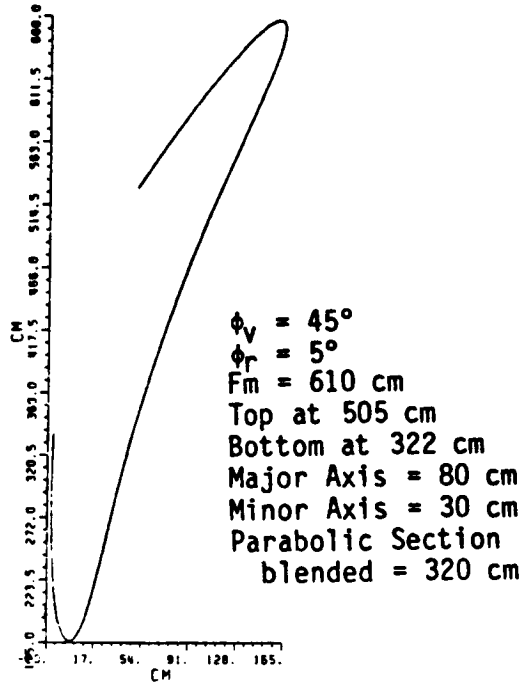

(a) Parabolic blended edges.

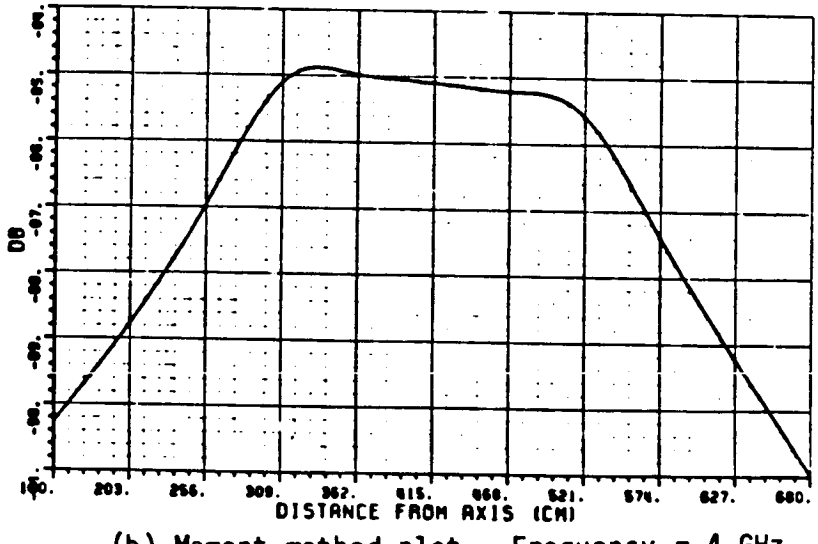

(b) Moment method plot. Frequency = 4 GHz

Figure 4.22 Reflector with parabolic blended surfaces and field plot.

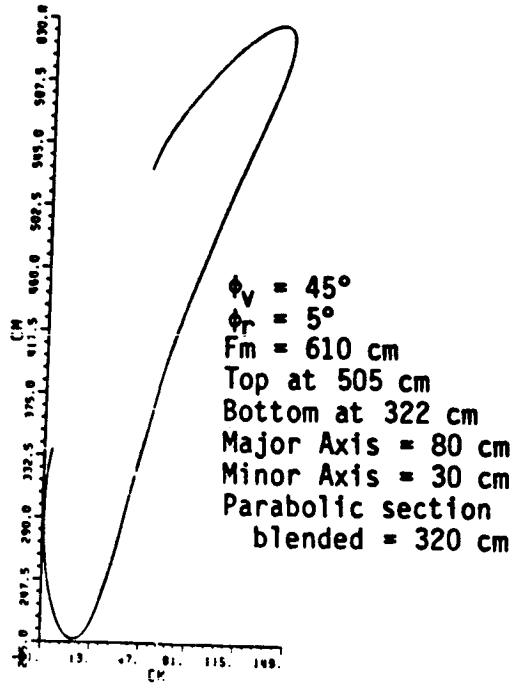

(a) Cosine blended edges.

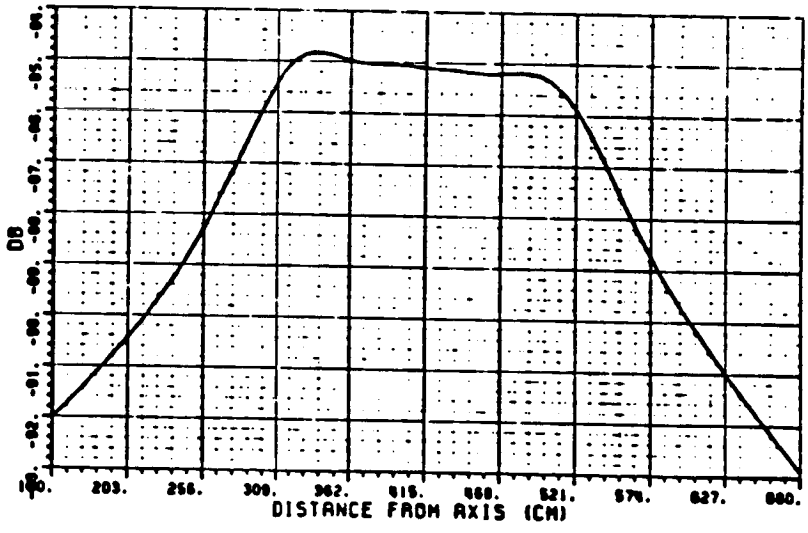

(b) Moment method plot. Frequency = 4 GHz

Figure 4.23 Reflector with cosine blended surfaces and field plot.

The GO reflected field for the main reflector will now be calculated (see Figure 4.25). In the parabolic region, the reflected field is given by

$$U^{REF} = \frac{e^{-jk(\rho_i+\rho_r)}}{\sqrt{\rho_i}} \tag{4.103}$$

with

$$\rho_i = [(Fm-X)^2+Y^2]^{1/2} \quad , \tag{4.104}$$

$$\rho_r = Fm + DISPLN-X, \text{ and} \tag{4.105}$$

$$YPLN = Y \quad . \tag{4.106}$$

For the top and bottom blended surfaces, the reflected field is

$$U^{REF} = \frac{e^{-jk\rho_i}}{\sqrt{\rho_i}} \sqrt{\frac{\rho_c}{\rho_c+\rho_r}}\, e^{-jk\rho_r} \tag{4.107}$$

with

$$\frac{1}{\rho_c} = \frac{1}{\rho_i} + \frac{2}{R_c \cos\theta_i} \tag{4.108}$$

and ρ_i as before. To calcualte R_c and $\cos\theta_i$, the partial derivatives with respect to Y_p must be found. For the bottom surface, one finds the following:

$$X' = X'_{PARA}(1-P) + X_{PARA}(-P') + X'_{ELL}P + X_{ELL}P' \tag{4.109}$$

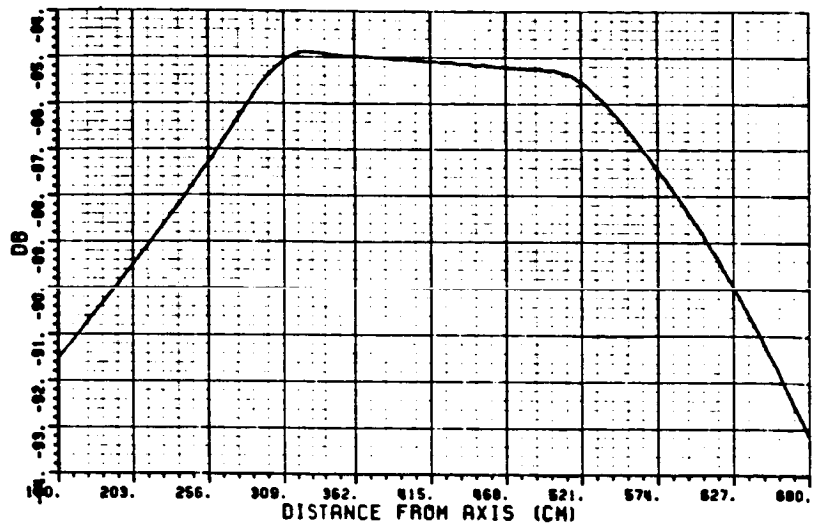

(a) DISPLN = -305cm.

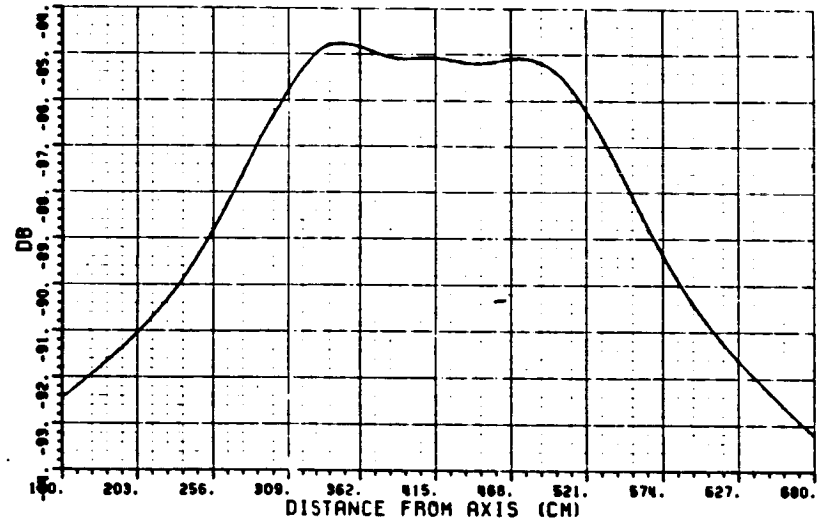

(b) DISPLN = 305cm.

Figure 4.24 Moment method plots for various distances to the observation plane.

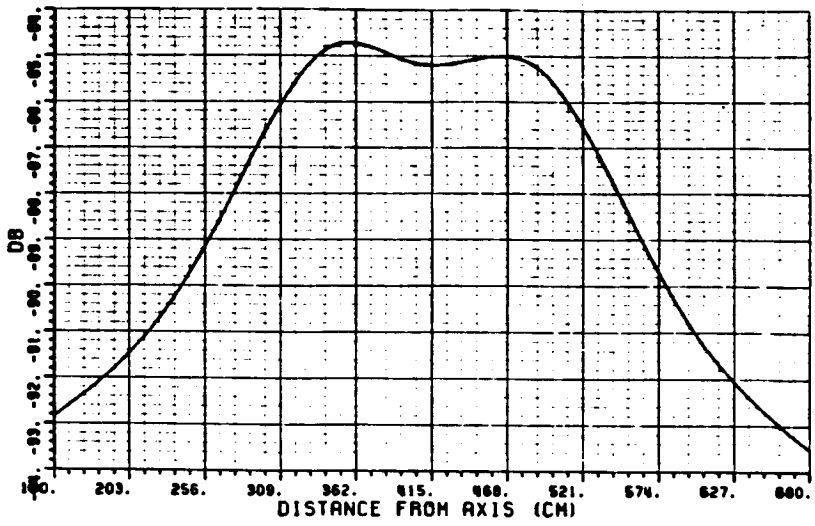

(c) DISPLN = 610cm.

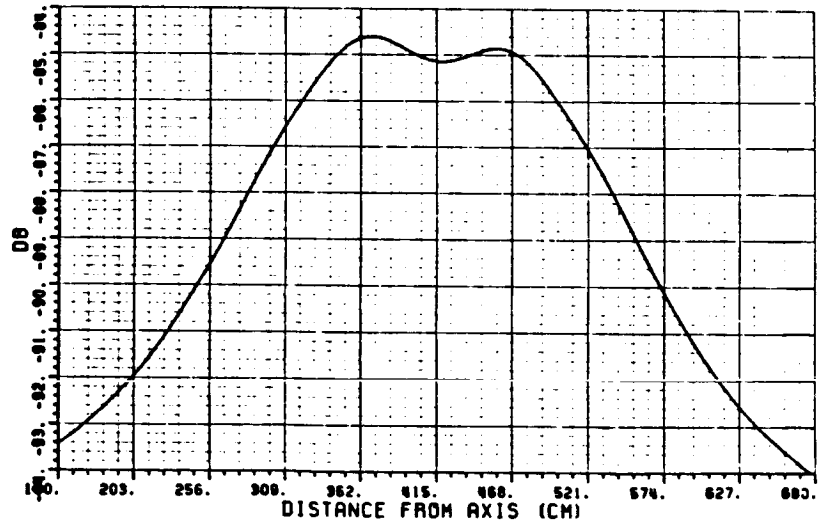

(d) DISPLN = 1220cm.

Figure 4.24 (Continued).

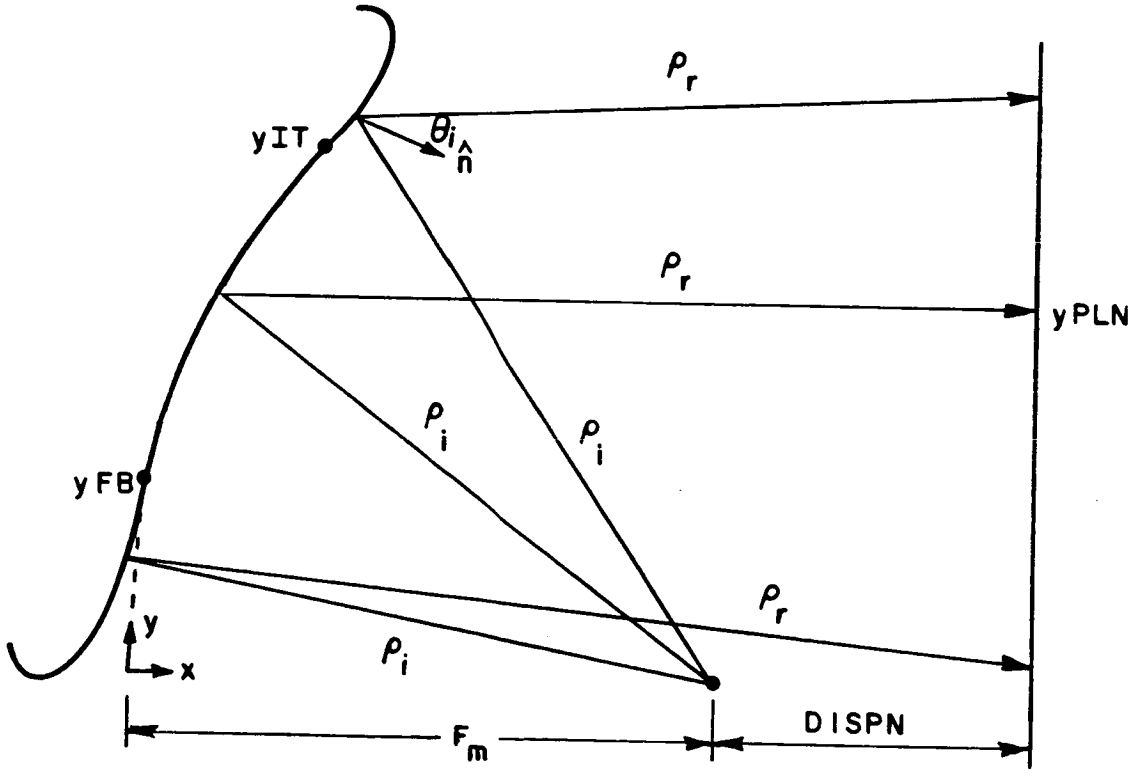

Figure 4.25 Reflected field from main reflector.

$$X'_{PARA}(Yp) = \frac{Y_p}{2Fm} \tag{4.110}$$

$$P'(Yp) = -\frac{1}{2}\sin\left[\pi\left(\frac{v-v_i}{\pi/2-v_i}\right)\right]\left(\frac{\pi}{YFB-YIB}\right) \tag{4.111}$$

$$X'_{ELL}(Yp) = [A\sin v\cos\theta + B\cos v\sin\theta]\left(\frac{\pi/2-v_i}{YFB-YIB}\right) \tag{4.112}$$

$$X'' = X''_{PARA}(1-P) + 2X'_{PARA}(-P') + X_{PARA}(-P'')$$

$$+ X''_{ELL}P + 2X'_{ELL}P + X_{ELL}P'' \tag{4.113}$$

$$X''_{PARA}(Yp) = \frac{1}{2Fm} \tag{4.114}$$

$$P''(Yp) = \frac{1}{2}\cos\left[\pi\left(\frac{v-v_i}{\pi/2-vi}\right)\right]\left[\frac{\pi}{YFB-YIP}\right]^2 \tag{4.115}$$

$$X''_{ELL} = [A\cos v\cos\theta - B\sin v\sin\theta]\left[\frac{\pi/2-vi}{YFB-YIB}\right]^2 \tag{4.116}$$

$$Y' = (1-P) + Yp(-P') + Y'_{ELL}P + Y_{ELL}P' \tag{4.117}$$

$$Y'_{ELL}(Yp) = (A\sin v\sin\theta - B\cos v\cos\theta)\left(\frac{\pi/2-v_i}{YFB-YIB}\right) \tag{4.118}$$

$$Y'' = -2P' + Yp(-P'') + Y''_{ELL}P + 2Y'_{ELL}P' + Y_{ELL}P'' \quad , \text{ and} \tag{4.119}$$

$$Y''_{ELL}(Yp) = [A\cos v\sin\theta + B\sin v\cos\theta]\left[\frac{\pi/2 - v_j}{YFB-YIB}\right]^2 . \tag{4.120}$$

For the top surface, one obtains the following:

$$X' = X'_{PARA}P + X_{PARA}P' + X'_{ELL}(1-P) + X_{ELL}(-P') \tag{4.121}$$

$$P' = -\frac{1}{2}\sin\left[\frac{\pi v}{v_f}\right]\left(\frac{\pi}{YFT-YIT}\right) \tag{4.122}$$

$$X'_{ELL} = (A\cos v\cos\theta - B\sin v\sin\theta)\left(\frac{v_f}{YFT-YIT}\right) \tag{4.123}$$

$$X'' = X''_{PARA}P + 2X'_{PARA}P' + X_{PARA}P''$$

$$+ X''_{ELL}(1-P) + 2X'_{ELL}(-P') + X_{ELL}(-P'') \tag{4.124}$$

$$P''(Yp) = -\frac{1}{2}\cos\left[\frac{\pi v}{v_f}\right]\left[\frac{\pi}{YFT-YIT}\right]^2 \tag{4.125}$$

$$X''_{ELL}(Yp) = (A\sin v\cos\theta - V\cos v\sin\theta)\left[\frac{v_f}{YFT-YIT}\right]^2 \tag{4.126}$$

$$Y' = P + YpP' + Y'_{ELL}(1-P) + Y_{ELL}(-P') \tag{4.127}$$

$$Y'_{ELL}(Yp) = (A\cos v\sin\theta + B\sin v\cos\theta)\left(\frac{v_f}{YFT-YIT}\right) \tag{4.128}$$

$$Y'' = 2P' + Y_P P'' + Y''_{ELL}(1-P) + 2Y'_{ELL}(-P') + Y_{ELL}(-P'') \quad , \text{ and} \tag{4.129}$$

$$Y''_{ELL} = (-A\sin v\sin\theta + B\cos v\cos\theta)\left(\frac{V_f}{YFT-YIT}\right)^2 \quad . \tag{4.130}$$

From elementary calculus, the position vector is given by

$$\bar{r} = x\hat{x} + y\hat{y} \tag{4.131}$$

with

$$\bar{r}' = x'\hat{x} + y'\hat{y}, \text{ and} \tag{4.132}$$

$$|\bar{r}'| = [(x')^2 + (y')^2]^{1/2} \quad . \tag{4.133}$$

Also, the unit vector is

$$\hat{t} = \frac{\bar{r}'}{|\bar{r}'|} = \frac{x'\hat{x} + y'\hat{y}}{[(y')^2+(y')^2]^{1/2}} \tag{4.134}$$

and

$$\hat{t}' = \frac{\hat{x}[x''-x'(x'x''+y'y'')[(x')^2+(y')^2]^{-1}]+\hat{y}[y''-y'(x'x''+y'y'')[(x')^2+(y')^2]^{-1}]}{[(x')^2+(y')^2]^{1/2}} \quad . \tag{4.135}$$

Finally,

$$\bar{\kappa} = \frac{\hat{t}'}{|\bar{r}'|} \quad . \tag{4.136}$$

The radius of curvature is given by

$$R_c = \frac{1}{|\bar{\kappa}|} \tag{4.137}$$

and the outward facing normal by

$$\hat{n} = \frac{-\vec{\kappa}}{|\vec{\kappa}|} \quad . \tag{4.138}$$

The dot product with the incident vector

$$\hat{\rho}_i = \frac{(Fm-x)\hat{x}-y\hat{y}}{[(Fm-x)^2+y^2]^{1/2}} \tag{4.139}$$

may then be formed yielding

$$\cos\theta_i = \hat{\rho}_i \cdot \hat{n} \tag{4.140}$$

and the caustic distance ρ_c is known.

The reflected field is solved completely when YPLN and ρ_r are known. First, one obtains that

$$\rho_r = [(Fm + DISPLN - x)^2 + (YPLN - y)^2]^{1/2} \quad . \tag{4.141}$$

For the bottom edge (see Figure 4.26), one finds that

$$\alpha_1 = TAN^{-1}((Fm-x)/y) \tag{4.142}$$

and

$$\alpha_2 = \cos^{-1}(\cos\theta_i) \quad . \tag{4.143}$$

The normal is always outward facing so if $\alpha_2 > \pi/2$ then subtract α_2 from π to get desired α_2. Then, one obtains that

$$TAN(\alpha_1+2\alpha_2) = (Fm + DISPN - x)/(y-YPLN) \tag{4.144}$$

or

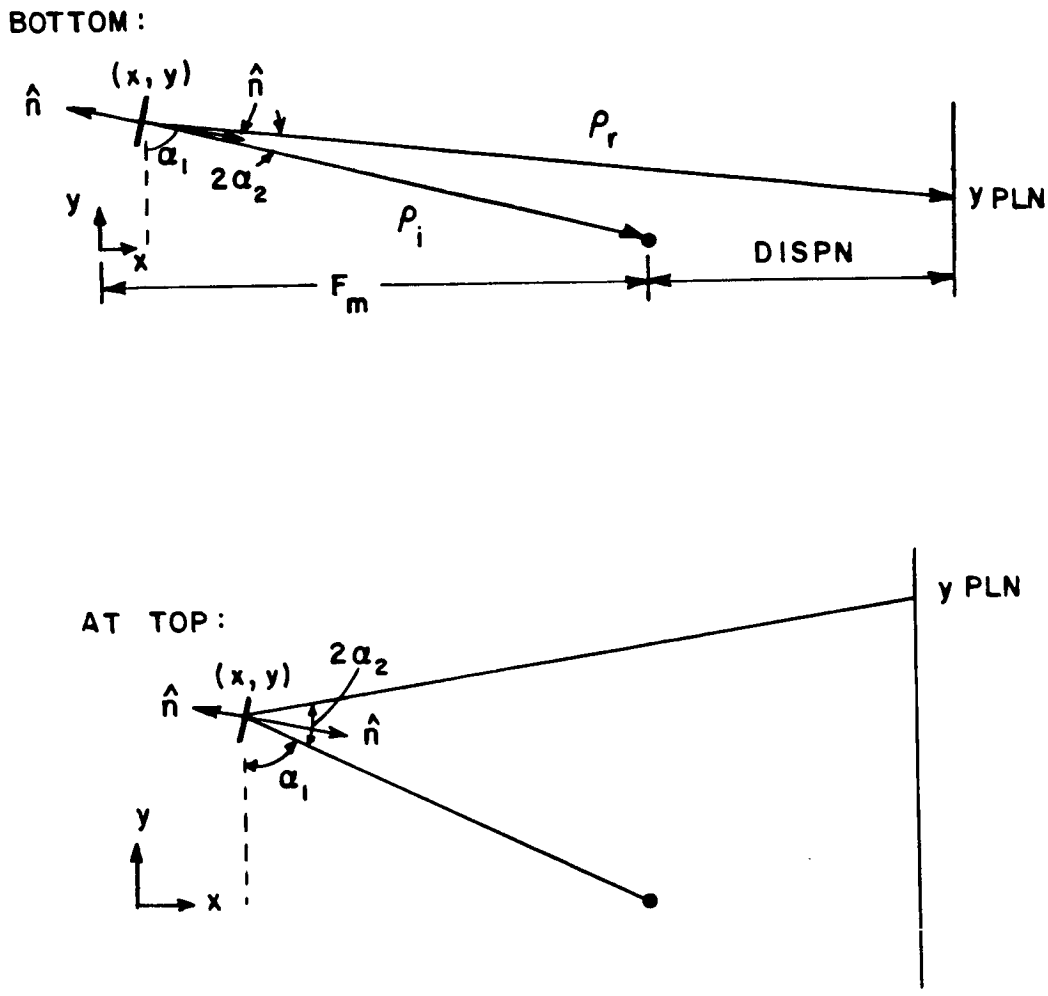

Figure 4.26 Bottom and top reflection points.

$$YPLN = -(Fm + DISPN - x)/TAN(\alpha_1 + 2\alpha_2) + y \quad . \tag{4.145}$$

Similarly for the top surface, one obtains that

$$TAN(\alpha_1 + 2\alpha_2 - \pi/2) = (YPLN - y)/(Fm + DISPN - x) \tag{4.146}$$

or

$$YPLN = (Fm + DISPN - x)\ TAN(\alpha_1 + 2\alpha_2 - \pi/2) + y \quad . \tag{4.147}$$

The reflected field for the surfaces is then given by Equation (4.107).

In Figure 4.27, a typical main reflector is shown. The slope or first derivative is also present to show the slope transition from the reflector to the blended surfaces. The GO and moment method plots follow. Next, smaller surfaces are attached (Figure 4.28) and the degradation in the field is apparent. The GO plot is not as greatly affected since it only contains the reflected field components. Larger surfaces will result in flatter field performance, but a tradeoff must be made between edge size and field performance. Once the field is acceptable, the surfaces should not be increased further in order to keep the triple reflected field to a minimum.

The total system may now be put together. The subreflector and main reflector have been analyzed separately, and there is little further design that can be done at this stage. The offset between the reflectors should be as large as possible, and the blended surfaces have been made as small as possible to reduce the triple reflected field without sacrificing flat field performance.

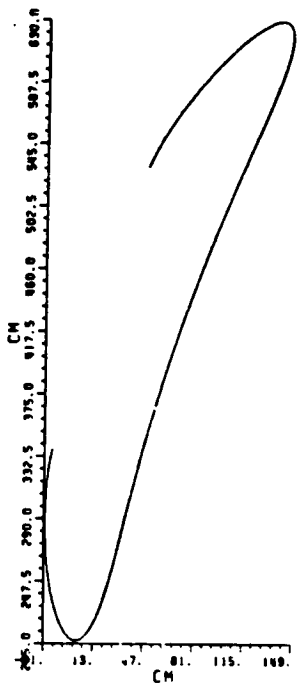

ϕ_v = 45°
ϕ_r = 5°
Fm = 610 cm
Top at 505 cm
Bottom at 322 cm
Major Axis = 80 cm
Minor Axis = 30 cm
Parabolic section
blended = 320 cm

(a) Main reflector with blended surfaces.

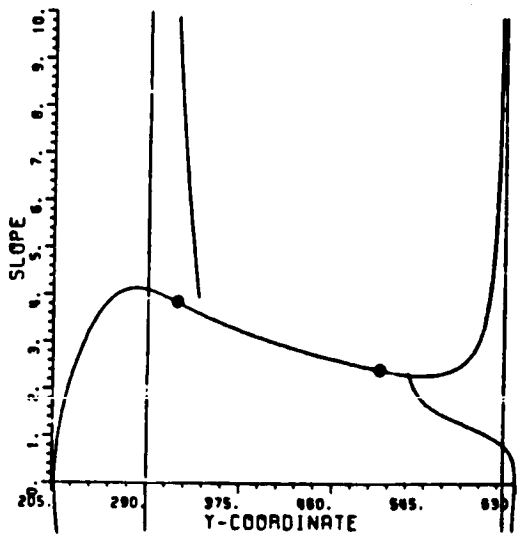

(b) First derivative plot.

Figure 4.27 Parabolic reflector with blended surfaces.

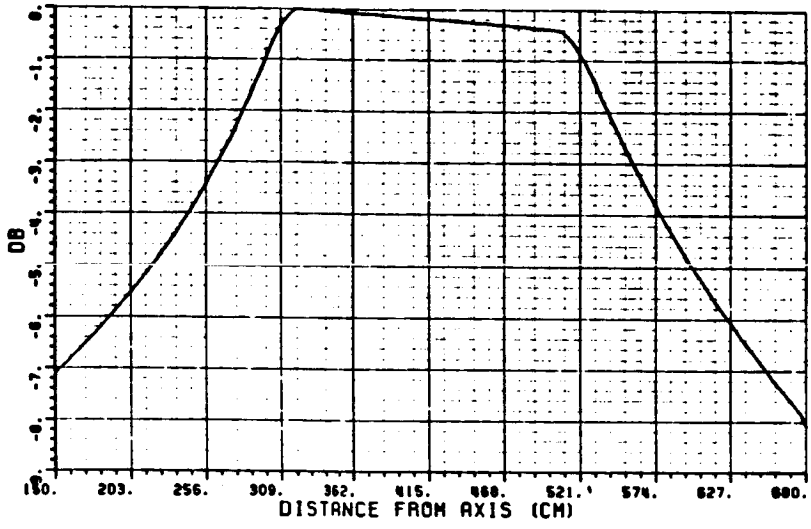

(c) Geometrical optics plot. Frequency = 4 GHz

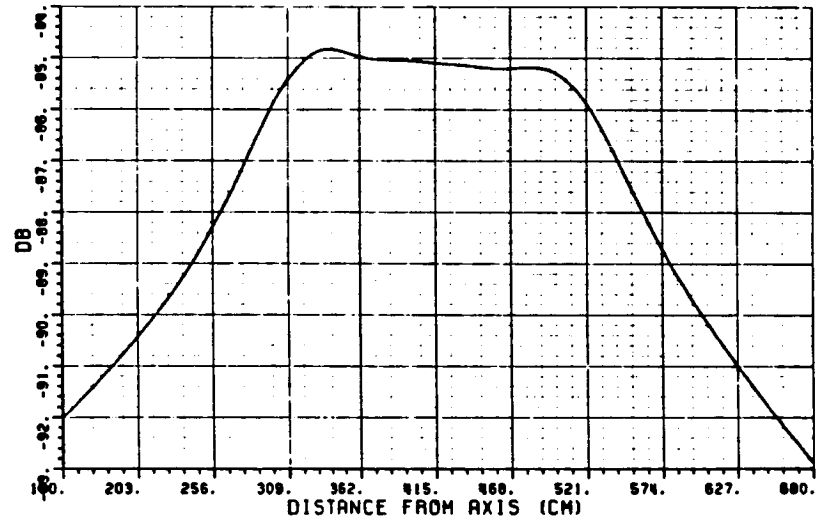

(d) Moment method plot. Frequency = 4 GHZ

Figure 4.27 (Continued).

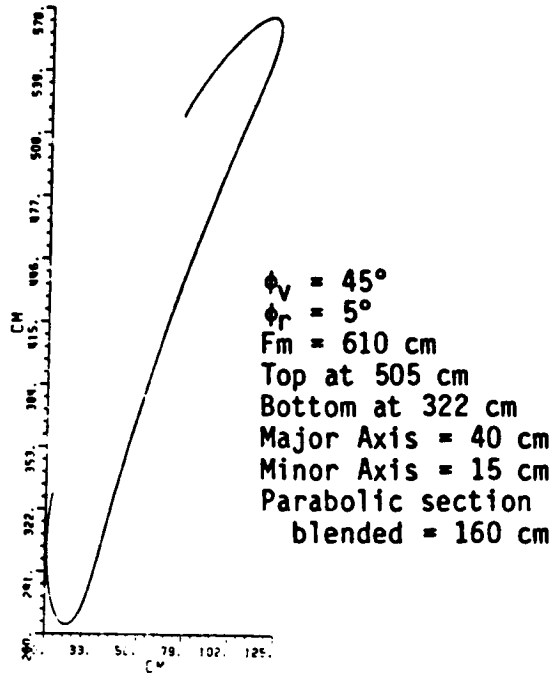

(a) Main reflector with blended edges.

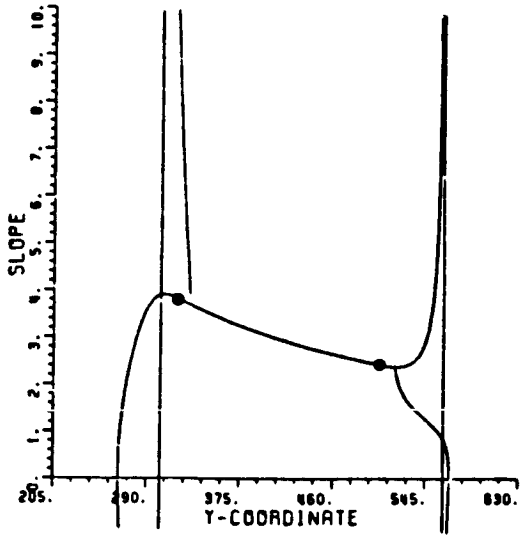

(b) First derivative plot.

Figure 4.28 Parabolic reflector with smaller blended surfaces.

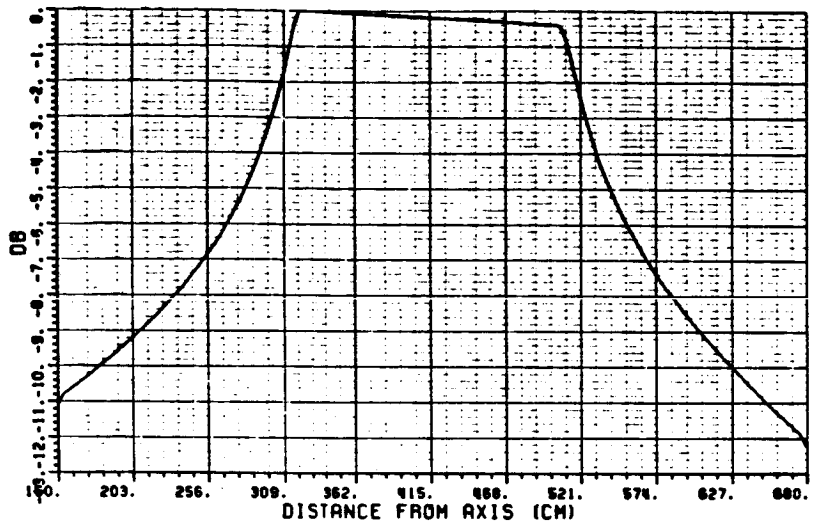

(c) Geometrical optics plot. Frequency = 4 GHz

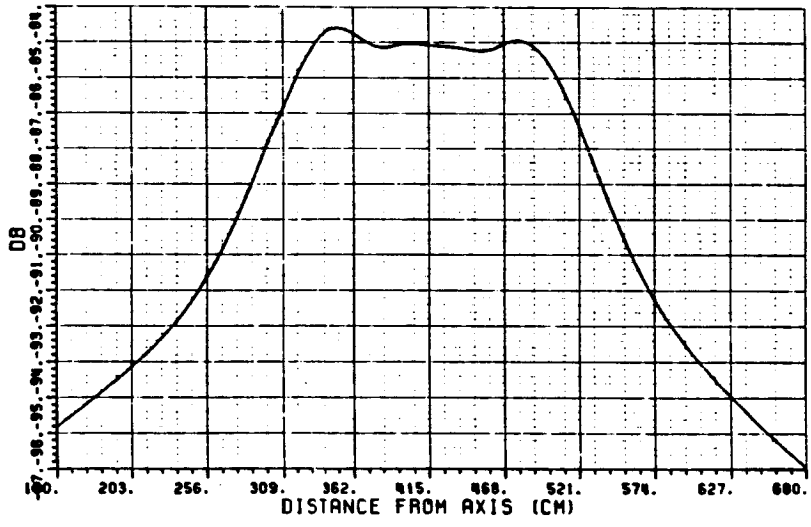

(d) Moment method plot. Frequency = 4 GHz

Figure 4.28 (Continued).

Moment method and GO analysis are used for the entire system and the GO reflected field for the entire system will be examined first. In Figure 4.29, the reflected field from the subreflector that does not interact with the blended surfaces is given by

$$U^{REF} = \sqrt{\frac{\rho_{c1}}{\rho_i(\rho_{c1}+\rho_{r1})}}\, e^{-jk(\rho_i+\rho_{r1}+\rho_{r2})} \tag{4.148}$$

with

$$\rho_{c1} = [(Lv-x_s)^2 + y_s^2]^{1/2} \tag{4.149}$$

and

$$\rho_i = [(Fc-Lv+x_s)^2 + y_s^2]^{1/2} \quad . \tag{4.150}$$

Now y_m and y_s are related by

$$y_m = 2F_m[-1/c + \sqrt{1/c^2 + 1}] \tag{4.151}$$

where

$$c = \frac{y_s}{Lv-x_s} \quad . \tag{4.152}$$

Also, one finds that

$$x_m = y_m^2/(4Fm) \tag{4.153}$$

$$\rho_{r2} = Fm + DISPN - x_m \tag{4.154}$$

$$Y_{OB} = y_m \quad , \quad \text{and} \tag{4.155}$$

$$\rho_{r1} = [(Fm-Lv+x_s-x_m)^2 + (y_m-y_s)^2]^{1/2} . \tag{4.156}$$

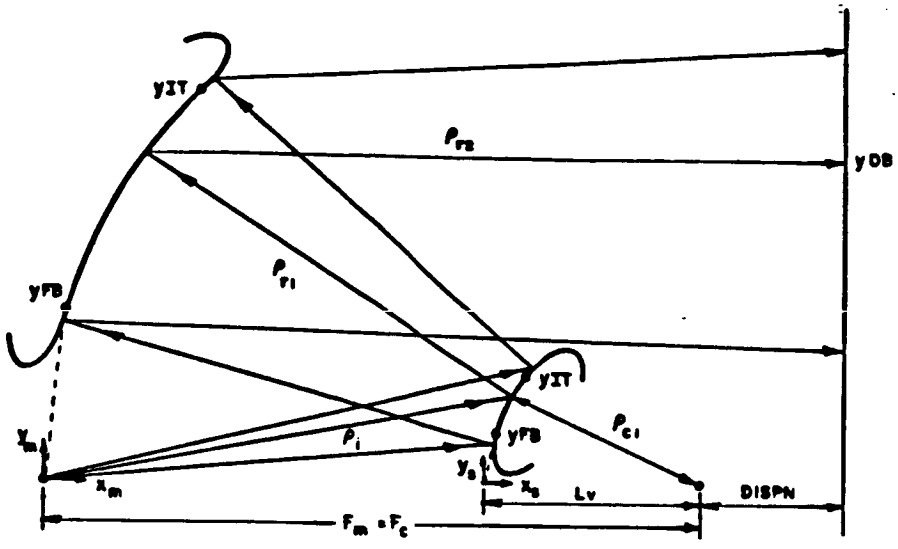

Figure 4.29 Total reflected field.

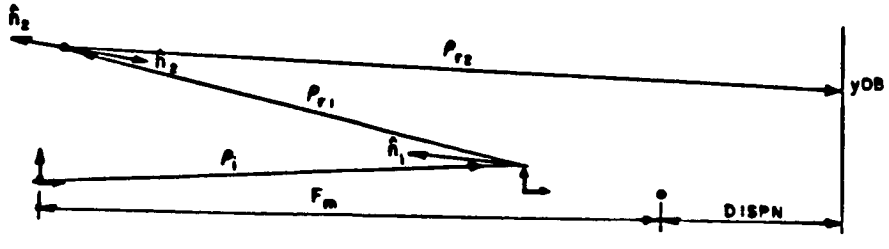

Figure 4.30 Blended surface reflected field.

Points on the subreflector are then chosen and rays traced. The hyperbola section of the subreflector reflects rays that also extend outside the parabolic section of the main reflector. The reflection point on these surfaces must be found differently.

The reflected fields for the top and bottom surfaces in Figure 4.30 are given by

$$U^{REF} = \frac{e^{-jk\rho_i}}{\sqrt{\rho_i}} \sqrt{\frac{\rho_{c1}}{\rho_{c1}+\rho_{r1}}}\, e^{-jk\rho_{r1}} \sqrt{\frac{\rho_{c2}}{\rho_{c2}+\rho_{r2}}}\, e^{-jk\rho_{r2}} \tag{4.157}$$

or

$$U^{REF} = \sqrt{\frac{\rho_{c1}\rho_{c2}}{\rho_i(\rho_{c1}+\rho_{r1})(\rho_{c2}+\rho_{r2})}}\, e^{-jk(\rho_i+\rho_{r1}+\rho_{r2})} \tag{4.158}$$

and

$$\rho_i = [(Fc-Lv+x_s)^2 + y_s^2]^{1/2} \tag{4.159}$$

where x_s and y_s are chosen on the subreflector. There are two possibilities for ρ_{c1}. If (X_s,Y_s) is on the hyperbola section then

$$\rho_{c1} = [(Lv-x_s)^2 + y_s^2] \tag{4.160}$$

Otherwise, ρ_{c1} for the surface s is given by Equation (4.28) and those that follow it. The reflection point on the main reflector must now be found. For (X_s,Y_s) on the hyperbola, one obtains

$$\hat{n}_1 = n_x\hat{x} + n_y\hat{y} = \frac{-\hat{x} + \frac{(a/b^2)y_s}{[1+(Ys/b)^2]^{1/2}}\hat{x}}{1 + \left[\frac{(a/b^2)y_s}{[1+(ys/b)^2]^{1/2}}\right]^{2\ 1/2}}. \tag{4.161}$$

In the subreflector section, $\cos\theta_i$ was calculated such that

$$\cos\theta_i = \hat{n}_1 \cdot \hat{\rho}_{r1} \tag{4.162}$$

and

$$\rho_{r1} = \frac{-(Fm-L_v+y_s-y_m)\hat{x}+(y_m-y_s)\hat{y}}{\rho_{r1}} \tag{4.163}$$

where

$$\rho_{r1} = [(Fm-Lv+x_s-x_m)^2+ (y_m-y_s)^2]^{1/2} \tag{4.164}$$

for a given parameter Y_p for the main reflector. The reflection point (x_m,y_m) is then found using a bisection routine to solve for Y_p. For the blended surfaces, the normal was calculated in the subreflector section, and the reflection point is found in a similar manner. The normal for the main reflector was also previously calculated, and the incident vector is

$$\hat{\rho}_i = -\hat{\rho}_{r1} \quad . \tag{4.165}$$

So, one finds that

$$\cos\theta_i = \hat{\rho}_i \cdot \hat{n}_2 \tag{4.166}$$

and ρ_{r2} and YOB may be calculated as in the main reflector section. Finally, the caustic distance is given by

$$\frac{1}{\rho_{c2}} = \frac{1}{\rho_i} + \frac{2}{R_c\cos\theta_i} \tag{4.167}$$

with

$$\rho_i = \rho_{r1} + \rho_{c1} \tag{4.168}$$

and R_c was calculated previously. Then U^{REF} is known through selecting points on the subreflector and implementing the above ray tracing procedure.

In the moment method procedure, the entire system is represented by a geometry of points spaced a variable distance apart. This distance is usually fixed at two-tenths wavelengths for best results. Now the moment method is applied to the entire system (Figure 4.31) and the plot in Figure 4.32 results. The magnetic line source also reflects off the main reflector into the target area, and this field is subtracted yielding Figure 4.33. Next the spillover incident field and the direct reflected field off the subreflector edge are subracted out yielding Figure 4.34. The triple reflected field ripple is apparent as well as a slow varying ripple caused by successive reflections from the subreflector edge, the main reflector edge, the subreflector hyperbolic area, and the main reflector parabolic area. Of course in an actual system, this field component is not seen by using a pulsed radar system. Finally, by selectively zeroing the correct elements in the impedance matrix, the interaction between the main reflector and subreflector is eliminated resulting in Figure 4.35 where the slow and fast ripple have been eliminated. The corresponding GO plot is shown in Figure 4.36.

GO may also be used to calculate the triple reflected field level since all the basic analysis has already been completed (see Figure 4.37). First α_2 is recalculated and (x_s,y_s) found on the subreflector using a bisection method. Then ρ_{r2} is known. The normal is computed at (x_s,y_s) and another bisection method to find YOB. This yields ρ_{r3} and ρ_c which may also be calculated at this point.

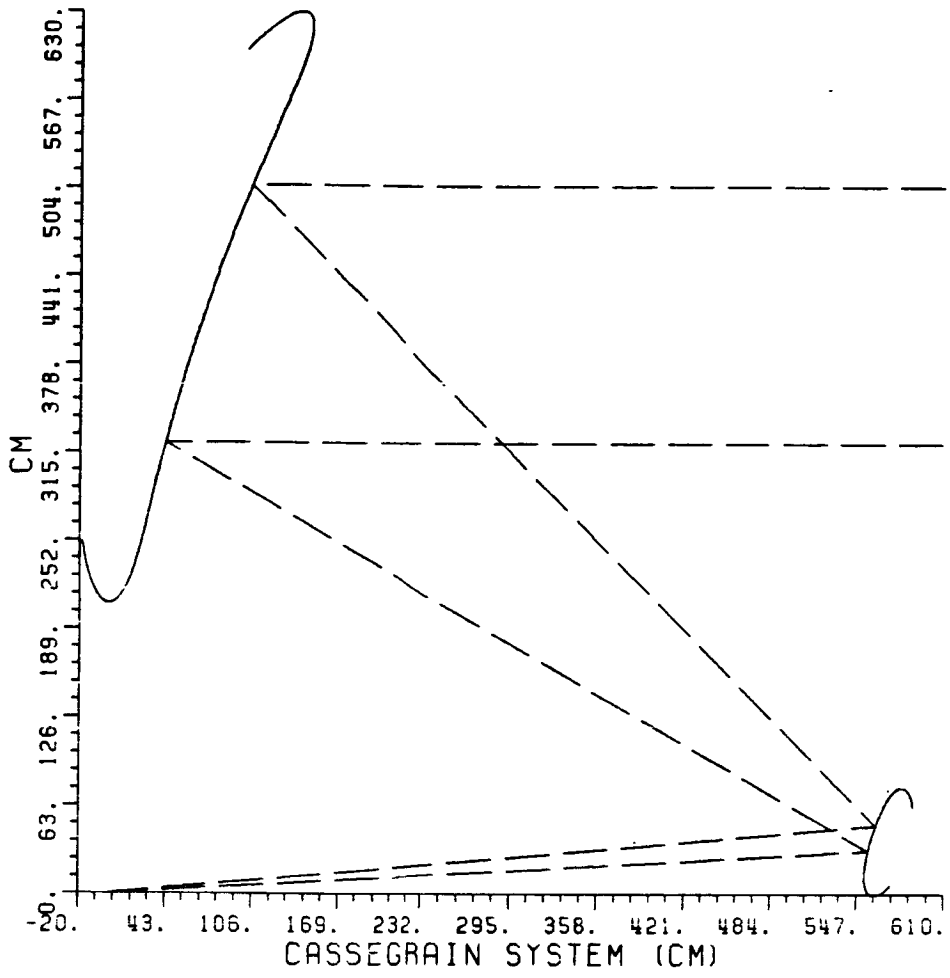

$\phi_v = 45°$
$\phi_r = 5$
Fm = 610cm
F_c = 610cm

Main Reflector

Major Axis = 80cm
Minor Axis = 30cm
Parabolic blended section = 320cm
Top edge at 505cm
Bottom edge at 322cm

Subreflector

Major Axis = 20cm
Minor Axis = 13cm
Hyperbolic section blended = 80cm
Top edge at 49.4cm
Bottom edge at 30.9cm

Unnecessary edge extensions in back regions have been eliminated.

Figure 4.31 Entire Cassegrain system.

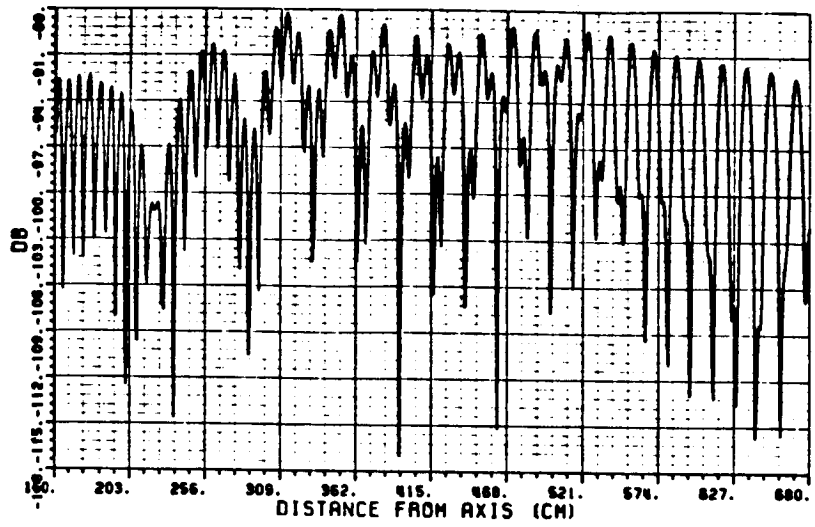

Figure 4.32 Entire system.

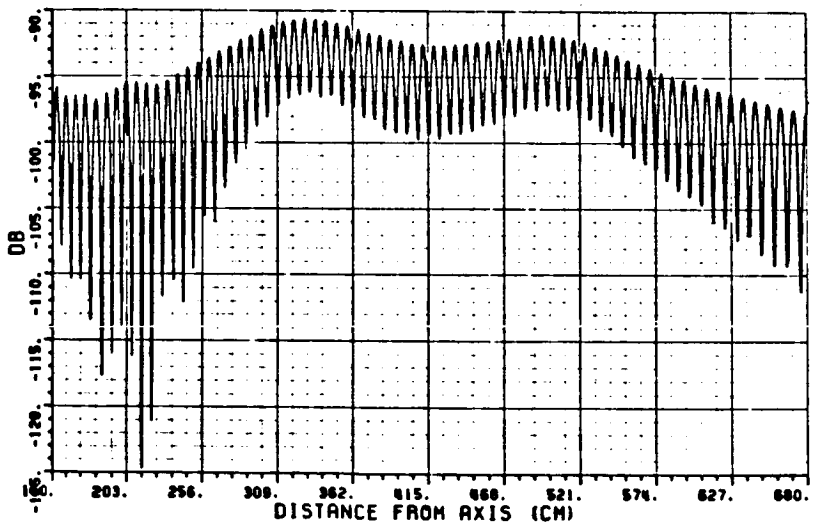

Figure 4.33 Entire system less main reflector contribution.

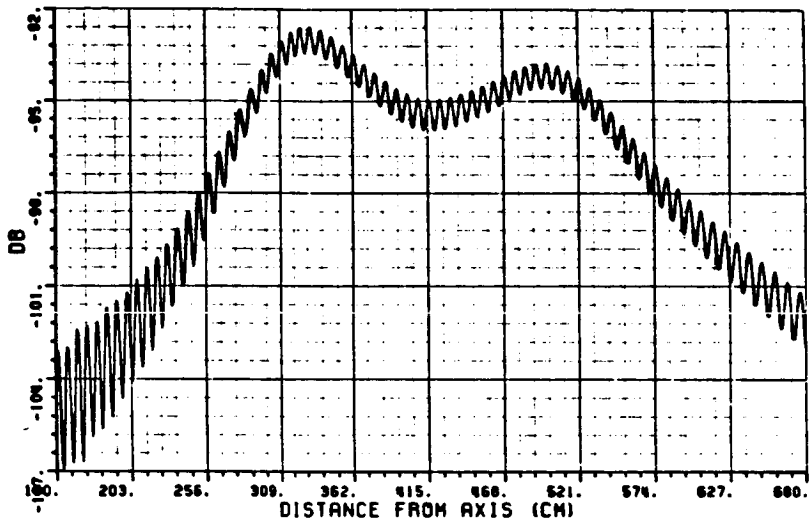

Figure 4.34 Entire system less main reflector, subreflector and spillover contribution.

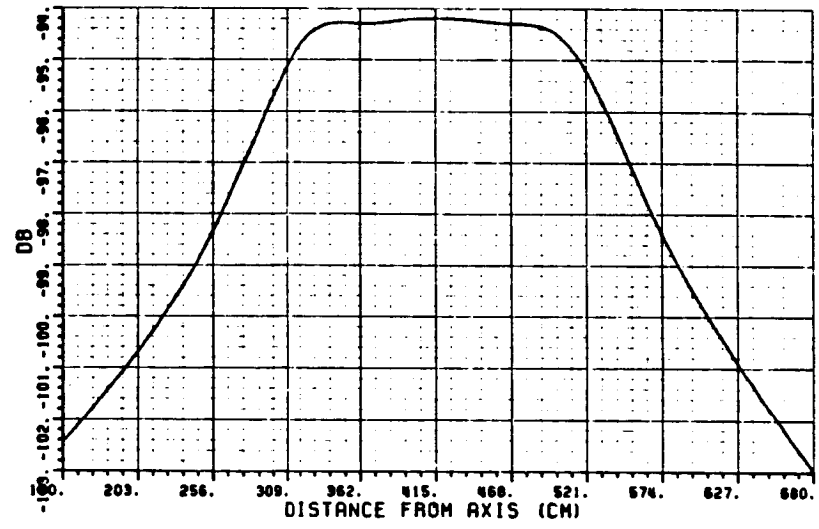

Figure 4.35 Desired reflected field.

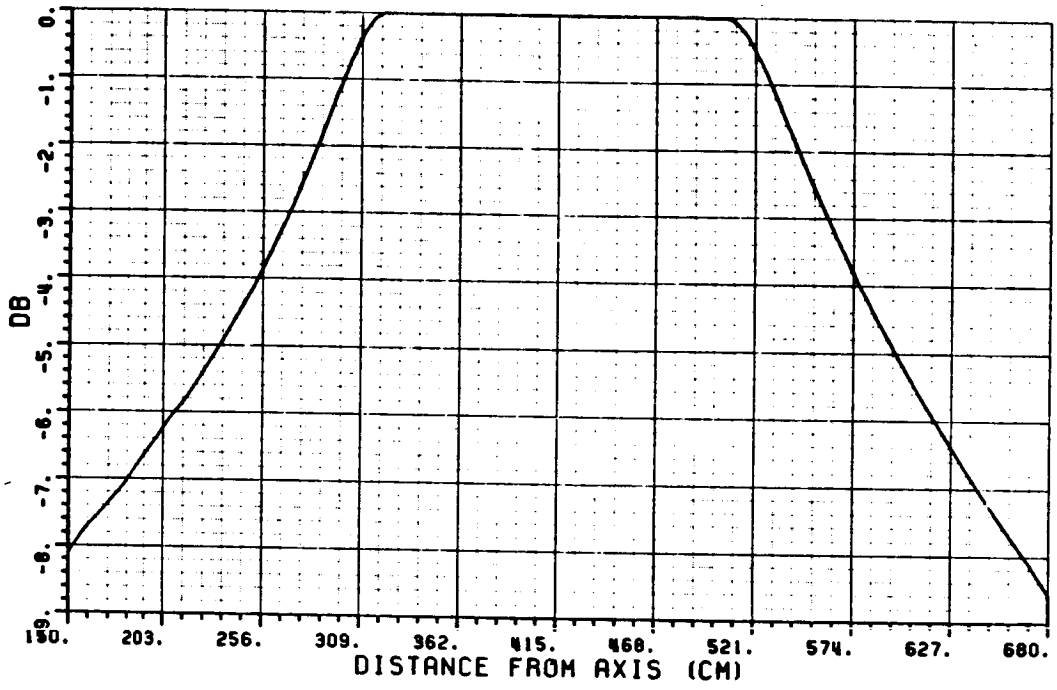

Figure 4.36 GO reflected field.

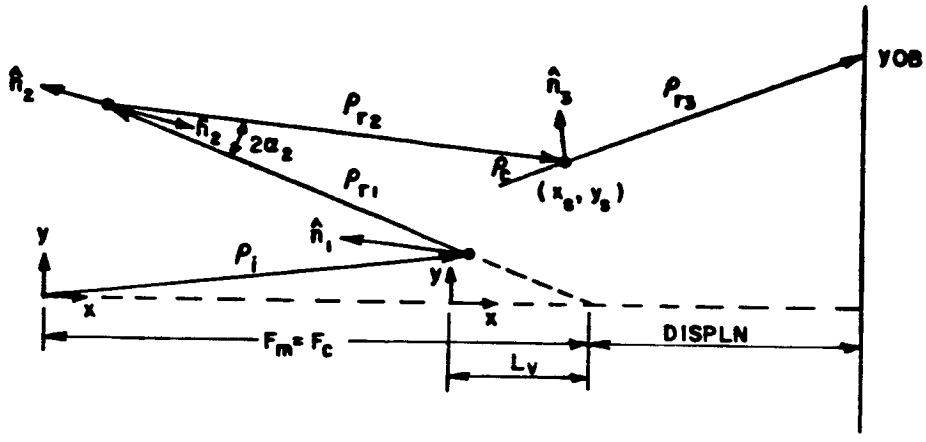

Figure 4.37 Triple reflected field.

Then

$$U^{YOB} = U_{\substack{AT \\ SUB}} \sqrt{\frac{\rho_c}{\rho_c+\rho_{r3}}}\, e^{-jk\rho_{r3}} . \qquad (4.169)$$

A plot of this field is shown in Figure 4.38. The level of this field is plotted relative to the reflected field magnitude in the center of the target zone. The triple reflected field is actually higher than that which would be given by the maximum level in Figure 4.38. This could be remedied by using a more accurate value for the reflection coefficient when computing the triple reflected field.

At this point, little else can be done about the triple reflected field without sacrificing the desired flat field performance. One alternative is to place microwave absorber in the vicinity of the subreflector to block the ray path of the triple reflected field from the subreflector to the target area. This improvement could be easily implemented. In actuality, the triple reflected field will be weaker in a three-dimensional system in that additional spread factors will reduce the triple reflected field even further.

Finally, the source horn is placed at the "origin" for convenience as well as optimal performance. Ease in changing horns and horn orientation and the close proximity of radar components make this an ideal location. A typical broadband horn gives the desired flat field over angles much greater than those considered here. If possible, a field taper is desired over the blended surfaces which will improve system performance but the major purpose of the horn is flat, broadband performance over the widest possible angles.

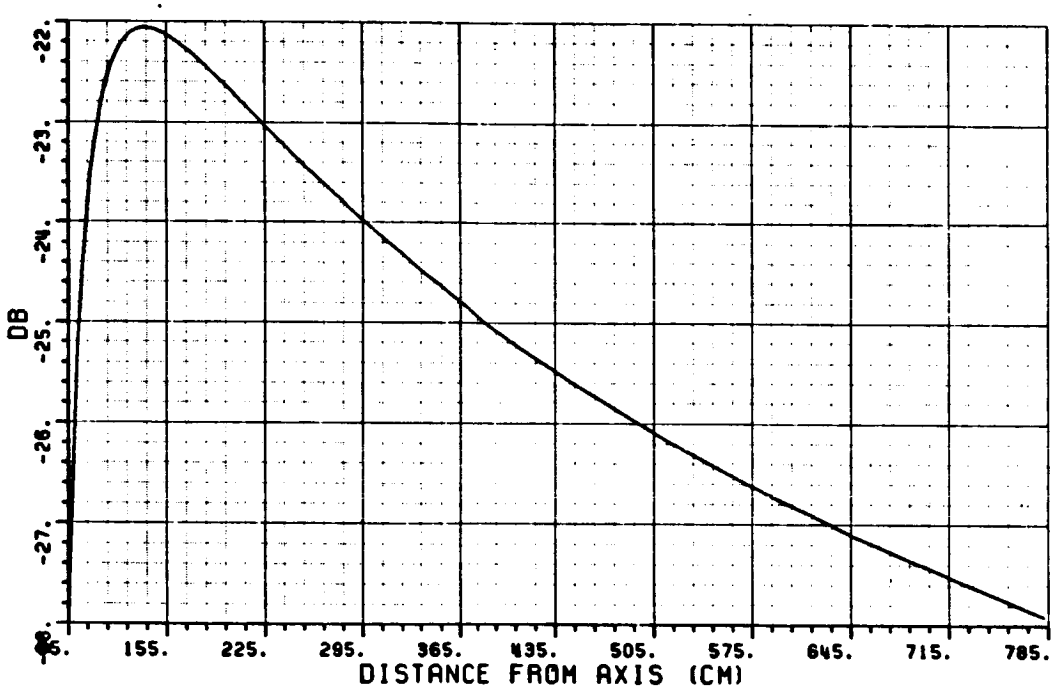

Figure 4.38 GO triple reflected field.

CHAPTER V

CASSEGRAIN SYSTEM DESIGN PROCEDURE

The Cassegrain system is a viable alternative for providing a uniform plane wave in a compact range measurement system. A procedure will be described briefly for designing a Cassegrain system given a target area dimension as a constraint. No further constraints will be given but in actuality each individual application will have its own unique restrictions.

The system described in Chapter IV will be used as an example; that is to say the target area is to have a dimension of six feet. The main reflector is considered first. It is convenient to make the vertical dimension the same six feet. Increasing this dimension will flatten the field when just considering the main reflector, but this will result in a larger overall size leading to an increased triple reflected field. Therefore, the main reflector is kept as small as possible to keep the triple reflected field to a minimum. The overall focal length (Fm) is chosen to be approximately three times the target dimension. Care must be taken to make sure the target plane is not in the far field of the main reflector at the minimum frequency of operation. For this particular case, the focal length was chosen to be twenty feet.

The edges of the main reflector must be considered next. Only the field of the main reflector (source at virtual focal point) is examined. The three blended surface variables are the major axis length, minor axis length and blended parabolic section length. The blended parabolic section is fixed at four times the major axis length for the most effective transition from the parabola to the blended surface . The major axis length should be increased until the field over the target area is flat. The natural taper of the field will also be present. Some rounding of the field at the junctions will be tolerable since the subreflector field is usually tapered and will compensate for this problem resulting in a smooth field at the junctions. Finally the minor axis length is usually one-third to two-thirds the major axis length. The actual length is set such that the minimum radius of curvature of the edge is greater than a quarter wavelength at the lowest frequency of operation. The rounding of the field at the junctions for this case had a 0.1 dB to 0.2 dB variation as is seen in Figure 4.27d of the previous chapter.

The subreflector is designed next. The goal is to generate a uniform field illuminating the parabolic section of the main reflector with a subreflector whose overall dimensions are kept as small as possible to reduce field interactions between the two reflectors. One parameter that determines the size is ϕ_r. For this example a value of five degrees was chosen. The blended surfaces are added next following the same procedure as with the main reflector. The far field pattern is then examined and a half dB variation over the area to be

illuminated is tolerable. In Figure 4.12b the subreflector field plot is shown and the desired illumination area is from 135° to 150° for this particular example. If the field variation is not acceptable, the size of the blended surfaces may be increased. If a flatter field is not obtained, the size of the hyperbolic reflector section must be increased, and the addition of the blended edges repeated until a satisfactory pattern is obtained.

The total system may then be put together, and the resulting pattern examined. The feed is placed beneath the main reflector at the "origin". Although the feed could be placed somewhere between the reflectors, this location is most operationally convenient and gives good source performance since the beamwidth is smaller and field flatter at this increased distance. The system is now completely specified, and little further design may be done except for varying the offset angle between the two reflectors. Increasing this offset angle without altering the rest of the system should reduce the triple reflected field. The interaction between the blended surfaces of the reflectors now results in weaker reflected fields at each edge yielding an overall reduced triple reflected field. This also changes the desired field pattern somewhat since the positioning of the hyperbolic subreflector and parabolic main reflector has changed. This change usually does not affect the desired pattern greatly but the triple reflected field is reduced. Therefore, the ideal situation is to have a maximum offset angle to reduce the triple reflected field making sure that the desired field over the target area remains acceptable.

For this example, consider three cases with offset angles of 35°, 45°, and 55°. A system with ϕ_V = 35° is shown in Figure 5.1. The minimum triple reflected field from Figure 5.2 is about 1.6 dB. The desired reflected field with interactions between reflectors eliminated is shown in Figure 5.3. Within the six foot target area there is about 0.5 dB rolloff at the extremes. There is about 0.2 dB variation over 4.8 feet of the area. The next case in Figure 5.4 has ϕ_V = 45° and was the system considered in the previous chapter. At this angle the triple reflected field is reduced to about 0.9 dB (see Figure 5.5). The desired reflected field has a 0.4 dB rolloff within the six foot area and 0.2 dB variation over 5.4 feet (see Figure 5.6). The final case has ϕ_V = 55° as shown in Figure 5.7. The triple reflected field has now been reduced to a level of 0.6 dB (see Figure 5.8). This change of 0.3 dB is not as great as the reduction between the angles of 35° and 45° which implies diminishing returns with increasing angles. The desired reflected field has less than 0.4 dB rolloff within the six foot target area. And 0.2 dB variation over 5.4 feet as shown in Figure 5.9. Therefore, a maximum offset angle is desired but this must be tailored to each individual case. Note that the polarization performance will deteriorate with increasing tilt angle for a full three-dimensional system.

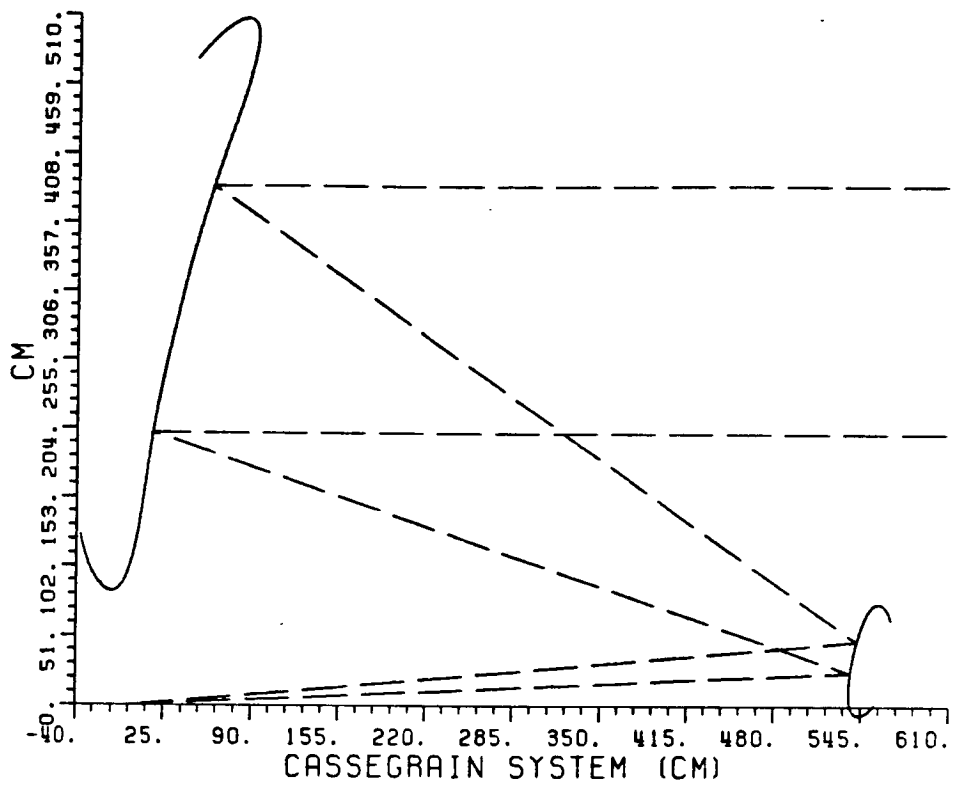

ϕ_v = 35°
ϕ_r = 5°
Fm = 610 cm
Fc = 610 cm

Main Reflector		Subreflector	
Major Axis = 80 cm		Major Axis = 20 cm	
Minor axis = 30 cm		Minor Axis = 13 cm	
Blended parabolic section	= 320 cm	Blended hyperbolic Section	= 80 cm
Top edge at 384 cm		Top edge at 47.4 ccm	
Bottom edge at 201 cm		Bottom edge at 24.5 cm	

Unnecessary edge extensions in back regions have been eliminated.

Figure 5.1 Cassegrain system with ϕ_v = 35°.

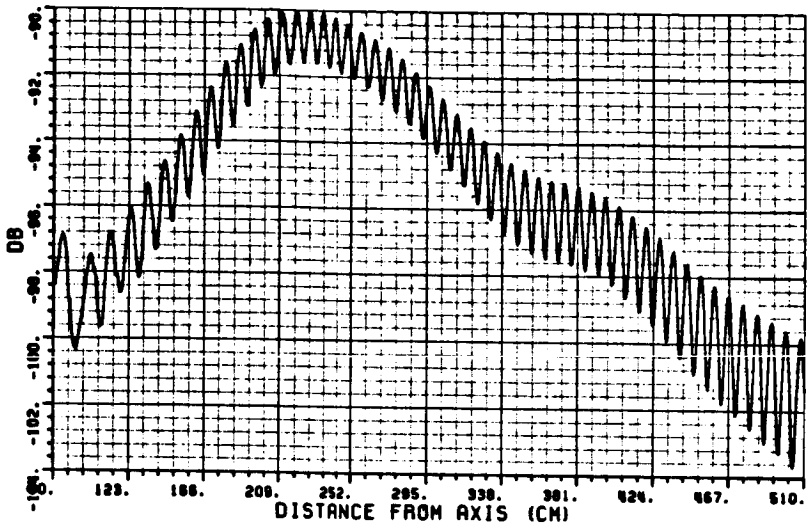

Frequency = 4 GHz

Figure 5.2 Moment method plot showing triple reflected field.

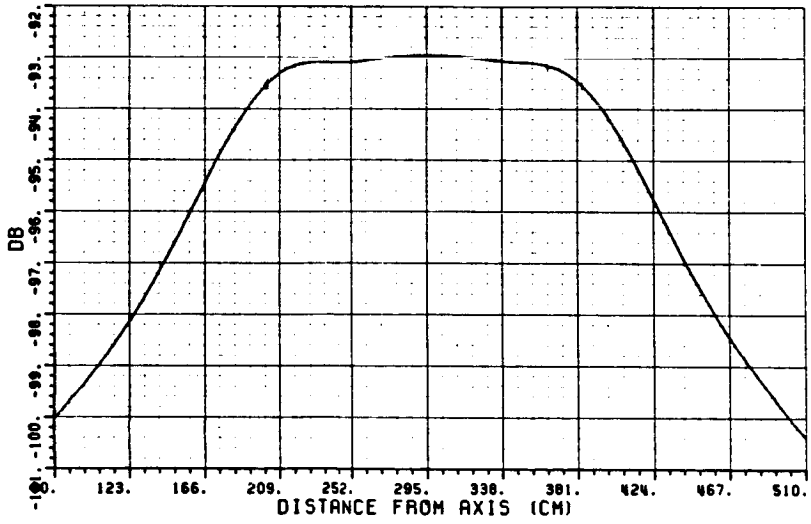

Frequency = 4 GHz

Figure 5.3 Moment method plot of desired reflected field.

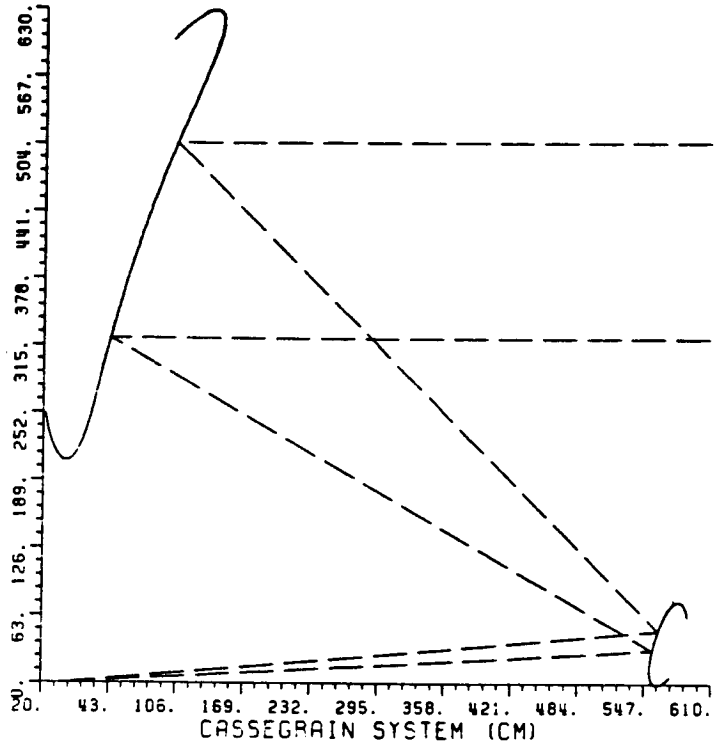

ϕ_v = 45°
ϕ_r = 5°
Fm = 610 cm
Fc = 610 cm

Main Reflector	Subreflector
Major Axis = 80 cm	Major Axis = 20 cm
Minor axis = 30 cm	Minor Axis = 13 cm
Blended parabolic section = 320 cm	Blended hyperbolic Section = 80 cm
Top edge at 505 cm	Top edge at 49.1 ccm
Bottom edge at 322 cm	Bottom edge at 30.9 cm

Unnecessary edge extensions in back regions have been eliminated.

Figure 5.4 Cassegrain system with ϕ_v = 45°.

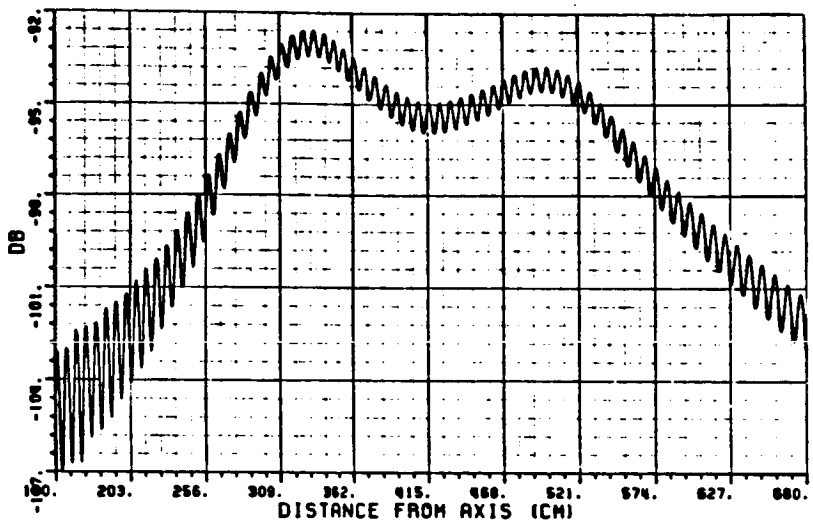

Frequency = 4 GHz

Figure 5.5 Moment method plot showing triple reflected field.

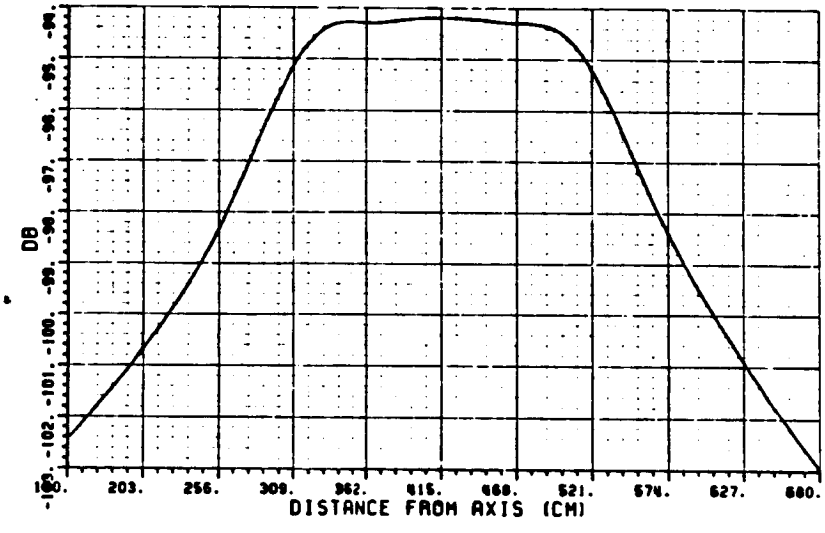

Frequency = 4 GHz

Figure 5.6 Moment method plot of desired reflected field.

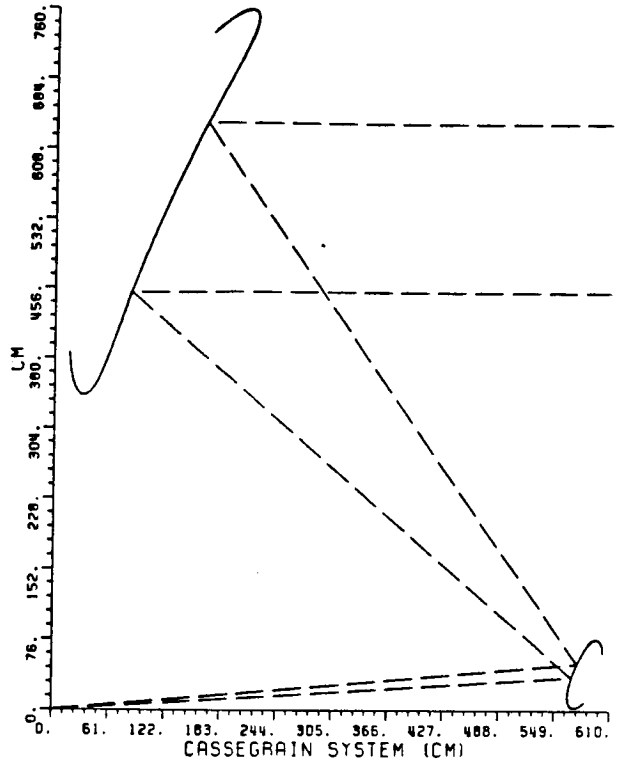

$\phi_v = 55°$
$\phi_r = 5°$
Fm = 610 cm
Fc = 610 cm

Main Reflector	Subreflector
Major Axis = 80 cm	Major Axis = 20 cm
Minor axis = 30 cm	Minor Axis = 13 cm
Blended parabolic section = 320 cm	Blended hyperbolic Section = 80 cm
Top edge at 635 cm	Top edge at 50.29 cm
Bottom edge at 452 cm	Bottom edge at 35.35 cm

Unnecessary edge extensions in back regions have been eliminated.

Figure 5.7 Cassegrain system with $\phi_v = 55°$.

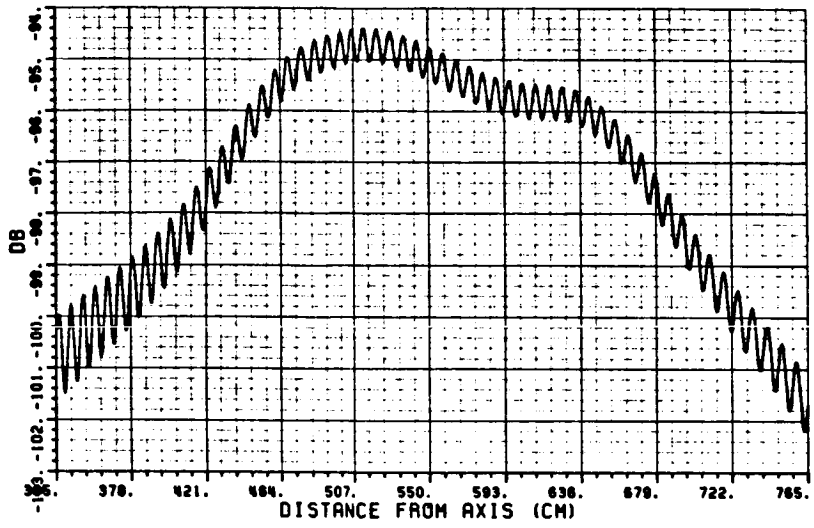

Frequency = 4 GHz

Figure 5.8 Moment method plot showing triple reflected field.

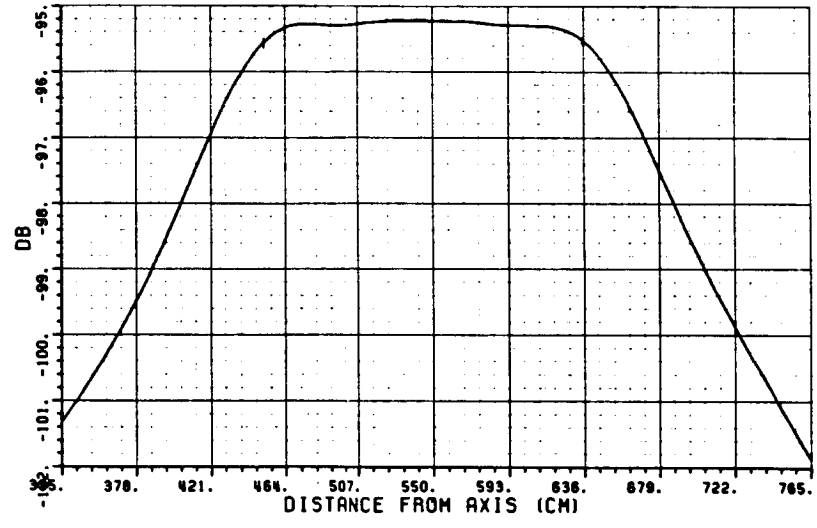

Frequency = 4 GHz

Figure 5.9 Moment method plot of desired reflected field.

CHAPTER VI

CONCLUSIONS

In conclusion, the Cassegrain system will provide a uniform plane wave but the triple reflected field ripple must be reduced through judicious design and absorber blocking. The blended edges provide superior performance over large target areas for a given size reflector system. Design and analysis is best implemented by studying the main reflector and subreflector separately. Then the system may be put together to complete the analysis.

Different techniques were used to study the system. The moment method provides accurate results but is limited by structure size and computational speed. Though difficult to implement in some situations, UTD provides results which compare favorably with moment method even when just examining the reflected field. UTD is also fast and usable on large structures. Both these techniques are best utilized by examining each reflector spearately before combining and checking the total system.

With the two reflector system, the elimination of undesired field components becomes the prime consideration. Those field components which have pathlengths that differ greatly from the desired reflected field pathlength may be eliminated through time gating with the use of a pulsed radar system. The triple reflected field component does have a

similar pathlength to the desired reflected field and must be reduced through careful design of the two reflector system. If three-dimensional effects were also considered, the apparent level of this field would be reduced further. Absorber blocking around the subreflector would also reduce the triple reflected field at the expense of introducing diffracted components from the absorber. The diffracted fields from all blended surface junctions have been virtually eliminated through the blending process.

This report is not a complete study of this topic, but it serves to illustrate the potential benefits and problem areas associated with subreflector compact range systems. Further work is needed for three-dimensional structures in order to give additional insight into the working of the system as well as give improved accuracy in the area of several field components. The blending procedure implemented is new and various blending functions as well as different blending processes provide additional possibilities for system enhancement. The diffracted field at the blended surface junction, though not considered here, is another area of potential analysis. Other Cassegrain reflector system configurations are possible including the isolation of one reflector from the other in separate areas to reduce the interaction between the two. Finally, the actual physical construction and implementation of a Cassegrain reflector system would provide the final verification of the analysis and design.

APPENDIX A

REFLECTION POINT ON MAIN REFLECTOR

This appendix describes how the reflection point on the main reflector is found. Knowing that the angle of incidence equals the angle of reflection, a point, (X_o, Y_o) is initially chosen on the parabola (see Figure A.1). Now the normal is given by

$$\hat{n} = \frac{\hat{x} - \frac{y}{2f}\hat{y}}{\left(1 + \frac{y^2}{4f^2}\right)^{1/2}} \quad . \tag{A.1}$$

A new coordinate system is formed at "O" (see Figure A.2). R is the radius of curvature and given by

$$R = 2f\left(1 + \frac{y^2}{4f^2}\right)^{3/2} \tag{A.2}$$

so "O" is located at

$$X_{OR} = X_o + 2f\left(1 + \frac{y^2}{4f^2}\right) \tag{A.3}$$

and

$$Y_{OR} = Y_o - \left(1 + \frac{y^2}{4f^2}\right)y \quad . \tag{A.4}$$

Working in this new coordinate system, move $\Delta\phi$ and assume R remains the same for this small change. Now

$$\cos\theta_i = \cos\theta_r$$

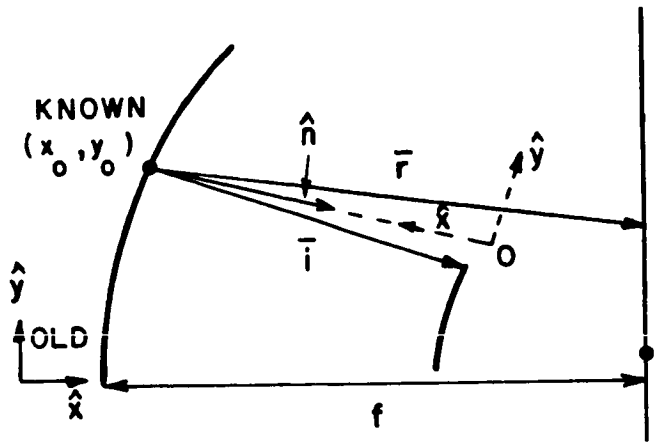

Figure A.1 Initial reflection point.

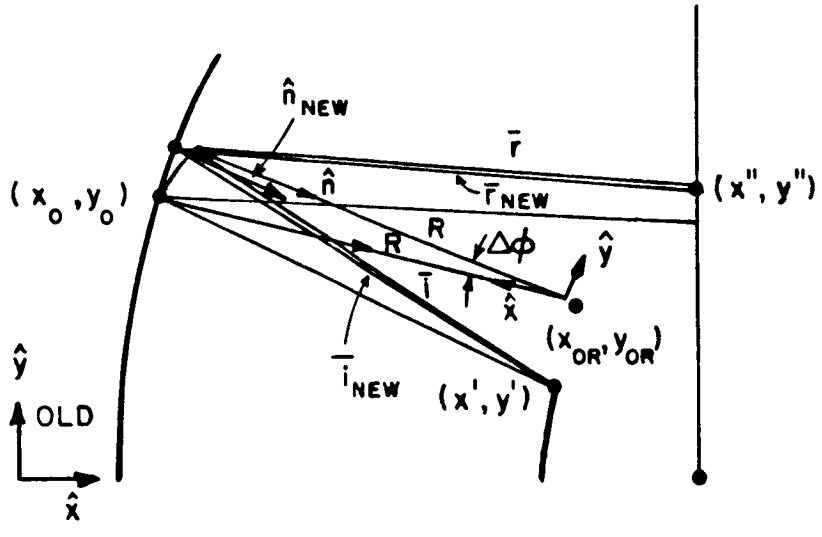

Figure A.2 New coordinate system.

or

$$\hat{n} \cdot \hat{i} = \hat{n} \cdot \hat{r} \tag{A.5}$$

and

$$\bar{i} = (x'\hat{x} + y'\hat{y}) - \hat{x}R\cos\Delta\phi - \hat{y}R\sin\Delta\phi \ ,$$

$$\bar{r} = \hat{x}(x'' - R\cos\Delta\phi) + \hat{y}(y'' - R\sin\Delta\phi) \ ,$$

and

$$\hat{n} = -(\hat{x}\cos\Delta\phi + \hat{y}\sin\Delta\phi).$$

Now as $\Delta\phi \to 0$, $\cos\Delta\phi \to 1$ and $\sin\Delta\phi \to \Delta\phi$. So

$$\bar{i} \approx \hat{x}(x'-R) + \hat{y}(y'-R\Delta\phi),$$

$$\bar{r} \approx \hat{x}(x''-R) + \hat{y}(y''-R\Delta\phi),$$

and

$$\hat{n} \approx -(\hat{x}+\hat{y}\Delta\phi).$$

So Equation (A.5) simplifies (ignoring second order terms, $(\Delta\phi)^2$) to

$$\Delta\phi = \frac{(x''-R)^2[(x'-R)^2+(y')^2]-(x'-R)^2[(x''-R)^2+(y'')^2]}{2(x'-R)y'[(x''-R)^2+(y'')^2]-2y''R(x'-R)^2+2y'R(x''-R)^2-2(x''-R)y''\cdot[(x'-R)^2+(y')^2]} \ . \tag{A.6}$$

Now moving from this nearby point to a point actually on the reflector, the error is computed as follows:

$$\varepsilon = \hat{n}_{NEW}\cdot\hat{i}_{NEW}-\hat{n}_{NEW}\cdot\hat{r}_{NEW} \ . \tag{A.7}$$

The reflection point is found when the error is below some prescribed value. Otherwise, the procedure is repeated until the minimum error is obtained.

For convenience, the point actually on the reflector is shown in Figure A.3 and given by

$$Y_p = Y_{OR} + R\sin(\Delta\phi+\alpha)$$

and

$$X_p = Y_p^2/(4f)$$

where

$$\alpha = \text{TAN}^{-1}(Y_o/2f) \ . \qquad \text{(A.8)}$$

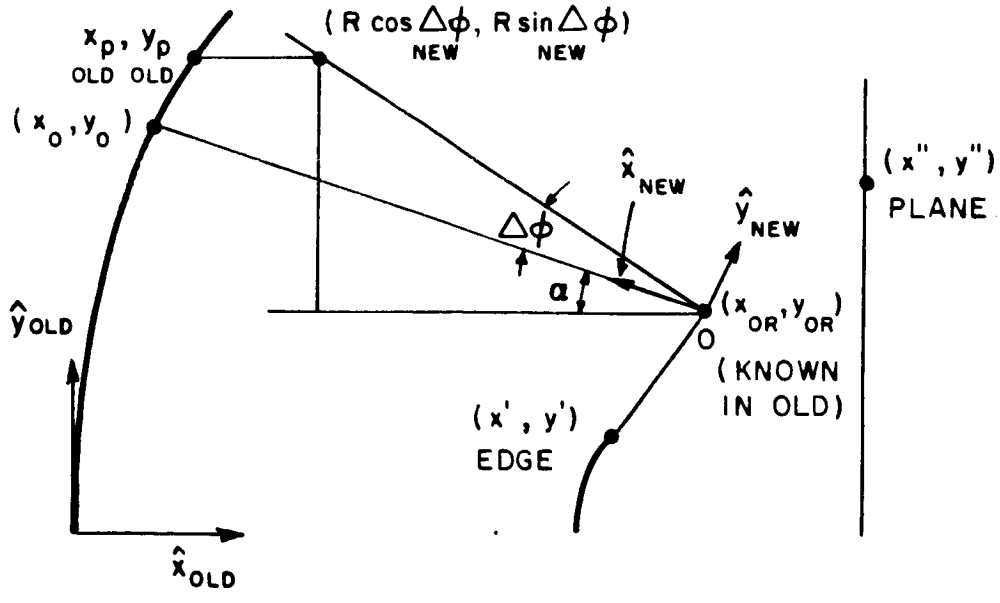

Figure A.3 Actual point on reflector.

Then

$$\hat{n}_{NEW} = \frac{\hat{x} - \frac{Y_p}{2f}\hat{y}}{(1 + Y_p^2/4f^2)^{1/2}} ,$$

$$T_{NEW} = (x'_{OLD} - x_{POLD})\hat{x} + (y'_{OLD} - y_{POLD})\hat{y} ,$$

and

$$\bar{r}_{NEW} = (x''_{OLD} - x_{POLD})\hat{x} + (y''_{OLD} - y_{POLD})\hat{y}.$$

The subscript "OLD" refers to the original coordinate system. The error is then given by Equation (A.7) as

$$\varepsilon = \frac{1}{(1 + \frac{YPOLD^2}{4f^2})^{1/2}} \left[\frac{1}{\sqrt{(X'_{OLD} - X_{POLD})^2 + (Y'_{OLD} - Y_{POLD})^2}} \right.$$

$$(X'_{OLD} - X_{POLD} - (Y'_{OLD} - Y_{POLD})\frac{Y_{POLD}}{2f}) -$$

$$\frac{1}{\sqrt{(X''_{OLD} - X_{POLD})^2 + (Y''_{OLD} - Y_{POLD})^2}}$$

$$\left. (X''_{OLD} - X_{POLD} - (Y''_{OLD} - Y_{POLD})\frac{Y_{POLD}}{2f}) \right] . \qquad (A.9)$$

Finally, the points (x',y') and (x",y") need to be transformed to the new coordinate system as follows (see Figure A.4):

$$x'_{NEW} = (x_{OR} - x'_{OLD})\cos\alpha - (y_{OR} - y'_{OLD})\sin\alpha \qquad (A.10)$$

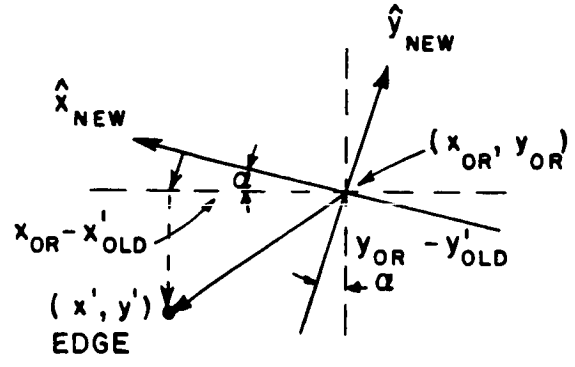

(a) (x',y') coordinate transformation.

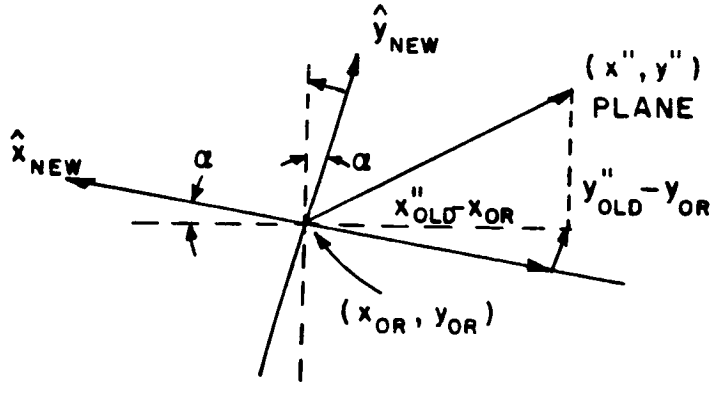

(b) (x",y") coordinate transformation.

Figure A.4 Coordinate system transformation.

$$y'_{NEW} = -[(x_{OR} - x'_{OLD})\sin\alpha + (y_{OR} - y'_{OLD})\cos\alpha] \tag{A.11}$$

and

$$x''_{NEW} = (y''_{OLD} - y_{OR})\sin\alpha - (x''_{OLD} - x_{OR})\cos\alpha \tag{A.12}$$

$$y''_{NEW} = (y''_{OLD} - y_{OR})\cos\alpha + (x''_{OLD} - x_{OR})\sin\alpha \quad . \tag{A.13}$$

Another method of proceeding is to take the cross product

$$\hat{i} \times \hat{n} = \hat{n} \times \hat{r}$$

and form

$$\frac{\hat{n} \cdot \hat{i}}{\hat{i} \times \hat{n}} = \frac{\hat{n} \cdot \hat{r}}{\hat{n} \times \hat{r}}$$

or

$$(\hat{n} \cdot \hat{i})(\hat{n} \times \hat{r}) = (\hat{n} \cdot \hat{r})(\hat{i} \times \hat{n})$$

or

$$(\hat{n} \cdot \bar{i})(\hat{n} \times \bar{r}) = (\hat{n} \cdot \bar{r})(\bar{i} \times \hat{n}) \quad . \tag{A.14}$$

Using the small argument forms of $\bar{i}$, $\bar{r}$, and $\hat{n}$, Equation (A.14) yields

$$\Delta\phi = \frac{y'(x''-R) + y''(x'-R)}{x'(x''-R) + x''(x'-R) - 2y'y''} \tag{A.15}$$

when ignoring second order terms. Equation (A.15) may be used as an alternative to Equation (A.6).

APPENDIX B

REFLECTION POINT ON ELLIPTICAL EDGE OF SUBREFLECTOR

This appendix describes how the reflection point on the elliptical rolled edge of the subreflector is found. In Figure B.1 point (s,t) is known and the normal to the surface of the ellipse is given by

$$\hat{n} = x_o\hat{x} + y_o\hat{y} = \frac{B\cos v\cos\theta - A\sin v\sin\theta}{[B^2\cos^2 v + A^2\sin^2 v]^{1/2}}\hat{x} + \frac{B\cos v\sin\theta + A\sin v\cos\theta}{[B^2\cos^2 v + A^2\sin^2 v]^{1/2}}\hat{y} . \tag{B.1}$$

The dot product is then formed

$$\frac{\bar{i}\cdot\hat{n}}{|\bar{i}|} = \frac{\bar{r}\cdot\hat{n}}{|\bar{r}|} , \tag{B.2}$$

with

$$\bar{i} = \hat{x} + f\hat{y} , \tag{B.3}$$

and

$$\bar{r} = -\hat{x} . \tag{B.4}$$

Now at point (s,t),

$$t = fs+g \quad \text{or} \quad g = t-fs$$

so

$$y = f(x-s) + t$$

or

$$f = \frac{y-t}{x-s} \tag{B.5}$$

where for the ellipse

$$y = A\sin\theta\cos v + B\cos\theta\sin v + Y_E \tag{B.6}$$

and

$$x = A\cos v\cos\theta - B\sin v\sin\theta + X_E \ . \tag{B.7}$$

to find v which gives the reflection point, an initial guess is made. From Equation (B.5) f is calculated and then the dot product in Equation (B.2) calculated. The difference is formed

$$\text{ERROR} = \frac{\bar{i} \cdot \hat{n}}{|\bar{i}|} - \frac{\bar{r} \cdot \hat{n}}{|\bar{r}|} \tag{B.8}$$

and is this behaves nicely, v may be found by successively bisecting the v interval until the desired error tolerance is obtained. Once v and the reflection point are known, remaining parameters may easily be calculated which finally yield the desired field.

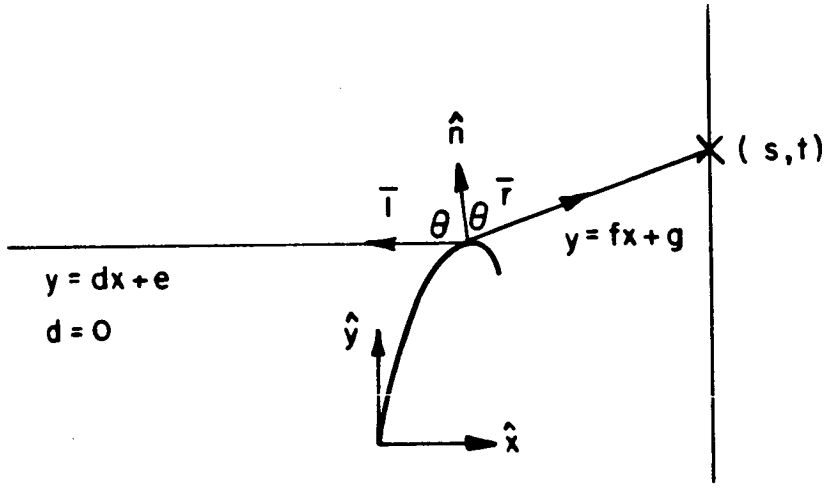

Figure B.1 Reflection point on elliptical rolled edge.

APPENDIX C

MODIFICATIONS FOR VARIABLE DISTANCE TO PLANE

When making the plane of interest a variable distance (see Figure C.1), the following modifications must be done. For the reflected field, ρ_{r2} becomes ρ_{r2} + DISPLN. For the diffracted field from the main reflector rolled edge junction, ρ must be recalculated. First

$$\theta_i = \cos^{-1}\left(\frac{Dm/2}{\rho^E_{r1} + \rho^E_c}\right), \tag{C.1}$$

$$\theta_2 = \tan^{-1}\left(\frac{DISPLN}{y(I)}\right) \tag{C.2}$$

and

$$\rho = [(\rho^E_{r1} + \rho^E_c)^2 + Y(I)^2 + DISPLN^2 - 2(\rho^E_{r1} + \rho^E_c)(Y(I)^2 + DISPLN^2)^{1/2} \cos(\theta_1 + \theta_2)]^{1/2}. \tag{C.3}$$

Now

$$\beta^- = \phi - \phi' \tag{C.4}$$

or

$$\beta- = \cos\text{-}1\left[\frac{-y(I)^2 - DISPLN^2 + \rho^2 + (\rho^E_{r1} + \rho^E_c)^2}{2\rho(\rho^E_{r1} + \rho^E_c}\right]. \tag{C.4}$$

Next

$$\beta^+ = \phi+\phi'$$

and

$$\theta_i = 1/2 \sin^{-1}\left(\frac{Dm/2}{\rho^E_{r1}+\rho^E_c}\right)$$

and

$$\phi' = \pi/2 - \theta_i.$$

So

$$\beta^+ = 2\phi' + (\phi-\phi')$$

or

$$\beta^+ = \pi - \sin^{-1}\left(\frac{Dm/2}{\rho^E_{r1}+\rho^E_c}\right) + \beta^-. \qquad (C.5)$$

For the diffracted field from the subreflector edge junction,

$$x''_{OLD} = Fm + DISPLN.$$

Finally for the triple reflected field, s goes to Lv + DISPLN.

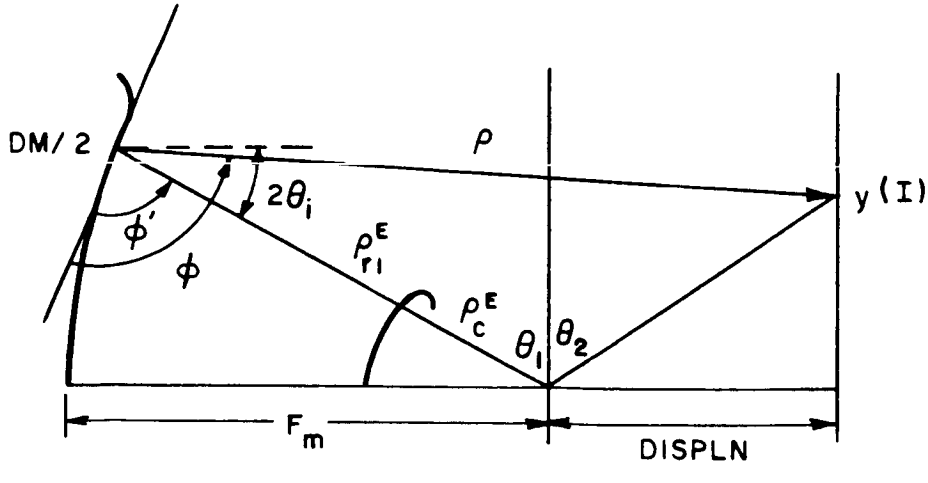

Figure C.1 Variable distance to plane.

REFERENCES

[1] Balanis, C.A., Antenna Theory: Analysis and Design, Harper & Row, Inc., (1982), Chapter 13.

[2] Hanna, P.W., "Microwave Antennas Derived from the Cassegrain Telescope", IRE Trans. on Antennas and Propagation, Vol. AP-9, pp. 140-153, March 1961.

[3] Heedy, D.J., "An E-Plane Analysis of Aperture-Matched Horn Antennas Using the Moment Method and the Uniform Geometrical Theory of Diffraction", M.Sc. Thesis, The Ohio State University ElectroScience Laboratory, Department of Electrical Engineering, Columbus, Ohio, 1984.

[4] Rumsey, V.H., "Reaction Concept in Electromagnetic Theory", Physical Review, Vol. 94, June 15, 1954, pp. 1483-1491.

[5] Schellkunoff, S.A., "On Diffraction and Radiation of Electromagnetic Waves", Physical Review, Vol. 56, August 15, 1939.

[6] Richmond, J.H., "An Integral-Equation Solution for TE Radiation and Scattering from Conducting Cylinders", Report 2902-7, October 1972, The Ohio State University ElectroScience Laboratory, Department of Electrical Engineering, prepared under Grant NGL 36-008-138 for National Aeronautics and Space Administration, Langley Research Center.

[7] Burnside, W.D., "Microwave Optics", class notes for Electrical Engineering course 712, The Ohio State University, 1983.